SYNTHESIS OF REDUCED GRAPHENE OXIDE/TUNGSTEN TRIOXIDE NANOCOMPOSITE ELECTRODE FOR HIGH ELECTROCHEMICAL PERFORMANCE

CHRISTELLE WONG PAU PING

INSTITUTE OF GRADUATE STUDIES
UNIVERSITY OF MALAYA
KUALA LUMPUR

2017

SYNTHESIS OF REDUCED GRAPHENE OXIDE/TUNGSTEN TRIOXIDE NANOCOMPOSITE ELECTRODE FOR HIGH ELECTROCHEMICAL PERFORMANCE

CHRISTELLE WONG PAU PING

DISSERTATION SUBMITTED IN FULFILMENT OF THE REQUIREMENTS FOR THE DEGREE OF MASTER OF PHILOSOPHY

INSTITUTE OF GRADUATE STUDIES
UNIVERSITY OF MALAYA
KUALA LUMPUR

2017

UNIVERSITY OF MALAYA

ORIGINAL LITERARY WORK DECLARATION

Name of Candidate: Christelle Wong Pau Ping

Matric No: HGA 140017

Name of Degree: Master of Philosophy

Title of Dissertation: Synthesis of Reduced Graphene Oxide/Tungsten Trioxide Nanocomposite Electrode for High Electrochemical Performance

Field of Study: Chemistry (Nanotechnology)

I do solemnly and sincerely declare that:

(1) I am the sole author/writer of this Work;
(2) This Work is original;
(3) Any use of any work in which copyright exists was done by way of fair dealing and for permitted purposes and any excerpt or extract from, or reference to or reproduction of any copyright work has been disclosed expressly and sufficiently and the title of the Work and its authorship have been acknowledged in this Work;
(4) I do not have any actual knowledge nor do I ought reasonably to know that the making of this work constitutes an infringement of any copyright work;
(5) I hereby assign all and every rights in the copyright to this Work to the University of Malaya ("UM"), who henceforth shall be owner of the copyright in this Work and that any reproduction or use in any form or by any means whatsoever is prohibited without the written consent of UM having been first had and obtained;
(6) I am fully aware that if in the course of making this Work I have infringed any copyright whether intentionally or otherwise, I may be subject to legal action or any other action as may be determined by UM.

Candidate's Signature Date:

Subscribed and solemnly declared before,

Witness's Signature Date:

Name:

Designation:

ABSTRACT

The consumption of non-renewable energy has raised severe environmental issues to the Earth. An increase in fossil fuel burning directly increased the volume of greenhouse gases. As results the Earth is getting warmer and sea levels increased continuously. In order to solve the problem, renewable energy resources have been intensively researched. However, renewable energy requires an energy storage device such as supercapacitor to maximize the utilization of energies. Electrode material is a promising target for the development of sustainable supercapacitor for future energy system. The formation of desired electrode material is essential in order to fabricate supercapacitor with higher power density and longer life cycle than secondary batteries in electronic application. In this study, Pre-oxidized reduced graphene oxide (P-rGO) was successfully synthesized through two-steps modified Hummers' method followed by chemical reduction method. Based on the results, the synthesized P-rGO exhibited higher capacitance as compared to rGO that synthesized through single-step modified Hummers' method. Continuous efforts have been exerted to further improve the electrochemical performance of P-rGO/WO_3 nanocomposite by incorporating an optimum content of WO_3 on P-rGO sheets using hydrothermal technique. In this manner, comprehensive investigations on different parameters, such as loadings of ammonium paratungstate (APT), hydrothermal temperature and reaction time were conducted in order to study the formation of P-rGO/WO_3 nanocomposite. WO_3 and P-rGO/WO_3 nanocomposite were successfully synthesized through a simple hydrothermal method. It was found that P-rGO/WO_3 nanocomposite in ratio of 1:100 and subsequently heat treated at 150 ºC for 20 hours demonstrated a maximum electrochemical behavior with specific capacitance of 274.0 F g^{-1} at a current density of 0.7 A g^{-1}. This performance was approximately twice higher than the pure WO_3. The presence of WO_3 at 1:100 in P-rGO/WO_3 nanocomposite showed an improvement in electrochemical performance because it acts as the spacer to prevent the restacking of P-rGO as well as to provide a larger surface area for electrolyte access. Moreover, the addition of P-rGO to nanocomposite could decrease the resistance of ions between the electrolyte and electrode, leading to fast electron transport.

ABSTRAK

Penggunaan tenaga yang tidak boleh diperbaharui membangkitkan masalah alam sekitar yang teruk kepada Bumi seperti membebaskan gas karbon dioksida yang berlebihan akibat pembakaran bahan api fosil. Ia menyebabkan kesan rumah hijau bertambah buruk. Situasi ini amat membimbangkan masyarakat sedunia kerana suhu bumi meningkat setiap tahun dan paras air laut terus menaik akibat leburan glasier. Justeru, sumber tenaga yang boleh diperbaharui telah menarik perhatian para penyelidik sedunia untuk menyelesaikan masalah tersebut. Namun, tenaga yang boleh diperbaharui memerlukan media penyimpanan tenaga seperti superkapasitor untuk penggunaan tenaga secara maksima. Pembentukan bahan elektrod yang dikehendaki adalah penting dalam usaha untuk mereka superkapasitor dengan ketumpatan kuasa yang lebih tinggi dan kitaran hidup lebih lama berbanding dengan bateri sekunder dalam aplikasi elektonik. Bahan elektrod menjadi tumpuan dalam pembuatan superkapasitor yang berpotensi untuk sistem tenaga masa depan. Dalam kajian ini, P-rGO telah berjaya disintesis dengan kaedah diubahsuai Hummers melalui dua langkah diikuti dengan kaedah penurunan kimia. Berdasarkan keputusan yang diperolehi, P-rGO menghasilkan nilai kapasitan spesifik yang lebih tinggi berbanding dengan rGO yang disintesis melalui satu langkah kaedah diubahsuai Hummers. Pelbagai parameter yang mempengaruhi morfologi P-rGO/WO_3 komposit nano telah dikaji dengan lebih teliti seperti kepekatan bahan mula, suhu tindak balas, dan masa tindak balas. Selain itu, WO_3 dan P-rGO/WO_3 komposit nano telah berjaya disintesis melalui kaedah hidroterma yang ringkas. Dalam usaha untuk meningkatkan lagi prestasi elektrokimia P-rGO/WO_3 komposit nano, WO_3 dan P-rGO digabungkan melalui teknik hidroterma pada keadaan optimum. Ia didapati bahawa nisbah 1:100 P-rGO:WO_3 dengan suhu 150 ºC selama 20 jam menghasilkan nilai kapasitan spesifik yang tertinggi iaitu 274.0 F g^{-1} pada ketumpatan arus 0.7 A g^{-1}. Prestasi ini adalah dua kali ganda lebih tinggi daripada WO_3. Kewujudan WO_3 dalam P-rGO/WO_3 komposit nano menyebabkan prestasi elektrokimia bertambah baik kerana ia bertindak sebagai spacer untuk menghalang penumpuan P-rGO serta menyediakan permukaan spesifik yang lebih besar untuk penembusan elektrolit. Tambahan pula, P-rGO boleh mengurangkan rintangan antara elektrolit dengan elektrod, dan ini mempercepatkan lagi penembusan elektrolit.

ACKNOWLEDGEMENTS

I would like to express my sincere gratitude to my supervisor Dr. Lai Chin Wei for his germinal ideas, invaluable guidance, continuous encouragement and constant support in making this research possible. He always impressed me with his outstanding professional conduct, time spent and commitment to this study and future career. The supervision and support gave truly help the progression and smoothness of my master study. The cooperation is much indeed appreciated.

My sincere thanks should be given to all my lab mates and assistants of NANOCAT's laboratory, University of Malaya, who helped me in many ways. Many special thanks go to Dr. Lee Kian Mun for his suggestions, guidance, help and supports during this study. All projects would be nothing without the enthusiasm and imagination from them.

Great deals appreciated go to my parents for their love, dream and sacrifice throughout completion of this study. Last but not least, I would like to express my gratefulness to all of them who involve directly or indirectly in this study. Thank you.

TABLE OF CONTENTS

LIST OF FIGURES

LIST OF TABLES

LIST OF SYMBOLS AND ABBREVIATIONS

1D	:	One dimensional
2D	:	Two dimensional
AC	:	Activated carbon
ACN	:	Acetonitrile
APT	:	Ammonium paratungstate
BDHSC	:	Bagasse-derived hierarchical structured carbon
BET	:	Brunauer-Emmett-Teller
BSE	:	Back-scattered electrons
CDC	:	Carbide derived carbons
CNTs	:	Carbon nanotubes
CO_2	:	Carbon dioxide
Co_3O_4	:	Cobalt (II,III) oxide
CV	:	Cyclic voltammetry
CVD	:	Chemical vapour deposition
EDLC	:	Electrical double-layer capacitor
EDX	:	Energy dispersion X-ray spectroscope
EIS	:	Electrochemical impedance spectroscopy
EMIM-BF_4	:	1-ethyl-3-methylimidazolium tetrafluoroborate
ESR	:	Equivalent series resistance
Fe_2O_3	:	Iron (III) oxide
FESEM	:	Field emission scanning electron microscope
FNC	:	Fluorine-rich nanoporous carbon
G	:	Graphite
GCD	:	Galvanostatic charge/discharge

GO	:	Graphene oxide
H_2	:	Hydrogen
HBr	:	Hydrogen bromide
HCl	:	Hydrochloric acid
HF	:	Hydrogen fluoride
H_2O_2	:	Hydrogen peroxide
H_2SO_4	:	Sulfuric acid
h-WO_3	:	Hexagonal tungsten trioxide
IHP	:	Inner Helmholtz plane
$KMnO_4$	:	Potassium permanganate
KNO_3	:	Potassium nitrate
KOH	:	Potassium hydroxide
K_2SO_4	:	Potassium sulfate
$K_2S_2O_8$	:	Potassium persulfate
$LiPF_6$	:	Lithium hexafluorophosphate
MnO_2	:	Manganese dioxide
MWNT	:	Multi-walled carbon nanotube
$NaBH_4$	:	Sodium borohydride
Na_2SO_3	:	Sodium sulfite
Na_2SO_4	:	Sodium sulfate
$Na_2WO_4 \cdot 2H_2O$	:	Sodium tungstate
NEC	:	Nippon Electric Corporation
NiO	:	Nickel (II) oxide
O_2	:	Oxygen
OHP	:	Outer Helmholtz plane
PA	:	Polyacetylene

PANI	:	Polyaniline
PC	:	Propylene carbonate
PEDOT	:	Poly(3,4-ethylenedioxythiophene)
P-G	:	Pre-oxidized graphite
P-GO	:	Pre-treated graphene oxide
P-rGO	:	Pre-treated reduced graphene oxide
P_2O_5	:	Phosphorus pentoxide
PProDOT	:	Poly(3.4-propylenedioxy thiophene)
PPy	:	Polypyrrole
PPV	:	Poly(phenylenevinylene)
PTFE	:	Polytetrafluoroethylene
PTh	:	Polythiophene
pTTPA	:	Poly(tris(4-(thiophen-2-yl)phenyl)amine)
rGO	:	Reduced graphene oxide
RuO_2	:	Ruthenium (IV) oxide
SE	:	Secondary electrons
SWNT	:	Single-walled carbon nanotube
TEA-BF_4	:	Tetraethylammonium tetrafluoroborate
TiC	:	Titanium carbide
WO_3	:	Tungsten trioxide
XRD	:	X-ray diffraction

CHAPTER 1: INTRODUCTION

1.1 Research Background

Energy, fossil fuel and environmental pollutions are strongly related to each other. Fossil fuel was used to generate electric energy, but it raises serious environmental issue such as global warming and climate change. Although approximately 21.3 billion tonnes of carbon dioxide (CO_2) are produced yearly, however, only half of it was absorbed in nature causing global warming. To overcome this problem, energy storage devices have attracted much attention because of their advantages. Supercapacitors, known as electrochemical capacitor, emerge as an ideal energy storage device, as they provide high power density, long cycling capability and fast charge/discharge as compared to batteries (Huang et al., 2013b).

Supercapacitors can be categorized into two general classes, depending on its energy storage mechanism, namely electrical double-layer capacitors (EDLCs) and pseudocapacitors. EDLCs store energy by the electrostatic accumulation of charges at the electrode-electrolyte interface instead of storing charges in the dielectric layer. On the other hand, pseudocapacitors store energy through a conventional faradaic route involving fast and reversible redox reactions between electrolyte and electroactive materials on the surface of electrodes (Faraji and Ani, 2014; Samdani et al., 2017).

In order to bring supercapacitor to the point of commercial readiness and establish high electrochemical performance of supercapacitor, substantial research on the development of electrode materials for supercapacitor application using hydrothermal technique has been developed lately. Although a number of metal oxides (i.e., Fe_2O_3, SnO_2, Co_3O_4, MnO_2, NiO and WO_3) have been reported to be supercapacitor electrode for the overall reversible redox reactions between electrolyte and electroactive materials, most of them suffer from poor cycling performance (Bonso et al., 2012; Lu et al., 2010; Pang et al.,

2012; Shinde et al., 2015; Xia et al., 2012; Zhai et al., 2013). Unfortunately, the overall high rate capability for high power performance is difficult to achieve due to their low electrical conductivity properties. To date, no metal oxides have been discovered that simultaneously meets all the criteria required for highly efficient supercapacitors.

In fact, a suitable candidate as an electrode for supercapacitor must have three basic criteria: (i) high specific surface area for the contact of electrolyte ions, (ii) good mechanical strength to prevent safety issue such as swelling and explosion and (iii) high electrical conductivity to avoid power loss due to internal resistance (Davies and Yu, 2011).

Taking this into consideration, hybrid capacitors, i.e. a combination of conductive EDLC electrode with pseudocapacitance electrode into single device have emerged as potential electrochemical capacitor in recent years. In part of EDLC electrode, rGO is generally attractive because of its unique 2D network structure, that provides an extremely large surface area, high electrical conductivity, and good mechanical strength (Chang et al., 2012). Among metal oxides, WO_3 has caught researchers' attention as a pseudocapacitance electrode owing to its high intrinsic densities, strong mechanical stability, and high melting temperature (Jo et al., 2013). However, WO_3 suffers from low electrical conductivity due to the presence of oxide. To make high electrochemical performance WO_3 electrodes, developing high surface area of WO_3 through simply synthetic method is a pre-requisite. Hydrothermal are commonly applied in the preparation of 1D tungsten oxide. This technique offers several advantages, such as inexpensive experiment setup, low energy consumption and more versatile (use variety of precursors that less toxic and easier to handle) (Iwu et al., 2012; Su et al., 2010).

To the best of our knowledge, the literatures on the formation of fiber-like nanostructure of WO_3 on pre-treated reduced graphene oxide (P-rGO) with ammonium

paratungstate (APT) as a precursor via hydrothermal route are still lacking. In this manner, coupling P-rGO with WO_3 that possess high mechanical stability and high melting temperature improve the safety of supercapacitor (Yang et al., 2012). A hybrid of P-rGO/WO_3, acting as a working electrode in a supercapacitor has been developed in our study recently. Results suggest that the hybrid P-rGO/WO_3 electrode demonstrates significant improvement of promoting the diffusion of electrolyte ions in capacitor system. Considering these facts, this present research study aims to investigate the crucial processing parameters including loadings of APT, hydrothermal temperature and reaction time on the formation of fiber-like structure of WO_3 on P-rGO sheets as well as their electrochemical performance. In addition to that, the detail information about the proposed growth mechanism of P-rGO/WO_3 nanocomposite will also be discussed in the present work.

1.2 Problem Statements

Supercapacitors are not a perfect electrochemical capacitor due to its low energy density than batteries. The reported energy density of EDLC materials (5-10 Wh kg^{-1}) are insufficient to fulfill the requirements for electronic devices (100-250 Wh kg^{-1}) (Yu et al., 2013). One of the ways is choosing appropriate electrolyte to maximize the operating potential as the equation of energy density is $E = ½ (CV^2)$. The energy storage can be increased with increasing the specific capacitance (C) and operating potential (V). Neutral electrolytes are preferable for symmetric supercapacitor due to its lower ionic conductivities and lower corrosive nature when compared to both acid and alkaline electrolytes. Due to the lower ionic conductivities, neutral electrolyte has lower concentration of H^+ and OH^- ions than those using acid and alkaline electrolytes. This may resulting in high overpotentials for H_2 and O_2 evolution reaction and thus wider the potential window.

The exceptional chemical and physical properties of rGO have been long recognized since the discovery of rGO by Geim and Novoselov using "scotch tape method" in 2004. To date, rGO was synthesized using modified Hummers' method under a specific set of environment conditions and have been widely used in supercapacitor applications. rGO has attracted great attention due to its unique properties, such as high surface area (>2600 $m^2 g^{-1}$), high electrical conductivity (2000 S cm^{-1}), and good mechanical stability (Xia et al., 2012). Moreover, good electrical conductivity of rGO can facilitate electron transfer and ion diffusion in metal oxides. However, rGO is still far from becoming a potential candidate for supercapacitor application due to high agglomeration of rGO sheets caused by van der Waals forces. This may reduce its specific surface area for the contact of electrolyte ions into rGO surface. The production of high electrochemical performance of supercapacitor using rGO as working electrode is a great challenge unless several issues have pointed out are addressed.

Another approach to improve the energy density of rGO is incorporating it with fiber-like structure of WO_3 to form nanocomposite electrode as it combined the advantages of individual component. One-dimensional (1D) nanofiber has been proven as an effective way since this architecture provides large specific surface area and high porosity, leadings to a fast reversible redox reaction. Thus, it is indispensable to study the effects of a series of processing parameters on the formation of fiber-like structure of WO_3 on the rGO sheets and their electrochemical performance.

However, in getting the right dimensions and morphologies of nanostructure materials, a controlled synthesis procedure for the production of desired rGO/WO_3 nanocomposite is a must. Therefore, in the present study, considerable efforts have been devoted to the synthesis of desired rGO/WO_3 nanocomposite that could increase the electrochemical performance.

1.3 Objectives of Research

The objectives of this research are listed as follows:

1. To synthesize the P-rGO using modified Hummers' method followed by chemical reduction method.
2. To study the formation of P-rGO/WO_3 nanocomposites via hydrothermal technique (i.e., loading amounts of APT, hydrothermal temperature and reaction time).
3. To study the supercapacitor characteristic (i.e., specific capacitance, energy and power density and cycling performance) of P-rGO/WO_3 nanocomposite and pure WO_3 nanofibers.

1.4 Scope of Research

Many studies highlighted the coupling mechanism between WO_3 and P-rGO to facilitate better electronic transport. However, most scholars mainly focused on the photocatalytic activities rather than supercapacitor applications. Therefore, detailed studies regarding the relationship of WO_3 content incorporated into P-rGO sheets for electrochemical performance has been established in this work. To the best of my knowledge, little information is known regarding the incorporation of WO_3 into P-rGO using hydrothermal technique, especially in supercapacitor application. Thus, a comprehensive study was conducted to optimize hydrothermal parameters (i.e., loadings of APT, hydrothermal temperature and reaction time) to obtained the desired P-rGO/WO_3 nanocomposites, which give best electrochemical performance.

The surface and cross-sectional morphologies of the P-rGO/WO_3 nanocomposites was viewed by field emission scanning electron microscope (FESEM) and high-resolution transmission electron microscope (HRTEM). Energy dispersion X-ray spectroscope (EDX) was used to determine the elemental composition of samples. In addition, X-ray diffraction (XRD) was used to identify the crystallinity structure of the sample. Moreover, the vibrational information specific to the chemical bonds and symmetrical of molecules

in the nanocomposite was determined using Raman spectroscope. Then, the pore structure and surface area of sample was analyzed by nitrogen adsorption-desorption isotherms using Brunauer-Emmett-Teller (BET) method.

The electrochemical performance of the samples were characterized using two-electrode system with P-rGO/WO_3 nanocomposites as the working and reference electrodes. The electrolytes used in the supercapacitor consisted of 1M sodium sulfite (Na_2SO_3) aqueous solution. The two electrodes were connected to potentiostat (Autolab PGSTAT 204), and the specific capacitance and internal resistance were measured.

1.5 Outline of Dissertation

This thesis consists of five chapters. Chapter 1 discusses the research background, problem statements, research objectives, scope of research and an overview of dissertation. Chapter 2 introduces the historical of supercapacitor, storage principles, construction designs and performance assessments. In general, a typical supercapacitor consists of three essential components, namely the electrode, the electrolyte and the separator. A comprehensive review on these components are included in Chapter 2. In Chapter 3, experimental procedures are presents in detail, including the chemicals, precursors and equipment that have been used throughout this research. A series of processing parameters (i.e., mass loading of WO_3 and P-rGO, reaction temperature and reaction time) on the formation of fiber-like structure of WO_3 on P-rGO sheets were studied. Moreover, the operation principles and sample preparation of characterization techniques are briefly explained. Chapter 4 interprets the experimental results and discussions on the formation of GO, rGO, P-GO, P-rGO, fiber-like structure of WO_3 and P-rGO/WO_3 nanocomposites and their electrochemical performance. Chapter 5 summarizes the electrochemical performances of P-rGO, WO_3 and P-rGO/WO_3 nanocomposites and suggested several strategies for future improvement. Such finding

will aid in building the fundamentals of P-rGO modification with WO_3 in the development of supercapacitor for sustainable energy system.

CHAPTER 2: LITERATURE REVIEW

2.1 Introduction

In response to the changing global landscape, energy has become a primary focus of the major world powers and scientific community. There has been great interest in developing and refining more efficient energy storage devices. The hybrid supercapacitor is one of the most promising prospects for efficient electrochemical performance and emerged with the potential to facilitate major advances in energy storage field. To bring this hybrid supercapacitor to the point of commercial readiness and viability in terms of performance and cost, substantial research on the development of high electrochemical behavior of supercapacitor is necessary. Recent studies have reported that rGO/WO_3 nanocomposite has emerged as the leading candidate for supercapacitor electrode due to the advantages of individual active material. However, rGO and WO_3 are still suffered from some disadvantages such as the restacking of rGO and poor conductivity nature of WO_3. Thus, integrating both electrode material can enhance the electrochemical performance of rGO/WO_3 nanocomposite.

The relationship between the rGO and WO_3 as well as their supercapacitor performance was still a matter of debate and remains unclear. It was noted that the properties of this binary oxide primarily depend on the nature of the preparation method and the role of optimum loading content incorporated into the rGO/WO_3 nanocomposite. Therefore, the development of efficient supercapacitor remains to be determined. In the subsequent section, the historical overview, basic principal, material selection and work done by various researchers with regards to the rGO/WO_3 nanocomposite applied in supercapacitor application will be reviewed in detail.

2.2 Historical Overview of Supercapacitor

The early work on capacitor technology was reported by Ewald Georg von Kleist in 1745, which inspired from the invention of Leyden jar. In 1876, Fitzgerald invented a wax-impregnated paper dielectric capacitor with foil electrodes and used in radio receivers (Masoumi and Naderinezhad, 2014). This conventional capacitor composed of two conductive materials that are separated by a dielectric. The dielectric is a non-conducting material that inserted between two electrodes, which can be air (3×10^6 V m^{-1} of dielectric strength) or paper (16×10^6 V m^{-1} of dielectric strength) (Sharma and Bhatti, 2010). The overall capacitance and operating voltage of capacitor are depends upon the dielectric. The discovery of conventional capacitor had brought out lots of great ideas for scientists and researchers, whom seek efficient energy storage devices.

After a few years, Charles Pollak was patented a borax electrolyte aluminium electrolytic capacitor which lead to commercial product in late 1920s. Electrolytic capacitors was then categorized as second generation capacitor, which show similar to the cell design to battery. Electrolytic capacitor, also known as polarized capacitor, which made up of two conductive electrodes (i.e., aluminium, tantalum and niobium) and a paper fully soaked in electrolyte, acting as a separator between electrodes (Jayalakshmi and Balasubramanian, 2008). The particular metal on electrode is coated with an insulating oxide layer, acting as dielectric in electrolytic capacitor. Due to their very thin dielectric oxide layer, a high volumetric capacitance can be achieved by combining sufficient dielectric strength. The destruction of electrolytic capacitor may happen if the polarity is reversed resulting in limited lifespan.

Taking this into account, electrochemical double-layer capacitors (EDLC) are emerged as third generation of capacitor - until now (seen in Figure 2.1). In 1853, the concept of double-layer capacitance was first proposed by a German physicist, Hermann

von Helmholtz. EDLCs stored charge at interface of electrode/electrolyte. With the developing of technology, the first EDLC was then patented by General Electric Company in 1957 but did not commercialize their invention. In 1966, researchers of Standard Oil of Ohio (SOHIO) developed another EDLC and licensing their invention to Nippon Electric Corporation (NEC), which finally introduced to market in 1971, used as power backup in computer memory (Sharma and Bhatti, 2010). These capacitors using activated carbon as the active material for the positive and negative electrodes in aqueous or organic electrolyte. This breakthrough has triggered the subsequent interests in energy storage devices research by scientists and researchers from all over the world on electrode materials as an important component in supercapacitor applications.

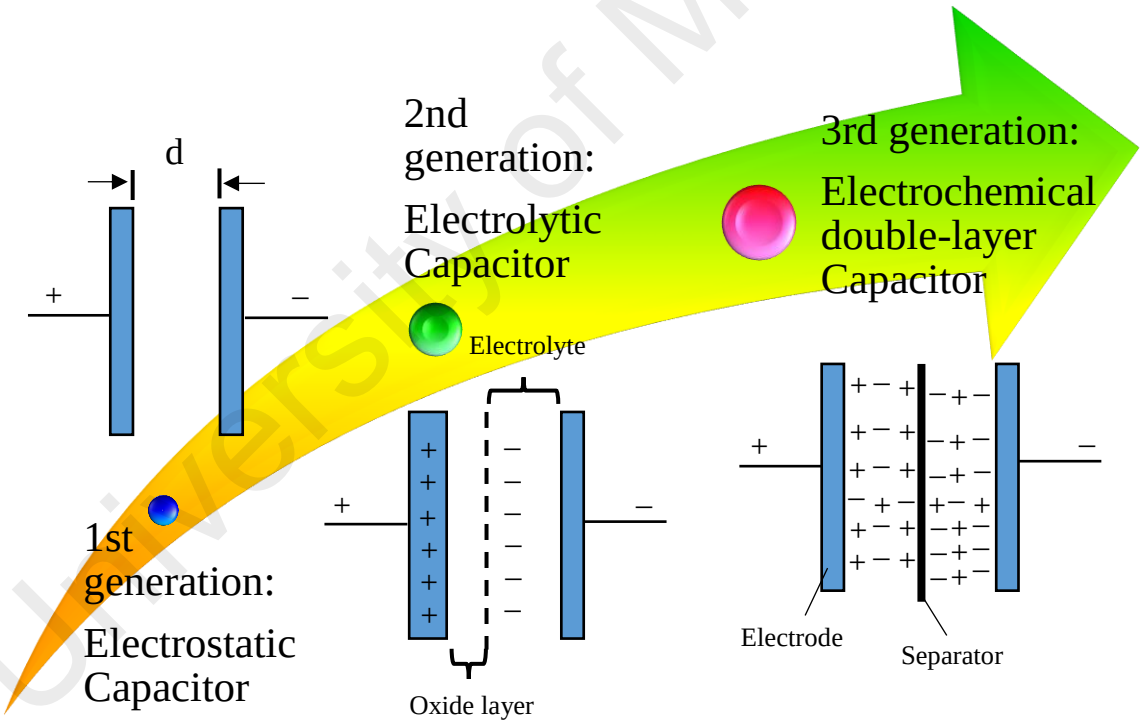

Figure 2.1: Evolution of capacitor (Jayalakshmi and Balasubramanian, 2008).

2.3 Basic Principle of Supercapacitor

Based on their energy storage mechanism, supercapacitors can be classified into three different types, namely electrical double-layer capacitor (EDLC), pseudocapacitor and hybrid capacitor as summarized in Table 2.1 (Sk et al., 2016). EDLC is designed to store

charge electrostatically at the electrode-electrolyte interface through reversible ion absorption (non-Faradaic). Meanwhile, pseudocapacitor relies on Faradaic reaction in which charge occurs at the surface of active materials via reversible redox reaction. On the other hand, hybrid capacitor involves both Faradaic and non-Faradaic process to store charge and believes that it can yield much higher specific capacitance. Their storage methods are being explained as follows:

Table 2.1: Different types of supercapacitor devices (Sk et al., 2016).

Types of supercapacitors		Electrode material	Storage mechanism	Merit	Demerits
Electrochemical double-layer capacitors (EDLCs)		Carbons: ACs, CNTs, rGO	EDLC (non-faradaic)	Long cycle life	Low specific capacitance, energy and power density
Pseudocapacitors		Transition metal oxides and conducting polymers	Redox reaction (faradaic)	High specific capacitance, energy and power density	Short cycle life
Hybrid capacitor	Composite hybrid	Metal oxide/carbon or conducting polymer/ carbon	Faradaic and non-faradaic	High specific capacitance, energy and power density	Slightly shorter cycle life than EDLC
	Asymmetric hybrid	Anode: Metal oxide/ conducting polymer Cathode: carbon	Anode: faradaic Cathode: non-faradaic	High specific capacitance, energy and power density	Slightly shorter cycle life than EDLC
	Battery-type hybrid	Anode: Li-ions material Cathode: carbon	Anode: Lithiation/ de-lithiation Cathode: non-faradaic	High specific capacitance, energy and power density	Slightly shorter cycle life than EDLC

2.3.1 Electrical Double-layer Capacitor (EDLC)

EDLC, double-layer charge storage is surface process and thus making it high reversible and longer the cycle life of supercapacitor. No electrochemical reaction involves between the interface of electrode and electrolyte. Several models are develop for the concept of electrical double layer, including Helmholtz model, Gouy-Chapman model and Stern model (Zhang and Zhao, 2009). Helmholtz model is the earliest model of electrical double layer, which proposed that the charge at electrode surface is neutralized by forming a double layer of counterions at a distance. Gouy and Chapman further modified the Helmholtz model, suggesting that the distribution of ion is determined by thermal motion, called diffusion layer. But, this model overestimated the electrical double layer capacitance and thus Stern combined Helmholtz model and Gouy-Chapman model, suggesting two regions of ion distribution, which are inner Helmholtz plane (IHP) and outer Helmholtz plane (OHP). In Stern layer, specifically adsorbed ions accumulated on IHP while non-specifically adsorbed ions attached on OHP upon polarization as illustrated in Figure 2.2 (Frackowiak et al., 2013).

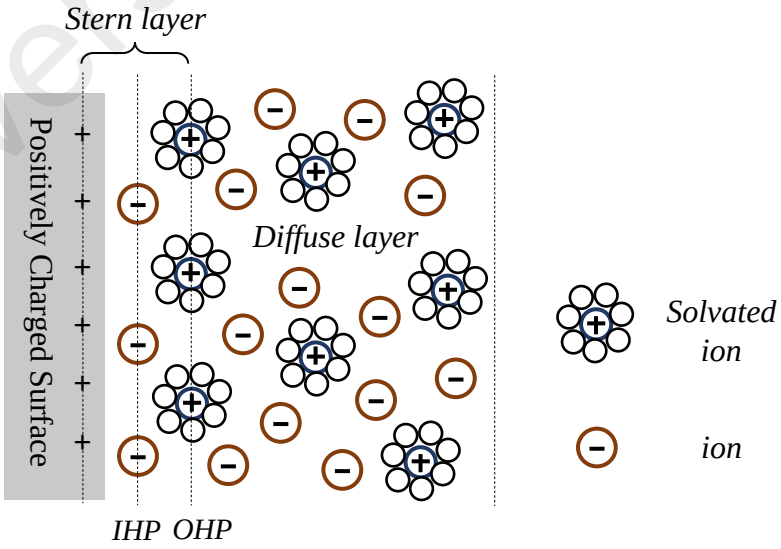

Figure 2.2: Model of electrical double-layer at positively charged surface with its ions and structure (Frackowiak et al., 2013).

EDLC normally utilizing material with high porous and surface area, which are carbon-based materials such as activated carbon (AC), carbon nanotubes (CNTs) and reduced graphene oxide (rGO). Among them, rGO is generally attractive as electrode materials since 2004 due to its incredible properties and structures that plays vital role in electrochemical performance.

2.3.2 Pseudocapacitor

Another type of supercapacitor is pseudocapacitor, generates capacitance via three faradaic process: (i) reversible adsorption; (ii) redox reaction of transition metal oxides; and (iii) electrochemical doping-undoping of conducting polymer (Burke, 2000). Pseudocapacitor possess larger specific capacitance (10-100 times higher) and energy density as compared with EDLC. Nevertheless, redox reaction usually slower than that of the non-faradaic process, which resulting in low power density and instability during cycling process. The most commonly known pseudocapacitance active materials are transition metal oxides such as ruthenium oxide, zinc oxide, magnesium oxide, tungsten oxide etc. and conducting polymers including polyaniline, polypyrrole etc.

2.3.3 Hybrid Capacitor

Hybrid capacitor, generally comprised more than one active species in single device, simultaneously. By combining different active materials, hybrid capacitor can be categorized into three types: composite hybrids, asymmetric hybrids and battery-type hybrids (Yu et al., 2013). In composite hybrids, different capacitive behavior material are combined in single electrode. For example, incorporation of EDLC/EDLC, pseudo/pseudo or EDLC/pseudo in single electrode symmetric hybrids. Mean, two electrode are identical in supercapacitor device. Asymmetric hybrid involves two storage mechanisms in different electrode, carbon-based as cathode and transition metal oxides or conducting polymer as anode. Another type of hybrid, referred to battery-type hybrid,

electrode configuration similar to asymmetric hybrid. The most famous battery-type hybrid, lithium-ion batteries, where Li-ions undergoes reversible intercalated and de-intercalated from/to anodes during charge/discharge process (Lukatskaya et al., 2016). It is worth mentioning that these hybrid capacitors able to overcome the major drawbacks of EDLC and pseudocapacitor. The operating voltage of hybrid capacitor can be larger than EDLC and pseudocapacitor leading to high energy and power density.

2.4 Construction Designs

Supercapacitor consists of three main basic components, namely electrode, electrolyte and separator. Electrode materials considered as the major factor to determine the performance of supercapacitor based on their storage mechanisms (electrical double-layer capacitance and pseudocapacitance). Besides that, electrolytes also have an obvious effect on capacitor characteristics. This is because electrolyte controls the potential window that influence the capacitance, energy density, power density and cycling stability of supercapacitor (Staaf et al., 2014). The effects of electrolyte on electrochemical performance will be discussed in detail in section 2.7. Separator serves as barrier forbids the electronic conductance but allows the mobility of the charged ions.

2.5 Performance Assessments

Evaluating the capacitance value of supercapacitor is important to serve as a trademark and gives the information of where tested materials would meet the requirement as electrode material. A series of tests and their equations are listed in Table 2.2 to calculate the capacitance, energy density and power density of supercapacitor (Faraji and Ani, 2015).

Table 2.2: Performance assessment of supercapacitor using different characterization techniques

Characterization technique	Equations	Remarks
Cyclic Voltammetry	$C = \frac{\int idt}{dV \times SR}$	• Used in 3 electrode system • Redox peaks are notable and repeating deviation
Galvanostatic charge/discharge	$C = \frac{I \times dt}{dV}$	• Best determines from slope of discharge curves
Energy density	$E = \frac{1}{2}CV^2$	• Describes the amount of energy which can be stored • Assessment of practical performance
Power density	$P_{max} = \frac{V^2}{4ESR}\ or \frac{E}{t}$	• Describes the speed at which energy can be delivered • Assessment of practical performance

* *C*= capacitance; *dV*= change in potential; *SR*= scan rate; *I*= current; *dt*= discharge time; *E*= energy density; *V*= voltage; *P*= power density; *ESR*= equivalent series resistance.

2.6 Electrodes

2.6.1 Material Selection for EDLC

Taking into account of the storage mechanisms that involved in the EDLC, the materials used as EDLC's electrode must satisfy several functional requirements with respect to electrochemical properties as shown below: (i) high specific surface area for the access of electrolyte ions during charging process; (ii) high electrical conductivity to reduce the internal resistance; (iii) regulation of pore size distribution to match the size of electrolyte ions; and (iv) interconnecting pores for ions diffusion and contact.

Various potential carbon electrodes have been identified as attractive materials for stable and highly efficient electrode such as AC, CNTs and rGO, which will be discussed in the following sub-sections.

2.6.1.1 Activated carbon (AC)

Activated carbon (AC) is well known carbonaceous electrode material for EDLC application, due to its hold several unique properties including high surface area (1000-

2500 m^2 g^{-1}), low cost, high electronic conductivity and excellent chemical stability (Liew et al., 2016). Traditionally, AC are mainly produced from expensive and non-renewable energy resources such as petroleum, coal and their derivatives (Han et al., 2017). Considering the cost, conversion of low cost and renewable resources into AC is highly recommended. Nowadays, more and more researchers have explored biomass for preparing AC including corn stalk, animal's feather, bagasse, fungi, hemp and used in supercapacitor as summarized in Table 2.3 (Elmouwahidi et al., 2017).

Table 2.3 shown that the specific capacitance of AC is strongly influenced by the specific surface area of AC materials especially to its porous structure and size. However, porous AC supercapacitor usually suffer from slow kinetics related to its microporous, which lower the accessible surface area for the penetration of electrolyte ions and produces a high internal resistance of capacitor (Liew et al., 2016). As well known, AC is composed of micro, meso and macropores. Consequently, low specific capacitance and power density of supercapacitor have been obtained for available AC supercapacitor. Therefore, the development of new materials to overcome the major drawbacks of AC are needed.

2.6.1.2 Carbon nanotubes (CNTs)

Carbon nanotubes (CNTs) are 1D carbonaceous materials and known as promising candidates to replace activated carbon as electrode material in supercapacitor applications. Compared to AC, CNT possesses excellent conductivity (~5000 S cm^{-1}) but lower surface area (100-1315 m^2 g^{-1}) are reported (Chen and Dai, 2013). Owing to its excellent conductivity, CNT have been studied by researchers in supercapacitor application. For examples, Kim et al. (2006) synthesized multi-walled carbon nanotube (MWNT) via electrostatic spray deposition onto metallic substrate, which showed a specific capacitance of 108 F g^{-1} under scan rate of 10 mV s^{-1}.

Table 2.3: A summary of synthesized AC electrode using different biomass resources for supercapacitor application.

Precursors	Synthesis method	BET surface area (m^2 g^{-1})	Specific capacitance (F g^{-1})	Current density/ Scan rate	Remarks	Ref.
Bagasse	Hydrothermal carbonization with KOH activation	2296	320	0.5 A g^{-1}	Bagasse-derived hierarchical structured carbon (BDHSC) presented the highest surface area for the accommodation of large amount of charges.	(Feng et al., 2016)
Rubber wood sawdust	Pre-carbonized followed by CO_2 activation	683.63	33.74	1 mV s^{-1}	AC pellets exhibited low specific capacitance owing to its low surface area.	(Taer et al., 2010)
Oil palm empty fruit bunches	Carbonization with CO_2 + KOH activation	1704	150	10 mA cm^{-2}	AC exhibited high specific surface area by optimizing activation time.	(Farma et al., 2013)
Bamboo	Heat treatment with KOH activation	3061	258	0.1 A g^{-1}	The bamboo-based AC exhibited the highest specific capacitance due to its high surface area.	(Yang et al., 2014)
Waste tea-leaves	Carbonization with KOH activation	2841	330	1 A g^{-1}	The high specific capacitance of AC was attributed to its high specific surface area and abundant oxygen-containing group. Thus, EDL capacitance and pseudocapacitance behavior was obtained in AC.	(Peng et al., 2013)
Hemp stem hemicellulose	Carbonization with KOH activation	3062	318	0.1 A g^{-1}	The sphere-like architectures of the AC exhibited abundant mesopores make electrolyte ions diffuse in and out of the electrode.	(Wang et al., 2015b)

Moreover, An and his research group proposed the single-walled carbon nanotube (SWNT) electrode synthesized using DC arc discharge, which delivered a maximum specific capacitance of 180 F g^{-1} at current density of 1 mA cm^{-2} (An et al., 2001). This condition might be attributed to its high specific surface area (357 m^2 g^{-1}) and the pore diameters are in range of 30-50 Å (mesopores). CNT prepared by chemical vapor deposition (CVD) achieved 115.7 F g^{-1} at scan rate of 100 mV s^{-1} due to the low contact resistance between CNT and graphite foil (Chen et al., 2002). Nonetheless, CNT-based supercapacitors did not achieve the expected performance (low specific capacitance as compared to AC and rGO). This explains why CNT hybrids is reported elsewhere in composite form (e.g. CNT/graphene, CNT/metal oxides and CNT/conducting polymers).

2.6.1.3 Reduced graphene oxide (rGO)

In fact, rGO is a single layer sheet of sp^2-bonded carbon atoms arranged in honeycomb crystal lattice, has gained huge attention as electrode material due to its good electrochemical stability, high surface area (> 2600 m^2 g^{-1}), fast ions diffuse to its structure and good mechanical property (Bo et al., 2012). Taking these facts into account, a recent literature review on the rGO electrode adopted in various forms of supercapacitor application was presented in Table 2.4.

A wide variety of synthesis methods have been used in the preparation of rGO, including chemical, thermal, electrochemical, and microbial/bacterial as shown in Table 2.4 (Bianco et al., 2013). Prior reduction treatment, graphite powder, a precursor of rGO undergoes oxidation reaction to form graphite oxide using modified Hummers' method. This oxidation process helps to increase the interlayer spacing between graphene sheets in graphite powder by introducing oxygen functional groups such as hydroxyl, epoxides, carboxyl and carbonyl as illustration in Figure 2.3 (Emiru and Ayele, 2017).

Table 2.4: The electrochemical performance of rGO supercapacitor.

Sample	Reduction method	Specific capacitance ($F\ g^{-1}$)	Current density/ Scan rate ($A\ g^{-1}$)	Remarks	Ref.
rGO	Thermal reduction	260.5	0.4	A lot of oxygen functional groups still present on the surface of rGO, which contribute the pseudocapacitance.	(Zhao et al., 2012)
rGO	Electrochemical reduction	150.4	5	The enhanced specific capacitance of rGO due to more electrochemically active surface area.	(Shao et al., 2010)
rGO	Electrochemical reduction	128	212.16	rGO displayed high specific capacitance due to removal of functional group help to increase the surface contact for ions.	(Peng et al., 2011)
rGO	Alkaline hydrothermal reduction	145	0.5	High electrochemical capacitance may attributed to the large sp^2 domains of rGO which benefit the ion mobility and lower charge transfer resistance.	(Perera et al., 2012)
rGO	Chemical reduction (Hydrazine)	135	0.01	High electrical conductivity of rGO give rise to the stable electrochemical performance over a wide range of scan rates.	(Stoller et al., 2008)
rGO	Chemical reduction (Hydrazine)	205	0.1	High specific capacitance owing to the high accessibility of electrolyte ions and high electrical conductivity (100 $S\ m^{-1}$).	(Wang et al., 2009)
rGO	Chemical reduction (Hydrazine)	154.1	1	High specific surface area that can be readily accessed by electrolyte ions.	(Liu et al., 2010)
rGO	Chemical reduction (HBr)	348	0.2	Remarkably specific capacitance due to rGO facilitates the penetration of aqueous electrolyte and the stable oxygen groups introduce pseudocapacitive effects.	(Chen et al., 2011)
rGO	Chemical reduction ($NaBH_4$)	135	0.75	rGO thin film electrode showed high specific capacitance due to high accessibility of surface area resulting in improved charge transfer kinetics.	(Yu et al., 2010)

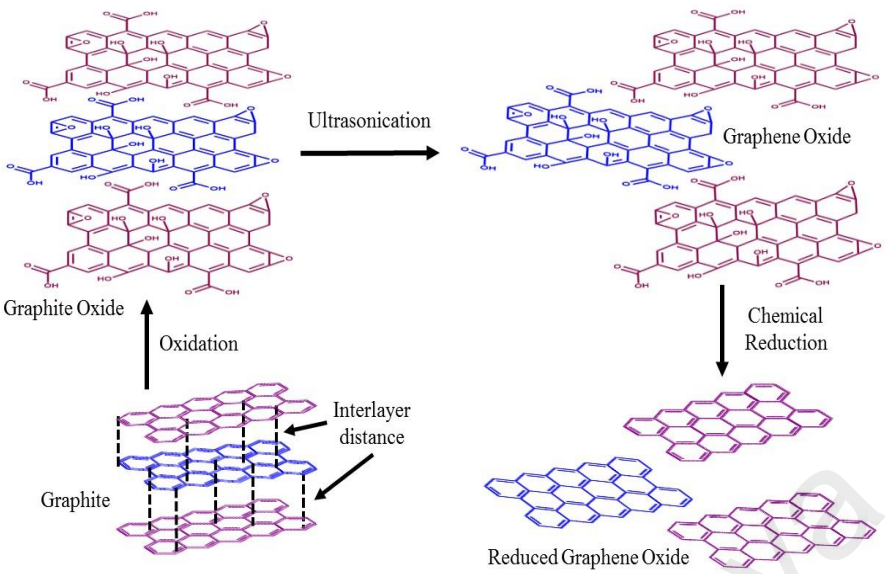

Figure 2.3: Synthesis of reduced graphene oxide via chemical reduction method (Chua and Pumera, 2014).

Chemical reduction, a scalable technique, towards the production of reduced graphene oxide (rGO) from graphene oxide (GO), which normally sustaining the solution at low temperature in range of 85-100 ºC. GO is an exfoliated form of graphite oxide and prepared through ultrasonication methods in deionized water. The transformation of GO to rGO is normally indicated by a color change from brown to black. In this process, a vast number of reducing agents have been used to synthesis rGO, including thiourea, hydrazine, borohydrides, hydrohalic acid, metal-alkaline and others (Chua and Pumera, 2014). Such reducing agents are reported to produce high deoxygenation degrees of rGO.

GO can be thermally treated to form rGO at high temperature of 1000 ºC or more in tube furnace in the presence of inert gas, which generated pressure to overcome the van der Waals force that occur between graphene sheets. However, large energy consumption is the major drawback of thermal reduction (Zhang et al., 2011). Moreover, electrochemical reduction technique, known as cyclic voltammetry (CV)-reduced GO, are reported to produce rGO by directly deposited it in GO suspension onto a substrate surface (Zhang et al., 2016c). The resulted rGO showed a similar structure as compared

to the pure graphene. Nevertheless, it is difficult to deposit a large amount of rGO onto the electrode surface.

Based on the literature studies, it could be summarized that the experimentally measured capacitance of rGO are much lower than the expected value owing to the agglomeration of graphene sheets caused by its strong van der Waals force, which lower the contact surface area for the electrolyte ion. Unlike AC, the specific surface area of rGO is depends on the layers instead of the distribution of pores. Therefore, combining rGO and others material to form nanocomposite has gained great interest for application.

2.6.2 Material Selection for Pseudocapacitor

2.6.2.1 Conducting polymers

To build high performance supercapacitor with high specific capacitance and energy density, many researchers have been devoting their time to investigate the utilization of conducting polymers. Conducting polymers offer several advantages such as intrinsic conductive, inexpensive, ease of preparation, flexibility and good specific capacitance (Li et al., 2005). Typical conducting polymers include polyaniline (PANI), polypyrrole (PPy), poly(3,4-ethylenedioxythiophene) (PEDOT), polythiophene (PTh), poly(3.4-propylenedioxy thiophene) (PProDOT), polyacetylene (PA), poly(phenylenevinylene) (PPV) etc.

Among the various conducting polymers, PANI has received much attention due to its multiple redox state resulting in high pseudocapacitance. For example, the specific capacitance of vertical aligned PANI achieved 950 F g^{-1} at current density of 1 A g^{-1} in aqueous electrolyte (Wang et al., 2010). This remarkable enhancement may attributed to the PANI aligned perpendicular to the substrate which provides effective diffusion channels for electrolyte ions. Robert et al. (2009) synthesized poly(tris(4-(thiophen-2-yl)phenyl)amine) (pTTPA) films via a three-fold Stille coupling reaction, which

demonstrated high specific capacitance of 990 F g^{-1} in organic electrolyte at scan rate of 50 mV s^{-1}. The specific capacitance of PEDOT nanotube is approximately 132 F g^{-1} at scan rate of 100 mC cm^{-2} (Liu et al., 2008). Conducting polymers showed remarkably high specific capacitance, but restricted by its low mechanical stability such as fast volumetric swelling and shrinking during electrochemical doping-undoping (Wang et al., 2012). This volumetric interchange destroy the structure of sample resulting in low cycle life. Therefore, design and development of transition metal oxides as electrode material has gained significant scientific interest and become the most studied material as it exhibits promising functional properties in capacitor system.

2.6.2.2 Transition metal oxides

In this manner, the use of transition metal oxides as electrode materials in pseudocapacitor was extensively explored, such as RuO_2, MnO_2, Fe_2O_3, WO_3, NiO, Co_3O_4, SnO_2 etc. probably because of their various oxidation states for redox reaction. Conway et al. (1991) claimed that redox reaction involved in RuO_2 material require successive electron transfer such as Ru^{2+}, Ru^{3+} and Ru^{4+} at metal. It was found that RuO_2 is the most promising candidates for supercapacitor owing to its superior pseudocapacitance, high reversible charge/discharge and good cyclic stability (Gujar et al., 2007). Unfortunately, RuO_2 is high cost, toxic in nature and less abundant, which restricted their commercial use. Herein, there is a solid motivation to discover alternative electrode materials, which are cheaper and show similar pseudocapacitance behavior as RuO_2. Table 2.5 summarized the pseudocapacitance behavior of several promising transition metal oxides active electrode applied in supercapacitor.

Table 2.5: The pseudocapacitance behavior of several transition metal oxides active electrode applied in supercapacitor.

Materials	Synthesis method	Remarks	Ref.
Co_3O_4	Hydrothermal	The specific capacitance of hollow Co_3O_4 nanowire was found to be 599 F g^{-1} in 1M KOH at current density of 2 A g^{-1}. This large value is attributed to the unique porous architecture provided large surface area for penetration of electrolyte ion.	(Xia et al., 2011)
MnO_2	Electrospinning	The MnO_2 electrode possessed a high specific capacitance of 645 F g^{-1} at current density of 0.5 A g^{-1} due to its nanofibrous structure, which offered a short channels for ion diffusion.	(Li et al., 2013)
NiO	Hydrothermal	NiO nanocolumns showed high supercapacitance of 686 F g^{-1} at current density of 1 A g^{-1}. The reason may be that superior surface area and small pores, which benefited the diffusion of ions into electrode.	(Zhang et al., 2010)
SnO_2	Hydrothermal	The specific capacitance values calculated from discharge curve are 548 F g^{-1} at current density of 1 A g^{-1} for hollow SnO_2 microspheres. The unique hollow architecture of SnO_2 and its high surface area led to an improved pseudocapacitance.	(Ren et al., 2014)
Fe_2O_3	Sol-gel	α-Fe_2O_3 electrode exhibited high specific capacitance (193 F g^{-1} at current density of 1 A g^{-1}) owing to its porous nature possessed high surface area.	(Shivakumara et al., 2014b)
WO_3	Hydrothermal	The specific capacitance of WO_3 is 797.05 F g^{-1} at current density of 0.5 A g^{-1}. The improved specific capacitance probably because of its mesoscopic structure, which provided more reactive sites for redox reaction.	(Xu et al., 2015)

Among the vast number of different transition metal oxides, tungsten trioxide (WO_3), an *n*-type semiconductor, is one of the most capable candidates for enhancement in electrochemical performance of supercapacitor applications because of its high intrinsic densities, high mechanical stability and good electrochemical redox characteristic (Liang et al., 2013). It is a well-known fact that WO_3 has several distinct crystalline polymorphs, namely monoclinic, triclinic, tetragonal, orthorhombic, cubic and hexagonal phases. By comparing the crystal structure of WO_3 in Table 2.6, hexagonal WO_3 (h-WO_3) is the most notably material as electrode material for supercapacitor due to its tunnels are effective for insertion of electrolyte ions and a high pseudocapacitance was obtained. h-WO_3 consists of WO_6 octahedral and arranged in six-membered ring by sharing corner oxygens to form hexagonal axis as illustrated in Figure 2.4 (Sun et al., 2015). Stacking of such layers resulted in the formation of hexagonal tunnels.

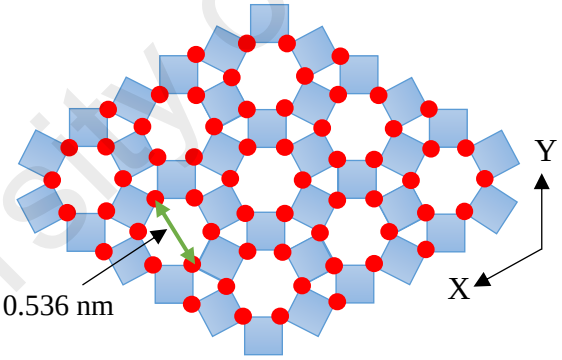

Figure 2.4: Crystal structure of h-WO_3 (Sun et al., 2015).

Nonetheless, an obvious hindrance to the widespread use of WO_3 as an active electrode in capacity system is its low electrical conductivity and poor cycle stability. Considering this fact, incorporation of WO_3 with other conductive materials such as carbon materials to fabricate composite as promising active electrode in supercapacitor is highly recommended.

Table 2.6: Comparison of the electrochemical properties of WO_3 supercapacitor and its different crystal structure.

Sample	Synthesis method	Morphology	Crystal structure	Specific Capacitance	Cycling stability	Ref.
WO_3	Hydrothermal	Microspheres	Hexagonal	797.05 F g^{-1} at current density of 0.5 A g^{-1}	100.47% capacitance retention after 1000 cycles	(Xu et al., 2015)
h-WO_3	Hydrothermal	Aligned nanopillar bundles	Hexagonal	421.8 F g^{-1} at current density of 0.5 A g^{-1}	Retained almost 100% within 1000 cycles	(Zhu et al., 2014)
WO_3	Hydrothermal	Nanofibers	Hexagonal	539.42 F g^{-1} at current density of 2 A g^{-1}	Retained 79.1% of initial capacitance after 6000 cycles	(Yao et al., 2017)
h-WO_3•nH_2O	Hydrothermal	Nanorods	Hexagonal	496 F g^{-1} at scan rate of 5 mV s^{-1}	N/A	(Chen et al., 2015)
WO_3-WO_3•0.5H_2O	Microwave-assisted hydrothermal	Disordered nanorods	Hexagonal and cubic	293 F g^{-1} at scan rate of 25 mV s^{-1}	72% capacitance retention after 100 cycles	(Chang et al., 2011)
m-WO_{3-x}	Template-assisted	Mesoporous	Cubic	199 F g^{-1} at current density of 1 mA cm^{-2}	Remained almost 95% within 1200 cycles	(Yoon et al., 2011)
WO_3	Microwave irradiation	Amorphous	Amorphous	231 F cm^{-3} at current density of 1 A g^{-1}	N/A	(Huang et al., 2009)
WO_3	Successive ionic layer adsorption and reaction (SILAR) method	Irregular rods	Monoclinic	266 F g^{-1} at scan rate of 10 mV s^{-1}	Remained 81% of initial capacitance after 1000 cycles	(Shinde et al., 2015)

2.6.3 Symmetric Hybrid Capacitor

Over the past few years, hybrid capacitor has gained much attention and has been intensively studied because of the unique features of high specific capacitance and excellent cycling performance. As mentioned above, rGO has its own merits and demerits. Fabrication of rGO/metal oxide composites has proved to be an effective way to improve the performance of rGO-based supercapacitor as it combined the advantages of both materials. Herein, a vast number of rGO/WO_3 composites and their electrochemical behavior are demonstrated in detail in following paragraphs.

2.6.3.1 rGO/WO_3 hybrids

Up to now, numerous literature reviews on rGO/WO_3 composites and their electrochemical performances are reported. A number of synthesis approaches such as hydrothermal, reflux and electrostatic self-assembly method, have been applied to prepare rGO/WO_3 composites for supercapacitor application. Among all of these methods, hydrothermal technique is the most feasible due to its advantages of low energy consumption, simple experimental setup, no toxic chemical involved, large-scale production and short reaction time (Mirghni et al., 2017). In general, composites are formed by dissolving precursors and additives in water, which being heated in sealed Teflon lined stainless-steel autoclave to desired temperature. The applied temperature is normally in range of 100-200 ºC (limitation of Teflon-lined) and pressured will automatically generated in a confined place (Yang et al., 2013). Others than temperature, the reaction time, type of precursor/salt, and solvents are the main factors to control the morphology of metal oxides.

Xing and her co-workers prepared WO_3 nanoparticles and dispersed it on rGO using hydrothermal technique, which demonstrating excellent specific capacitance of 580 F g^{-1} than pure WO_3 (255 F g^{-1}) at current density of 1 A g^{-1} in 2 M KOH electrolyte

(Xing et al., 2016). The improved capacitance of rGO/WO_3 composite ascribed to its large specific surface area and high electrical conductivity, which promotes ions diffusion and charge transfer kinetic. Ma et al. (2015) also synthesized rGO/WO_3 composite through hydrothermal method using sodium tungstate (Na_2WO_4•$2H_2O$) as WO_3 precursor. At current density of 1 A g^{-1}, the resulted WO_3•H_2O electrode exhibited a specific capacitance of 140 F g^{-1} while composite demonstrated much higher specific capacitance of 244 F g^{-1}. The enhanced specific capacitance of composited is because of the synergistic effect of rGO and WO_3•H_2O.

In addition, Chu et al. (2017) fabricated rGO/WO_3 composite via an electrostatic attraction between positive charge of surfactant modified-WO_3 and negative charge of GO. The WO_3 was first prepared using hydrothermal method and Na_2WO_4•$2H_2O$ used as precursor. The specific capacitance of rGO/WO_3 composite and pure WO_3 is 495 and 127 F g^{-1} at current density of 1 A g^{-1}, respectively. This may attributed to the synergistic effects of conductive rGO and WO_3.

Furthermore, rGO/WO_3 also can be synthesized using reflux by adding glucose reduced rGO and WO_3 precursor (Na_2WO_4•$2H_2O$), which exhibited specific capacitance of 140.8 F g^{-1} at current density of 0.3 A g^{-1} (Cai et al., 2014). In contrast, the specific capacitance of WO_3-WO_3•H_2O mixture is 24.5 F g^{-1}, which is almost six times lower than the composite. This results indicated that the addition of conductive rGO could enhanced the electrolyte ion mobility in electrode.

These reports suggest that the enhancement in specific capacitance of rGO/WO_3 composites owing to their new functionalities and properties as summarized below: (i) 2D graphene acts as support to facilitate the nucleation and growth of metal oxide with well-defined structures; (ii) metal oxide anchored on rGO can prevent the agglomeration/restacking of rGO (vice versa), resulting in an increase of electroactive

sites and long cycle life; and (iii) high conductive rGO also act as conductive framework to enhance the ion mobility.

2.7 Liquid Electrolytes

In other word, electrolyte is electrolyte salt and solvent, containing cations and anions that will react towards cathode and anode electrode by applying voltage. Electrolyte is one of the key component bring significantly impacts on electrochemical performance of supercapacitor in term of capacity, power density, energy density and cycle life. Various factors for an electrolyte in supercapacitor including: (i) the voltage window; (ii) the ion type and size; (iii) the ion concentration; (iv) the interaction between ion and solvent; and (v) the interaction between electrolyte and electrode should be concerned with respect to the supercapacitor performance (Wang et al., 2012).

In liquid electrolytes, there are further grouped into aqueous and non-aqueous electrolyte (Zhong et al., 2015) as presented in Figure 2.5. For aqueous electrolytes, acid, alkaline and neutral electrolyte are extensively used in the application of supercapacitor due to its high conductivity, smaller size of ions, and high mobility than non-aqueous electrolytes (Zhang et al., 2012). Organic electrolyte, ionic liquid and mixtures of organic and ionic liquid are being employed as non-aqueous electrolytes, which allows operating a supercapacitor with potential window up to 2-3 V.

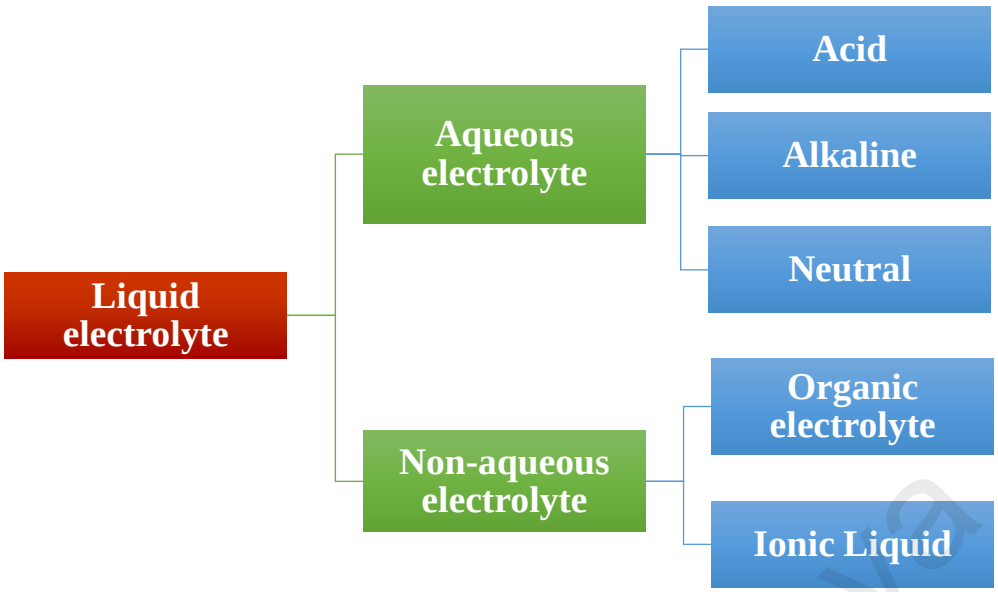

Figure 2.5: Classification of electrolytes for supercapacitor applications.

2.7.1 Aqueous Electrolytes

Supercapacitor using aqueous electrolytes exhibits high capacitance due to the fact that aqueous electrolyte are higher conductivity and smaller ionic radius than non-aqueous electrolyte. However, it suffers from low operating voltage, which restricted by the decomposition of water at about 1.23 V (Béguin et al., 2014). Consequently, the energy that can be stored in supercapacitor is lower in comparison to non-aqueous electrolyte. According to equation of energy density, $E = \frac{1}{2}CV^2$, the energy storage can be increased with increasing the specific capacitance and operating voltage (Zhang et al., 2016a).

In consideration of cycle life, energy and power density, neutral electrolyte are high choice for symmetric supercapacitor due to its lower ionic conductivities and lower corrosive nature when compared to both acid and alkaline electrolytes. Due to the lower ionic conductivities, neutral electrolyte has lower concentration of H^+ and OH^- ions than those using acid and alkaline electrolytes. This may resulting in high overpotentials for H_2 and O_2 evolution reaction and thus wider the potential window is expected. For example, Shivakumara and his co-workers reported that symmetric carbon/carbon

supercapacitor using Na_2SO_4 aqueous electrolyte could cycled for 3000 cycles even at 1.6 V of voltage window (Shivakumara et al., 2014a). Nitrogen doped carbon nanofibers supercapacitor exhibited high energy density of 29.1 Wh kg^{-1} at power density of 450 W kg^{-1} and a high voltage window of 1.8 V was obtained in Na_2SO_4 electrolyte (Zhao et al., 2013). Chae and Chen (2012) used neutral electrolyte, K_2SO_4 in carbon-carbon supercapacitor can charge up to 1.9 V and it still can maintained 85% of capacitance after 10 000 charge/discharge cycles. It was thus concluded that neutral electrolytes can operate safely even excess the limitation of water decomposition. The maximum voltage of neutral electrolyte-based supercapacitor are remarkably higher than acid and alkaline electrolyte (0.8-1 V) for carbon-based supercapacitor (Wang et al., 2015a; Xie et al., 2016). Therefore, neutral electrolyte would be preferable to develop high energy supercapacitor.

Unfortunately, the low ionic conductivities result in an increase of ESR value, therefore lower specific capacitance is found using neutral electrolyte. In contrast, acid and alkaline electrolytes have higher specific capacitance as compared to neutral electrolyte due to its high ionic conductivity. It should be emphasized that the ionic conductivity is greatly dependent on the concentration of electrolyte, suggesting too high or too low concentration of electrolyte will reduced the ionic conductivity. For example, alkaline electrolyte, KOH is usually in high concentration (6 M KOH) whereas neutral and acid (H_2SO_4) electrolyte used in supercapacitor are normally prepared in low concentration such as 0.5 M or 1 M (Mishra and Ramaprabhu, 2011; Tian et al., 2015). The major drawback of acid and alkaline electrolyte is their high corrosive nature (Fic et al., 2016). The corrosive character of acid and alkaline electrolytes were reported to decrease the cycle life of active material due to corrosion at current collector surface, leading to the peeling off of active material from current collector.

With respect to improve the working voltage of aqueous electrolyte, one of the most intensive approaches is to fabricate asymmetric capacitor by employing one electrode consists of EDLC material and another made from pseudocapacitive material. As a consequence, different potential window of the two electrodes are able to increase the operating voltage in the cell (Yan et al., 2012). A hybrid system using MnO_2 as positive electrode and activated carbon as negative electrode was constructed by Khomenko et al. (2006), showing the cell voltage could be extended up to 2 V in KNO_3 aqueous electrolyte. Moreover, Chen et al. (2014) fabricated ternary $Ni(OH)_2$-MnO_2-rGO/FrGO asymmetric supercapacitor exhibits superior capacitive behavior at 0-1.6 V of potential window using KOH as electrolyte. Another approaches are utilize electrode material possess high overpotentials for H_2 and O_2 evolution reaction, such as carbonaceous materials.

2.7.2 Non-aqueous Electrolytes

2.7.2.1 Organic

Organic electrolyte is generally consisting of conductive salt dissolved in organic solvent such as tetraethylammonium tetrafluoroborate (TEA-BF_4) dissolved in acetonitrile (ACN) or propylene carbonate (PC) solvent. Organic electrolytes are being adopted for commercial supercapacitor owing to their relatively high stability operating voltage in range of 2.5 to 2.8 V (Chae and Chen, 2014). The large potential window have a great advantage in improving energy and power densities. For example, fluorine-rich nanoporous carbon (FNC) is prepared via KOH activation process combined with F doping approach (washing with HF and nitric acid), the product exhibits high energy density and high power density of 42.2 Wh kg^{-1} and 134.9 W kg^{-1} in TEA-BF_4/PC electrolyte, respectively (Zhou et al., 2016). Brousse et al. (2016) reported the titanium carbide (TiC) on carbide derived carbons (CDC) film exhibits high energy density of 90 µWh cm^{-2} in 1-ethyl-3-methylimidazolium tetrafluoroborate (EMI-BF_4)/ACN

electrolyte. Although having higher potential window than aqueous electrolytes, organic electrolytes suffer from several demerits which limit their implementation in supercapacitor. Correspondingly, organic electrolytes show high preparation cost, which may attributed to the complicated purification process for removing any residual impurities such as water. Few ppm of water in organic electrolyte could cause the deterioration of electrochemical performance in term of potential range and cycle life (Azaïs et al., 2007). It also suffers from safety concern due to high flammable and volatile of organic solvents when used at high temperature especially ACN with low flash point (5 ºC) and high toxicity (Lin et al., 2011). The used of solvent-free ionic liquid electrolyte may solve the safety issue of organic electrolyte for high temperature applications. Furthermore, another drawback of organic electrolyte is their lower ionic conductivity as compared with aqueous electrolyte. This is associated with the fact that organic electrolytes are commonly exhibited low dissociation degree values resulted in low ionic conductivity and thus increased the ESR value.

2.7.2.2 Ionic liquid

Ionic liquids, also known as room temperature molten salts with melting points lower than 100 ºC, which usually affects by the size and symmetry of cations. Ionic liquids are generally composed of asymmetric organic cations and inorganic/organic anions, which show several advantages including wide potential window (> 3 V), almost zero vapour pressure, and high thermal stability (up to 350 ºC) (Fu et al., 2011; Tsai et al., 2013). Considering these facts, ionic liquid emerged as a promising electrolyte in boosting the energy density of supercapacitor. For instance, Lei et al. (2013) demonstrated the large potential window of 0-3.5 V of the 1-ethyl-3methylimidazolium tetrafluoroborate (EMIM-BF_4) offers rGO-mesoporous carbon (CMK-5) supercapacitor a very high energy density of 60.7 Wh kg^{-1} and power density of 10 kW kg^{-1}. rGO/CMK-5 electrode in EMIM-BF_4 ionic liquid show higher energy densities of 18.8 W h kg^{-1} than $LiPF_6$ organic

electrolyte (8.1 Wh kg^{-1}) and aqueous KOH electrolyte (1.9 Wh kg^{-1}). Moreover, the high viscosity of ionic liquid would slower the ions to access to the electrode during high scan rates or high charge/discharge rates and resulted in high ESR value.

A number of ionic liquids have been used in supercapacitor applications, which are cyclic amines (i.e., pyrrolidinium, imidazolium) and aliphatic quaternary ammonium salts (tetralkylammonium) with anions such as tetrafluoroborate, hexafluorophosphate, bis(trifluoromethanesulfonyl)imide and others (Wang et al., 2012). The type of cation and anion manipulated the chemical and physical properties of ionic liquids. The large ions of ionic liquid electrolyte hindered the diffusion of ions into narrow pores of carbon-based materials. To date, each type of electrolyte is not perfectly established due to its own merits and demerits.

CHAPTER 3: METHODOLOGY

3.1 Introduction

Chapter 3 covers the explanation and discussion of four important sections. The first section provides information about the raw material selection, and type of chemicals that were used in this study. The second section elaborates on the experimental procedure and design of experimental setup that used to synthesis GO, rGO, P-GO, P-rGO, WO_3 and rGO/WO_3 nanocomposite. The third section emphasized on the application process with regards to preparation of electrode. These studies aim to determine the optimum processing parameters to obtain desired rGO/WO_3 composite for the best electrochemical performance by improving the electrical conductivity of WO_3 using conductive rGO. The last section in this chapter outlines the characterization of structural, morphological and electronic properties of the resulted samples using various techniques, such as XRD, Raman, BET, FESEM and HRTEM. While the electrochemical properties of the samples are investigated through CV, GCD and EIS test. This covers a brief explanation on the characterization equipment, operating principles and sample preparation.

3.2 Raw Materials and Chemicals Selection

The raw materials and chemicals including their roles and properties that used to fabricate electrode materials were shown in Table 3.1. The chemicals were used as received without further purification. Deionized water (18.2 MΩ) was used throughout this study.

Table 3.1: List of raw materials and chemicals used to fabricate electrode materials including their purity, molar mass, roles and manufacturer.

Raw materials/ chemicals	Purity (%)	Molar mass ($g\ mol^{-1}$)	Roles	Manufacturer
Graphite powder	99	12.0	Starting material of rGO	Sigma Aldrich (Steinheim, Germany)
Ammonium paratungstate (APT)	99.99	3132.2	WO_3 precursor	Sigma Aldrich (Steinheim, Germany)
Hydrazine	35 wt % in H_2O	32.1	Reducing agent for rGO synthesis	Sigma Aldrich (Steinheim, Germany)
Sulfuric acid (H_2SO_4)	95-97	98.1	Create acidic reaction condition	Merck (Darmstadt, Germany)
Potassium persulfate ($K_2S_2O_8$)	≥ 99	270.3	Oxidizing agent for pre-oxidized graphite	Merck (Darmstadt, Germany)
Phosphorus pentoxide (P_2O_5)	≥ 98	283.9	Oxidizing agent for pre-oxidized graphite	Merck (Darmstadt, Germany)
Potassium hydroxide (KOH)	≥ 85	56.1	Undergo fast deoxygenation and resulting in stable rGO suspension	Merck (Darmstadt, Germany)
Sodium sulfate (Na_2SO_4)	≥ 99	142.0	Electrolyte	Merck (Darmstadt, Germany)
Sodium sulfite (Na_2SO_3)	97-100	126.0	Electrolyte	Merck (Darmstadt, Germany)
Hydrogen peroxide (H_2O_2)	30	34.0	Terminate the reaction and remove residual permanganate and manganese dioxide	R&M Chemicals (Essex, UK)
Hydrochloric acid (HCl)	37	36.5	Remove manganese salts	R&M Chemicals (Essex, UK)
Potassium permanganate ($KMnO_4$)	99	158.0	Oxidizing agent for GO synthesis	Friendemann Schmidt Chemical (Woodpark, Australia)

3.3 Experimental Procedure

Hydrothermal is the most feasible technique due to its ability to create nanostructure materials. Moreover, hydrothermal is relatively simple and easy process. The followings are the stages involved in this study, started from synthesis of P-rGO and subsequently adding WO_3 into P-rGO to form nanocomposite for supercapacitor evaluation.

3.3.1 Synthesis of Graphene Oxide (GO)

In a typical procedure, the pristine graphite was directly added into a beaker containing 300 mL of H_2SO_4. $KMnO_4$ (35 g) was added gradually with stirring at 35 ˚C for 4 h in an ice bath thereafter. Then, the mixture was diluted with 1 L of deionized water while maintaining the temperature at 50 ˚C. In order to stop the reaction, deionized water was added followed by the addition of 100 mL of 30% H_2O_2. The color of the solutions immediately turned from dark brown to light brown, indicating the completion of oxidation. The solid product was washed with HCl to remove the metal ions followed by distilled water to remove the acid residue. Finally, the resulted GO was oven-dried at 80 ˚C overnight.

3.3.2 Synthesis of Pre-oxidized Graphene Oxide (P-GO)

Graphene oxide (GO) was synthesized by oxidizing graphite powder in the presence of $KMnO_4$ and concentrated sulfuric acid. According to Kovtyukhova et al. (1999), a pre-oxidized step was required before the oxidation step to synthesis the GO. Prior to pre-treatment, 4 g of graphite powder was added to a mixture of 30 mL of H_2SO_4, 6 g of $K_2S_2O_8$ and 6 g of P_2O_5. The mixture was mechanically stirred at 80 ˚C for 6 h thereafter. Then, the resulting mixture was allowed to cool down slowly to room temperature. Next, the solution was diluted with deionized water and kept overnight. Then, the solution was filtered, and the product was dried in vacuum desiccators. The pre-oxidized graphite

powder was re-oxidized using modified Hummers' method (Section 3.3.1) to form P-GO (Tang et al., 2009).

3.3.3 Synthesis of Reduced Graphene Oxide (rGO) and (P-rGO)

1 g of graphite oxide/pre-oxidized graphite oxide was dissolved in 500 mL of deionized water through ultrasonication for 30 min to form GO supernatant. After that, 5 M KOH solutions were added dropwise to the supernatant until the pH 10 before adding 0.25 mL of hydrazine. The above solution was poured into a round bottom flask and undergoes reflux reaction at 95 ˚C for 24 h as shown in Figure 3.1. The mixture was filtered and washed with deionized water to adjust the pH to neutral. A black precipitate was obtained and dried in oven for 24 h. The resulted rGO and P-rGO powder was used for further characterizations.

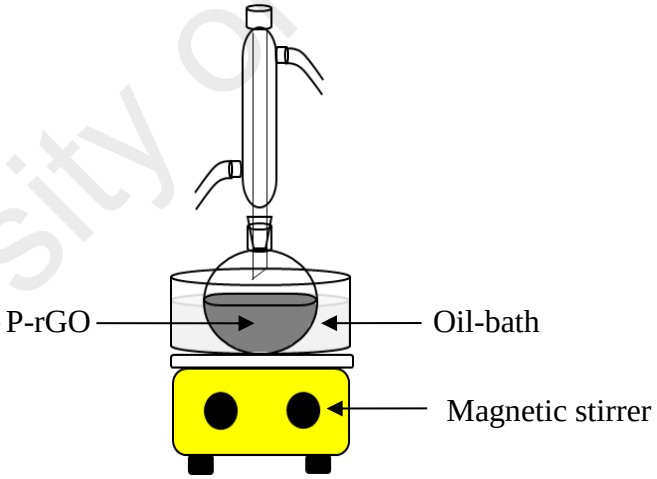

Figure 3.1: Experimental setup for synthesis of P-rGO using reflux technique.

3.3.4 Synthesis of P-rGO/WO_3 nanocomposites

The P-rGO/WO_3 nanocomposites were synthesized via a simple hydrothermal approach in this study. Accordingly, 3 mg of P-rGO powders were dispersed in 40 mL of deionized water and ultra-sonicated for 90 min to form a homogenous suspension. 0.3 g of APT was then added, with continuous stirring for 6 h. Then, HCl was added to adjust

the pH of the solution to 2. At this stage, the color of the solution changed from black to grey, indicating the APT powder was well-dispersed in P-rGO suspension. The as-prepared solution was then transferred to a Teflon-line stainless steel autoclave and held at 180 ˚C for 20 h (Figure 3.2). After cooling, the precipitate was filtered and washed thoroughly with deionized water and dried at 60 ˚C. By controlling the loadings of APT, hydrothermal temperature and reaction time, similar experimental conditions were carried out to synthesize desired P-rGO/WO_3 nanocomposites. Pure WO_3 was prepared by the similar procedure of preparing composites without P-rGO.

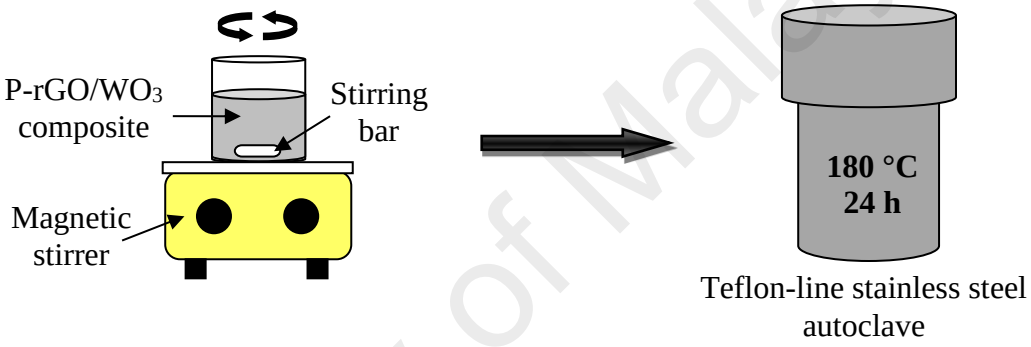

Figure 3.2: Experimental setup for synthesis of P-rGO/WO_3 nanocomposites.

In the present study, fabricated P-rGO/WO_3 nanocomposites through the hydrothermal technique by controlling the loadings of APT, hydrothermal temperature and reaction time were carried out. In addition, optimization of crystal structure during the heat treatment process for P-rGO/WO_3 nanocomposites is crucial in improving the electrochemical performance of electrode. To the best of our knowledge, reports on the effect of WO_3 on P-rGO sheets and theirs electrochemical performance still lacking. Therefore, the optimum synthesis parameters to obtain the desired P-rGO/WO_3 nanocomposites for the best electrochemical performance was aimed in our study. The constant and varied parameters for the WO_3 to incorporate on P-rGO surface have been showed in Table 3.2. An overview of the research methodology also illustrated in Figure 3.3.

Table 3.2: Parameters investigated to produce desired P-rGO/WO_3 nanocomposites and constant parameter.

Influence Parameter	Constant value
Loadings of P-rGO and APT in ratio form: P-rGO:APT (1:50, 1:100, 1:150, 1:200)	pH 2; Temperature = 180 ºC; Time = 20 h
Hydrothermal temperature: (120, 150, 180 ºC)	pH 2; Ratio of P-rGO:APT = 1:100; Time = 20 h
Reaction time: (5, 10, 15, 20 h)	pH 2; Ratio of P-rGO:APT = 1:100; Temperature = 150 ºC

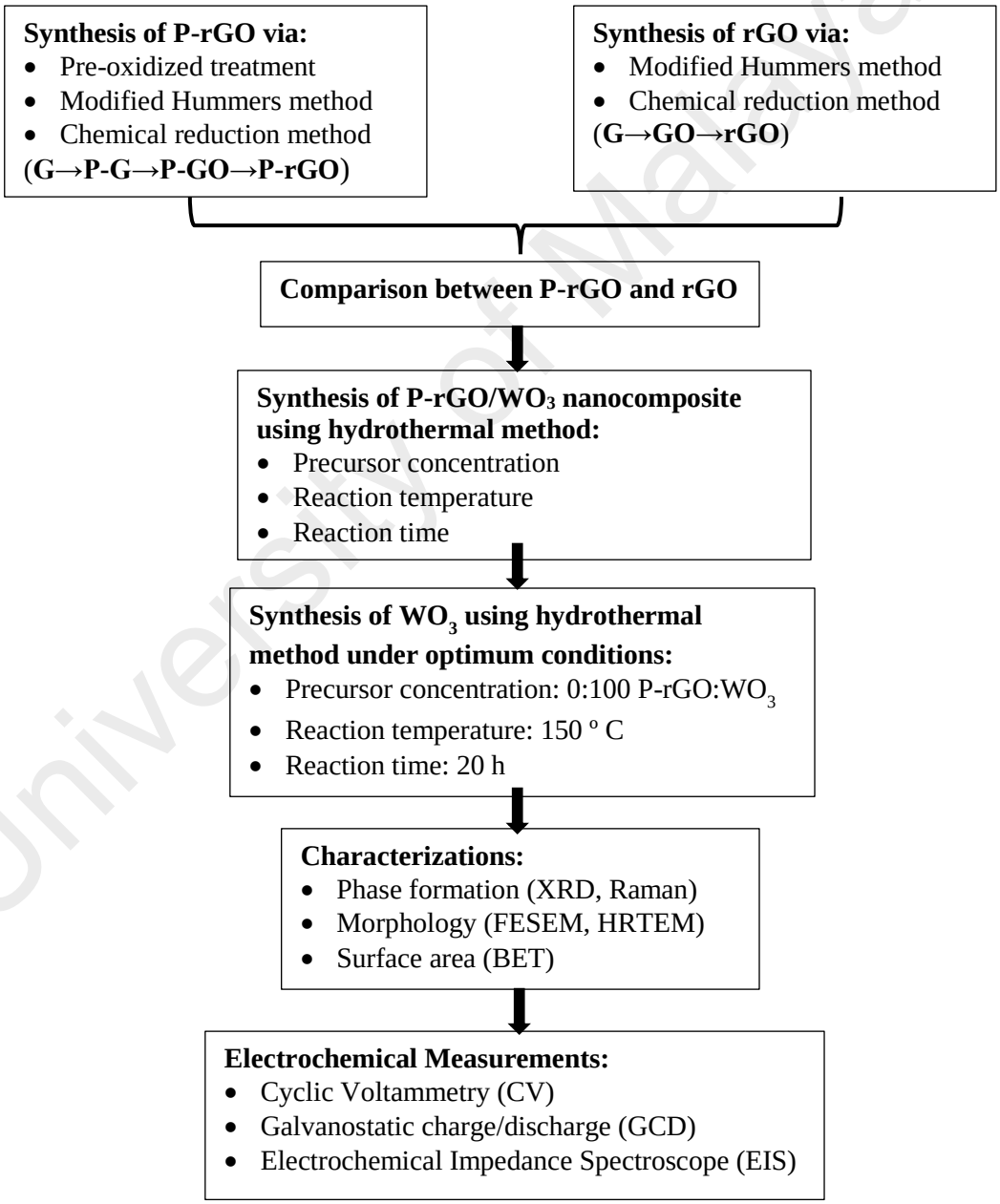

Figure 3.3: An overview of the research methodology.

3.4 Characterization Techniques

All the samples that were prepared in the experimental works were characterized accordingly. The structural, morphological, and electronic properties of GO, rGO, P-GO, P-rGO, WO_3 and rGO/WO_3 nanocomposite were characterized via various characterization techniques. The characterization techniques are X-Ray Diffraction (XRD), Raman Spectroscope, Field Emission Scanning Electron Microscope (FESEM), High Resolution Transmission Electron Microscope (HRTEM) and Surface area and porosity measurement (Brunauer-Emmett-Teller; BET). While, the electrochemical properties of samples are investigated using cyclic voltammetry (CV), galvanostatic charge/discharge (GCD) and electrochemical impedance spectroscope (EIS). In this section, information on the characterization technique, basic principle and sample preparation of such analytical equipment are discussed briefly.

3.4.1 X-ray Diffraction (XRD)

X-ray diffraction is a non-destructive technique, which gives the information about crystal structures and atomic spacing of material. In general, the monochromatic X-rays beam generated from cathode ray tube are directed toward the sample and the diffracted rays are collected by a detector to produce diffraction patterns. These patterns will be indexed to get the information of the phase for the materials.

In this study, the samples were analyzed using EMPYREAN, PANalytical powder X-ray diffractometer (Almelo, Netherlands). The fine powder was placed onto a sample holder and ensured a flat upper surface. Then, it was placed at the center of diffraction chamber and scanned over Cu Kα radiation (λ=1.5404 Å) with diffraction angle of 2θ in the range 5 to 90 º. The scan rate was 0.2 s^{-1} and the collection of results was after every 0.02 º. The interlayer spacing (d) of sample is calculated using Bragg's Law:

$$n\lambda = 2d \sin\theta \qquad \text{(Equation 3.1)}$$

where λ is the wavelength of X-ray beam, θ is the angle of diffraction and n is the positive integer.

3.4.2 Raman Spectroscopy

Raman spectroscopy was employed to study the chemical interaction and purity of the samples. Raman spectra were obtained using Renishaw inVia (Gloucestershire, UK) and operating with an Ar^+ laser at 514 nm as the excitation source. The sample was smeared uniformly onto a glass slide to create a flat upper surface prior to analysis. The laser light interacts with the sample leading to the laser photons shifts, which gives the information about the vibrations and phonons modes in the sample molecules.

3.4.3 Surface Area and Porosity Measurement

Gas adsorption is a physisorption technique used to characterize the surface area and texture of porous sample by directly measured the gas uptake, such as gravimetric measurement of the change in mass of sample (adsorbent) to form adsorption-desorption isotherms. Such isotherm displayed in graphical form, showing the amount adsorbed vs. equilibrium relative pressure (P/P_0). This isotherm will be indexed to get the information about the pores size (i.e., micro-, meso- and macro-) and pores volume of sample. Prior to determination of adsorption isotherm, outgassing the sample under vacuum is required to remove the physisorbed species from the surface of sample.

In this study, pore structure and Brunauer-Emmett-Teller (BET) surface area of sample was analyzed by nitrogen adsorption-desorption isotherms method with a Micromeritics ASAP 2020 instrument (Georgia, USA). Prior to the measurements, the isotherms were evaluated at -196 ºC after the samples were degassed at 150 ºC for 24 h under vacuum. The sample was filled into glass cell and attached to sample preparation station.

3.4.4 Field Emission Scanning Electron Microscope (FESEM)

FESEM is a well-established tool for characterization of the surface structure of sample. It relies on the electrons beam that generated from field emission gun and pass through electromagnetic lenses to produce a thin beam of electrons. This incident electron beam interacts with the atoms of sample and generates a multitude of signal types, namely back-scattered electrons (BSE), secondary electrons (SE), auger electrons and characteristic X-rays. BSE and SE are commonly used: (i) BSE: showing contrasts in composition in multiphase specimen (brightness depends on atomic number); (ii) SE: showing morphology and surface structure of sample. While measure the energy of X-rays can determine the elements that present in sample.

In this study, morphologies were captured by field-emission scanning electron microscope (FESEM, JEOL JSM-7600F) (Massachusetts, USA) and energy dispersive X-ray spectroscopy (EDX, JEOL JSM-7600F) was applied to determine the composition of the samples. Before doing characterization, the sample was scattered with spatula and press lightly to attach it on carbon tape. Usually, it was spraying with air to remove loose sample from the top. This step helps to avoid sample fly off from the holder in the vacuum.

3.4.5 High Resolution Transmission Electron Microscope (HRTEM)

Microstructures and morphologies were observed using transmission electron microscope (TEM, JEOL JEMP-2100F) (Massachusetts, USA). The basic principle of HRTEM is based on highly energetic electrons beams that transmitted through a thin specimen which will get scattered. The scattered electrons are then passed through the electromagnetic lens for refocusing the electrons and projecting it in image form on the screen. The prepared sample must be totally dried before imaged in the microscope. For sample preparation, first, the powder form sample was dispersed in absolute ethanol.

Then, a drop of sample was placed on carbon coated copper grids and allowed the alcohol to evaporate in desiccator overnight before TEM analysis. A layer of carbon coated on grids is useful for stabilized the film when it exposed to electron beam.

3.5 Electrochemical Measurements

3.5.1 Preparation of Electrodes

A two electrodes system was used to evaluate the electrochemical properties of GO, rGO, P-GO, P-rGO, WO_3 and P-rGO/WO_3 nanocomposites in 1 M Na_2SO_3 neutral aqueous electrolyte. Nickel foams were used as current collector and cellulose membrane was used as the separator. Typically, working and reference electrode were prepared by mixing active materials (e.g. GO, rGO, P-GO, P-rGO, WO_3 or P-rGO/WO_3 nanocomposites), acetylene black and polytetrafluoroethylene (PTFE) with a ratio of 80:15:5 to create a slurry and pasted on nickel foams within an area of 1 × 1 cm^2 as presented in Figure 3.4. For comparison, the electrochemical performance of P-rGO/WO_3 composites were evaluated in two electrolytes, namely 1 M Na_2SO_4 and 1 M Na_2SO_3.

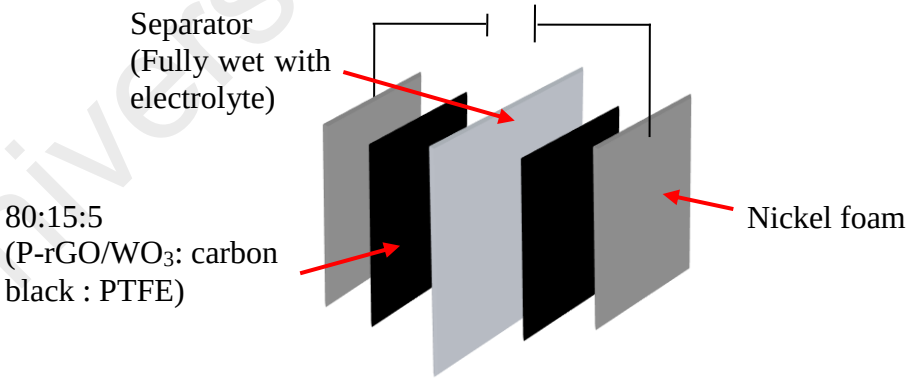

Figure 3.4: Schematic diagram of P-rGO/WO_3 nanocomposite electrode for supercapacitor performance.

3.5.2 Cyclic Voltammetry (CV)

Cyclic voltammetry (CV) is the technique used to examine the presence of redox reaction of the electroactive species and its reversibility under a range of potential. The potential of the system is fixed and the response of current flow is measured. Typical cyclic voltammogram shows that the current begins to flow as potential is swept from lower value and reaches a peak before dropping, suggesting surface reaction occurs in which reactant (M^{x+}) at electrode surface is converted to product ($M^{(x-1)+}$). When the potential reaches upper limit, the scan is reversed back to lower limit and converting the product back to reactant ($M^{(x-1)+} \rightarrow M^{x+}$). In this study, CV were carried out in potential range from -0.8 to 0.8 V at scan rate of 10, 25, 50 and 100 mV s^{-1} using Autolab PGSTAT 204 (Utrecht, Netherlands).

3.5.3 Galvanostatic Charge/discharge (GCD)

In this study, galvanostatic charge-discharge (GCD) were measured via Autolab PGSTAT 204 (Utrecht, Netherlands). It is a standard technique used to study the electrochemical properties (i.e., specific capacitance) and cycle life of supercapacitor. In this technique, the response of potential is measured by applying constant current. The electrode potential varies with time as it depends on the concentration ratio of reactant at electrode surface. The charge/discharge process was cycled in potential range from -0.8 to 0.8 V at current density of 0.3, 0.5, 0.7 and 1 A g^{-1}. Supercapacitor capacitance is determined from the slope of galvanostatic discharge curve using the following equation:

$$C = I/(dV/dt) \qquad \text{(Equation 3.2)}$$

where I is the current that applied to cell and dV/dt is the slope of discharge curve. Specific capacitances (C_{sp}) for single electrode are given below:

$$C_{sp} = (4*C)/m \quad \text{(Equation 3.3)}$$

where C is the capacitance and m is the total mass of active material in electrodes.

Energy density (E) and power density (P) of supercapacitor are calculated based on charge/discharge curves using Equations 3.4 and 3.5, respectively:

$$E = ½ [(C/m)^{*}V^2]/3.6 \quad \text{(Equation 3.4)}$$

$$P = E*3600/t \quad \text{(Equation 3.5)}$$

where C is the capacitance, m is the total mass of active material, V is the potential window and t is the discharge time.

3.5.4 Electrochemical Impedance Spectroscopy (EIS)

Electrochemical impedance spectroscopy (EIS) is a technique to measure the impedance data by applying a small amplitude of alternative interrupting potential over a wide range of frequency. It was performed in frequency range of 100 mHz to 100 kHz at open circuit potential with a potential amplitude of 10 mV by Autolab PGSTAT 204 (Utrecht, Netherlands). The collected electrochemical impedance data showing a semicircle at the medium frequency region of Nyquist plot and the arc is fitted to an equivalent circuit to measure the diameter of semicircle, which represented charge transfer resistance.

CHAPTER 4: RESULTS AND DISCUSSIONS

4.1 Introduction

This chapter presents the results obtained from the experiments conducted and the discussion of the analyses. There are four main sections in this chapter. The first section presents the information regarding to the formation of P-rGO and rGO. The influence of pre-oxidized treatment on resultant GO are evaluated in detail. The second section of this chapter will illustrate the P-rGO/WO_3 nanocomposite performance and the possible formation mechanisms of fiber-like WO_3 in P-rGO/WO_3 nanocomposite. The supercapacitor performances of the resultant nanocomposite in term of capacitance and cycling performance are presented. Based on our investigations, P-rGO/WO_3 sample via hydrothermal synthesis showed better supercapacitor performance than that of pure WO_3. The reason might be due to the addition of conductive P-rGO and synergistic effects of P-rGO and WO_3. In the current work, a comprehensive study was conducted to optimize several synthesis parameters (i.e., loading of APT, hydrothermal temperature and reaction time) to obtain the P-rGO/WO_3 composite that exhibits best supercapacitor properties. The last section will demonstrates the electrochemical performance of P-rGO/WO_3 composite in different neutral sodium-based electrolyte (i.e., Na_2SO_3 and Na_2SO_4) and determine the most suitable electrolyte.

4.2 Synthesis of P-rGO and rGO

A set of experiment was conducted for the formation of P-rGO and rGO with high specific surface area, high conductivity and high mechanical strength. It's a well-known fact that graphite occurs in the form of crystalline carbon, which made up of single sheets of stacked graphene held together by weak van der Waals force (Phiri et al., 2017). These graphene sheets can be obtained through chemical reduction of graphene oxide (GO) using hydrazine as reducing agent. rGO exhibited high electrical conductivity whereas GO is less conductive. The reason mainly attributed to the disturbance of the oxygen

functional groups that attached on GO surface. Thus, it is important to understand how the oxygen functional groups affect the electrochemical performance.

In order to obtain the degree of oxidation of graphite information during the changes in interlayer spacing of carbon lattice, XRD patterns were plotted. The Figure 4.1 (a) shows the XRD patterns of pristine graphite, pre-oxidized graphite (P-G), pre-treated graphene oxide (P-GO) and pre-treated reduced graphene oxide (P-rGO), respectively. Such plot is important to explain the mechanism of rGO formation. Based on the results obtained, it was found that pristine graphite exhibited a sharp and intense diffraction peak at $2\theta = 26.6^{o}$ which corresponds to (002) plane. After the pre-oxidized of graphite, a small change in the *d*-spacing from 0.33 to 0.39 nm is observed and calculated using Equation 3.1. This may attributed to small amounts of oxygen functional groups is attached on the graphene sheet. With further oxidized the P-G using modified Hummers' methods, P-GO shows a strong diffraction peak at 10.6º corresponds to the *d*-spacing of 0.83 nm along the (001) orientation, which significantly larger than the *d*-spacing of P-G (d = 0.39 nm) (Zainy et al., 2012). Consequently, the (002) peak of P-G at $2\theta = 26.2^{o}$ shifted to 10.6º, suggesting the attachment of oxygen functional groups (i.e., hydroxyl, epoxy, carbonyl and carboxyl) enlarged the interlayer spacing between carbon basal planes (Cao and Zhang, 2015). After chemical reduction, the peak at 10.6º disappeared and an intense P-rGO peak (002) positioned at $2\theta = 24.5^{o}$ with *d*-spacing of 0.36 nm was detected, indicating most of the oxygen functional groups are removed causing a decrease in interlayer spacing (Park et al., 2011). The broad peak of P-rGO reflects to its structure defects and low crystallinity index (Wang et al., 2011). Figure 4.1 (b) shows the XRD patterns of graphite, GO and rGO. It clearly shows that without the pre-oxidization stage, the peak due to graphite is still observed in GO, indicating the GO are not fully oxidized under same experimental conditions. The diffraction peak of rGO located at $2\theta = 24.1^{o}$ is very close to the diffraction peak of graphite, implying the successful reduction of rGO.

As well known, graphite is formed by stacking few layers of graphene sheets together through van der Waals force.

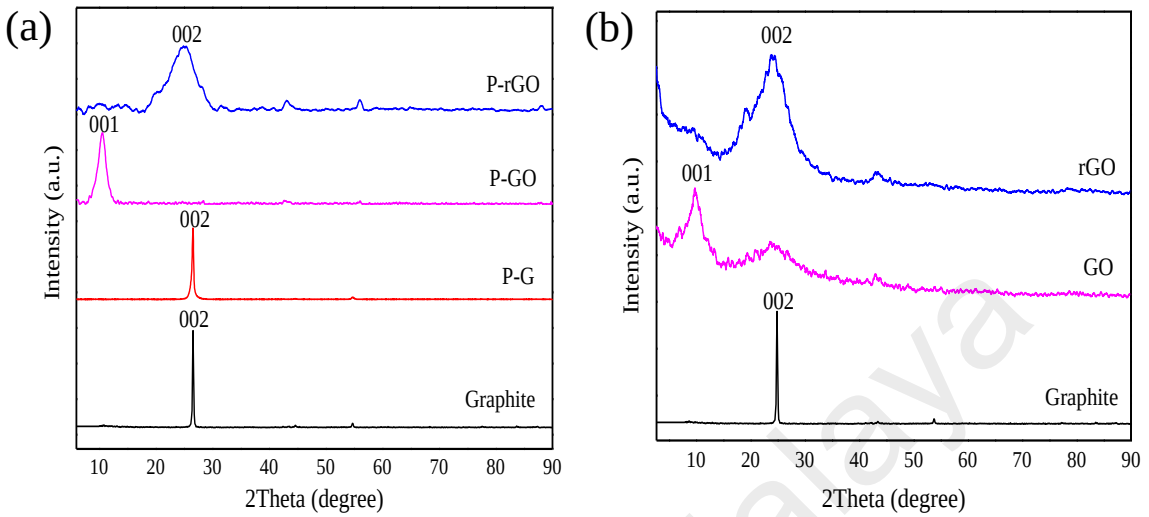

Figure 4.1: XRD patterns of (a) graphite, P-G, P-GO and P-rGO and (b) graphite, GO, rGO

The reduced state of P-GO to P-rGO and GO to rGO were further confirmed by Raman spectroscopy. In Figure 4.2 (a), the Raman spectrum of P-rGO contain two prominent peaks, namely D band and G band, appeared at 1350 and 1596 cm^{-1}, respectively. It is also apparent from the spectrum that the D and G bands of P-GO appeared at 1355 and 1603 cm^{-1}, respectively. In contrast, the D band and G band of rGO centered at 1352 and 1600 cm^{-1}, respectively as shown in Figure 4.2 (b). These characteristic peaks represent the defects in carbon atoms and the scattering of E_{2g} phonon of sp^2 carbon atoms (Bak et al., 2011). The intensity ratio of D and G bands (I_D/I_G) is used to measure the degree of disorder and average size of sp^2 domains in graphene materials (Kim et al., 2013). The I_D/I_G of P-GO and P-rGO are 0.74 and 0.84, respectively. While the I_D/I_G of GO and rGO are 0.85 and 0.88, respectively. P-rGO and rGO has the highest I_D/I_G ratio compared to that of P-GO and GO, due to a disorder after the oxygen groups are removed and introduced large amounts of sp^2 carbon networks with small average sizes (Chen et al., 2011). However, the I_D/I_G ratio of P-rGO is slightly lower than rGO, suggesting that the

P-rGO has larger sp^2 domains size than that of rGO. This large sp^2 domain structures result in an increased of conductivity and thus benefits the diffusion of ions (Stankovich et al., 2007). The 2D band is the key features to verify the number layers of graphene sheets in Raman Spectroscopy. In 2015, Akhavan reported that the 2D band of single-layer graphene typically positioned at around 2679 cm^{-1} while the 2D band of multi-layer graphene are blue shift into higher wavenumbers, which is 2698 cm^{-1} (Akhavan, 2015). In this study, the 2D band of P-rGO was located at 2689 cm^{-1}, while the 2D band of rGO was positioned at 2680 cm^{-1}, confirming that few-layer graphene sheets are observed for P-rGO and rGO.

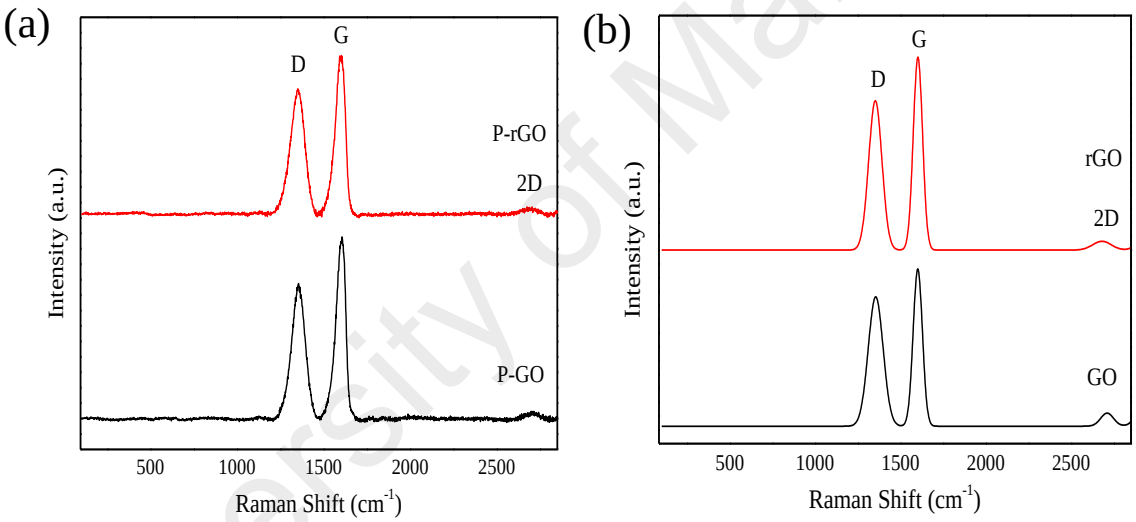

Figure 4.2: Raman spectrum of (a) P-GO and P-rGO and (b) GO and rGO.

Figure 4.3 shows the FESEM image of the morphological of (a) P-rGO and (b) rGO. As shown in Figure 4.3 (a), exfoliated P-rGO sheets appeared as crumpled morphology with densely stacked structure after chemical reduction. Many cracks can be obtained at the edge of P-rGO and provide void spaces between layers, which could contributed to fast charging rate (Perera et al., 2012). Figure 4.3 (b) reveals that the rGO showed thick particles that have not been fully exfoliated and thus low capacitance is expected. This results suggest that the oxidation degree of GO could influence the reduction process.

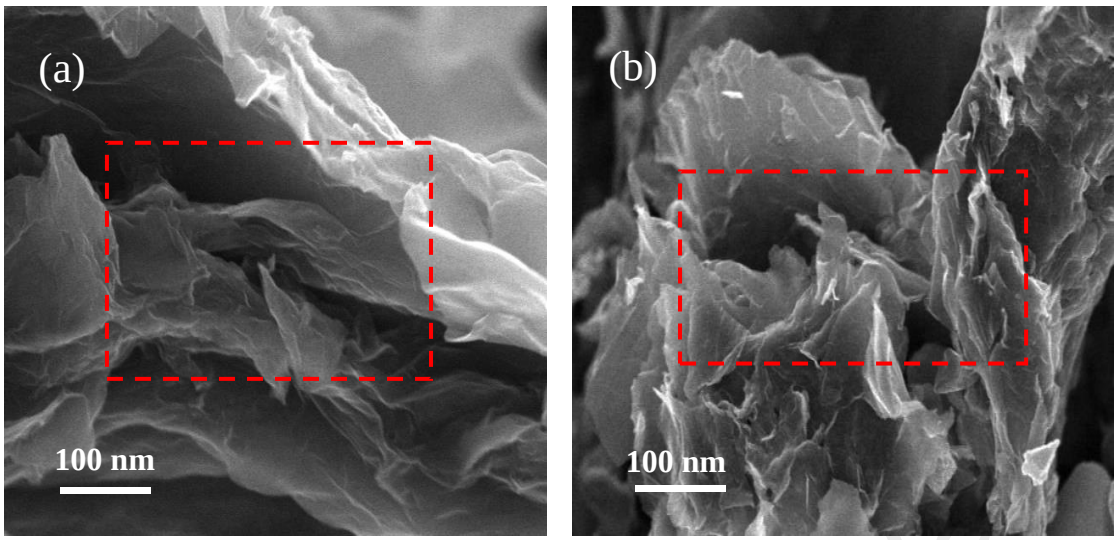

Figure 4.3: FESEM image of (a) P-rGO and (b) rGO.

Preliminary investigation on the electrochemical performance of P-GO, P-rGO, GO and rGO were carried out to study the potential of these materials to be used in the synthesis of composite. As presented in Figure 4.4 (a), rectangular like shape of CV curve was observed for P-rGO and rGO, while the CV curve of P-GO and GO electrode was deviating from rectangular shape. This deviation probably due to the presence of oxygen containing functional group on GO surface, which increased the resistance of ion penetration through electrode (Suleman et al., 2015). Moreover, a pair of weak redox peaks was observed in the CV curve of P-GO, showing the oxygen functional groups present on P-GO surface involves Faradaic reactions in electrochemical activity (Satheesh and Jayavel, 2013). However, it still shows a low current density with lower integral area as compared to P-rGO.

Figure 4.4 (b) displays the galvanostatic charge/discharge curves of P-GO, P-rGO, GO and rGO measured at current density of 0.7 A g^{-1}. Using Equations 3.2 and 3.3, the calculated specific capacitance increases in the following order: GO (31.7 F g^{-1}) < rGO (43.8 F g^{-1}) < P-GO (84.6 F g^{-1}) < P-rGO (138.7 F g^{-1}), indicating P-rGO exhibited the highest specific capacitance. The restoration of sp^2 hybridization increases the electrical conductivity of P-rGO and enhanced the ion mobility from electrolyte to electrode

(Sadhukhan et al., 2016). The large value of specific capacitance for P-GO further proved that the involving of Faradaic reactions – pseudocapacitance.

Based on aforementioned discussion, equivalent series resistance (ESR) is inverse proportional to the capacitive behavior. Hence, electrochemical impedance spectroscopy (EIS) measurement was conducted to study the electrical conductivity of electrode. Nyquist plot shows that ESR is obtained from the intercept at the real axis (Z') of Nyquist plot in high frequency region, semicircle in medium frequency region and straight line in low frequency region is related to diffusive resistance or Warburg impedance (Sankar and Selvan, 2014). ESR composed a series of resistance including electrolyte resistance, internal resistance of the substrate and contact resistance between current collector and material (Gholipour-Ranjbar et al., 2016). The inset in Figure 4.4 (c) demonstrated that the ESR values of P-GO, P-rGO, GO and rGO are 0.91, 0.77, 1.08 and 1.22 Ω, respectively. Changing in ESR value can be accredited to the different conductance value of P-GO, P-rGO, GO and rGO (Yang et al., 2017). Typically, the lower the ESR value is, the higher the conductivity of an electrode material will be. Moreover, P-rGO electrode also exhibited the smallest diameter of semicircle in comparison with P-GO, GO and rGO, indicating P-rGO possesses lower charge transfer resistance (R_{ct}) as shown in inset of Figure 4.4 (c) (Jo et al., 2016). According to fitted results, the R_{ct} value decreases according to the following order: GO (9.59 Ω) > rGO (5.24 Ω) > P-GO (3.17 Ω) > P-rGO (2.05 Ω). As shown in Figure 4.4 (c), all electrodes appear to have a vertical straight line nearly parallel to imaginary (Z") axis at low frequency, resulting in low ion diffusion resistance in the electrode. However, the curve of GO was slight bend, suggesting high ion diffusion resistance within electrode.

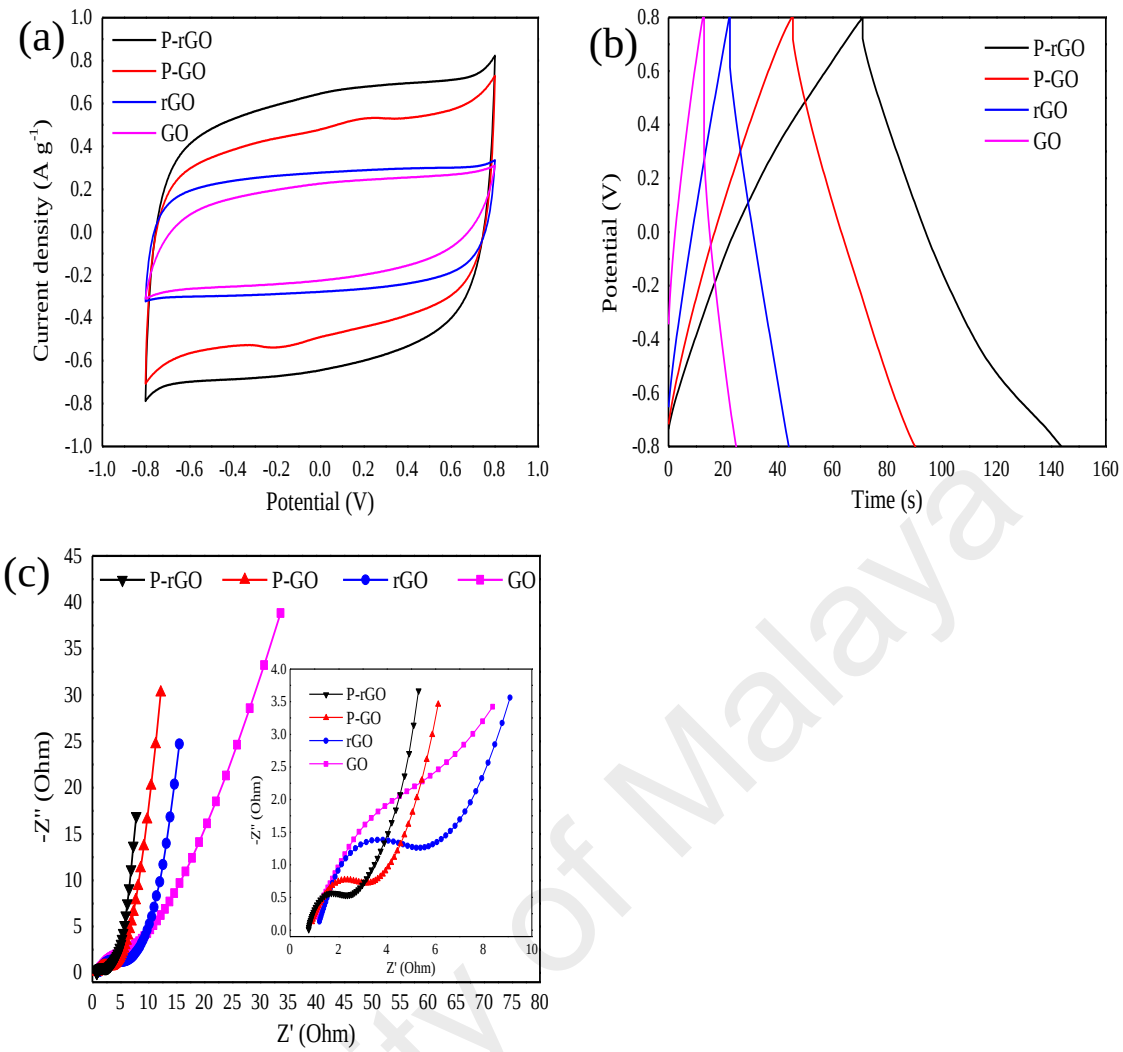

Figure 4.4: Electrochemical performance of P-GO, P-rGO, GO and rGO. (a) Cyclic voltammogram measured at scan rate of 25 mV s^{-1}; (b) Galvanostatic charge/discharge curves measured at current density of 0.7 A g^{-1}; and (c) Nyquist plot of P-GO, P-rGO, GO and rGO. The inset shows the enlarged high frequency region.

4.3 Synthesis of P-rGO/WO_3 Nanocomposites

Based on aforementioned discussion, P-rGO electrode was successfully synthesized via two-steps modified Hummers' method followed by chemical reduction technique and exhibited the best EDLC performance. A maximum specific capacitance of 138.7 F g^{-1} at current density of 0.7 A g^{-1} was achieved. Therefore, in the following studies, P-rGO electrode were synthesized in such condition mentioned above to study the effect of WO_3 loaded P-rGO electrode studies. The aim of this section is to improve the electrochemical performance of supercapacitor in term of specific capacitance and cycling performance.

In the present study, P-rGO/WO_3 nanocomposites were fabricated using hydrothermal technique. To the best of our knowledge, reports on the effect of deposit WO_3 on rGO and its electrochemical performance is still lacking. Therefore, the first part of the present study aims to determine the optimum synthesis parameters in order to achieve the desired P-rGO/WO_3 nanocomposites electrode for the high electrochemical performance. The second part of the current study propose possible formation and growth mechanisms of fiber-like WO_3 in P-rGO/WO_3 nanocomposites.

4.3.1 The Influence of Loading of APT using Hydrothermal Technique

It is well known that mass loading of WO_3 precursors plays an important role in determining the transportation of charge carrier in P-rGO/WO_3 nanocomposites. Considering this fact, optimization of the loading content of WO_3 during the hydrothermal synthesis of P-rGO/WO_3 nanocomposites to enhance their electrochemical performance is crucial. Correspondingly, it has been reported in literatures that P-rGO obtained from P-GO during the reduction process possesses excellent properties, such as high specific surface areas, structural flexibility, high electrical conductivity and good mechanical properties (Phiri et al., 2017; Zhu et al., 2010). However, in P-rGO, an atomic thick layer of carbon atoms arranged in a honeycomb lattice tended to suffer from irreversible graphene sheet-to-sheet restacking which limited the electrolytes diffusion (González et al., 2016). To overcome these limitations, it is common to incorporate WO_3 precursors into P-rGO to suppress the restacking of graphene and prevent agglomeration. In the present research study, the influence of mass loading of the WO_3 precursors on the formation of P-rGO/WO_3 nanocomposites as well as their electrochemical performance was investigated in detail.

In the present study, XRD analysis was used to study the effect of crystal structure of P-rGO/WO_3 nanocomposites containing different APT loadings. Figure 4.5 (a) shows the XRD patterns of the synthesized sample with different P-rGO to APT weight ratio. Accordingly, the Bragg diffraction of h-WO_3 phase was detected at 2θ values of 13.9, 23.3, 24.1, 27.1, 28.1, 33.7, and 36.7º in entire XRD patterns, corresponding to (100), (002), (110), (102), (200), (112) and (202) crystal planes, respectively. All the XRD diffraction peaks could be indexed to the hexagonal phase of WO_3 (h-WO_3, Joint Committee on Powder Diffraction Standards (JCPDS) with the card number of 85-2460) (Xu et al., 2015). However, there was no obvious (002) P-rGO diffraction peak at 2θ=24.5º being observed in the XRD patterns. This implies the insufficient sensitivity of the XRD measurements in detecting small amounts of P-rGO within the composite (< 2%) (Huang et al., 2013a). On top of that, no other impurity peaks were detected by the XRD analysis. This gives us a hint that the hydrothermal method assisted by HCl could produce pristine hexagonal phase of WO_3.

Figure 4.5 (b) shows the Raman spectra of P-rGO/WO_3 nanocomposites containing different loadings of APT. Correspondingly, the Raman band peaks at the lower wavenumber region corresponded to WO_3, while and those appeared at the high wavenumber region assigned to P-rGO. It is interestingly to note that the Raman spectra of the P-rGO/WO_3 nanocomposites containing higher amount of APT was significantly more intense. Raman peaks in the composition range of 250-261, 308-337, 681-705, 772-800 and 916-958 cm^{-1} were found to be the fundamental modes of the crystalline hexagonal phase (h-WO_3). The presence of sharp peaks at 681-705 and 772-800 cm^{-1} implied the elastic and flexural vibrations of O-W^{6+}-O stretching mode, respectively (Gu et al., 2016). The weak and broad peak at 250-261 cm^{-1} was attributed to the bending mode of W^{4+}-O bond; the peak at 308-337 cm^{-1} was ascribed to the bending mode of W^{5+}-O bond (Huo et al., 2013); while the peak at 916-958 cm^{-1} was mainly associated

with the stretching mode of W^{6+}=O bond (Ou et al., 2012). It was also noticed that the Raman peaks of WO_3 became broadened with increasing the APT concentration. This is presumably due to the formation of W-O-C bonds and the weakening of the initial W=O bonds. These are in agreement with Guo et al. (2012) and Jie et al. (2015). Moreover, two characteristic P-rGO peaks for D band at 1338-1353 cm^{-1} and G band at 1595-1599 cm^{-1} were also observed. Accordingly, the presence of D band attributed to the presence of defects and disorder carbon in the graphene sheets, while the G band corresponded to the scattering of E_{2g} mode of sp^2 carbon atoms (Kalambate et al., 2015).

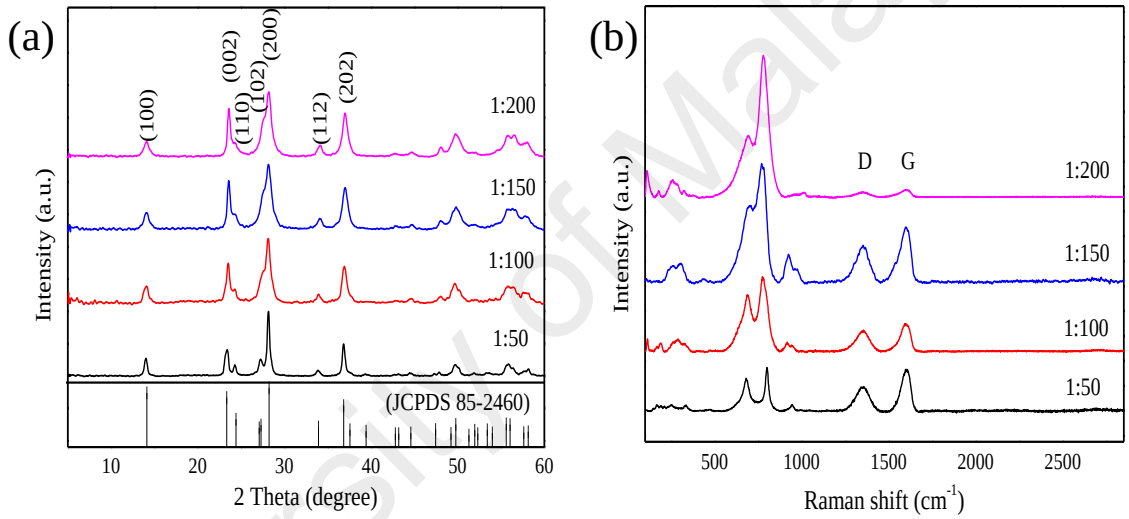

Figure 4.5: (a) XRD patterns and (b) Raman spectra of P-rGO/WO_3 nanocomposites prepared at different loading amount of APT.

Figure 4.6 (a-d) shows the FESEM images of the synthesized P-rGO/WO_3 nanocomposites containing different amounts of APT loaded. It is clear that the morphologies of the P-rGO/WO_3 nanocomposites were highly dependent on the loading amount of APT. The morphologies of samples synthesized using lower amount of APT (in range of 50-100) were found to be identical, in which the fiber-like structure randomly distributed throughout the P-rGO sheets. The diameter of the nanofibers was calculated based on the nanofiber diameter distribution histogram (Figure 4.7) and their respective values were tabulated at Table 4.1.

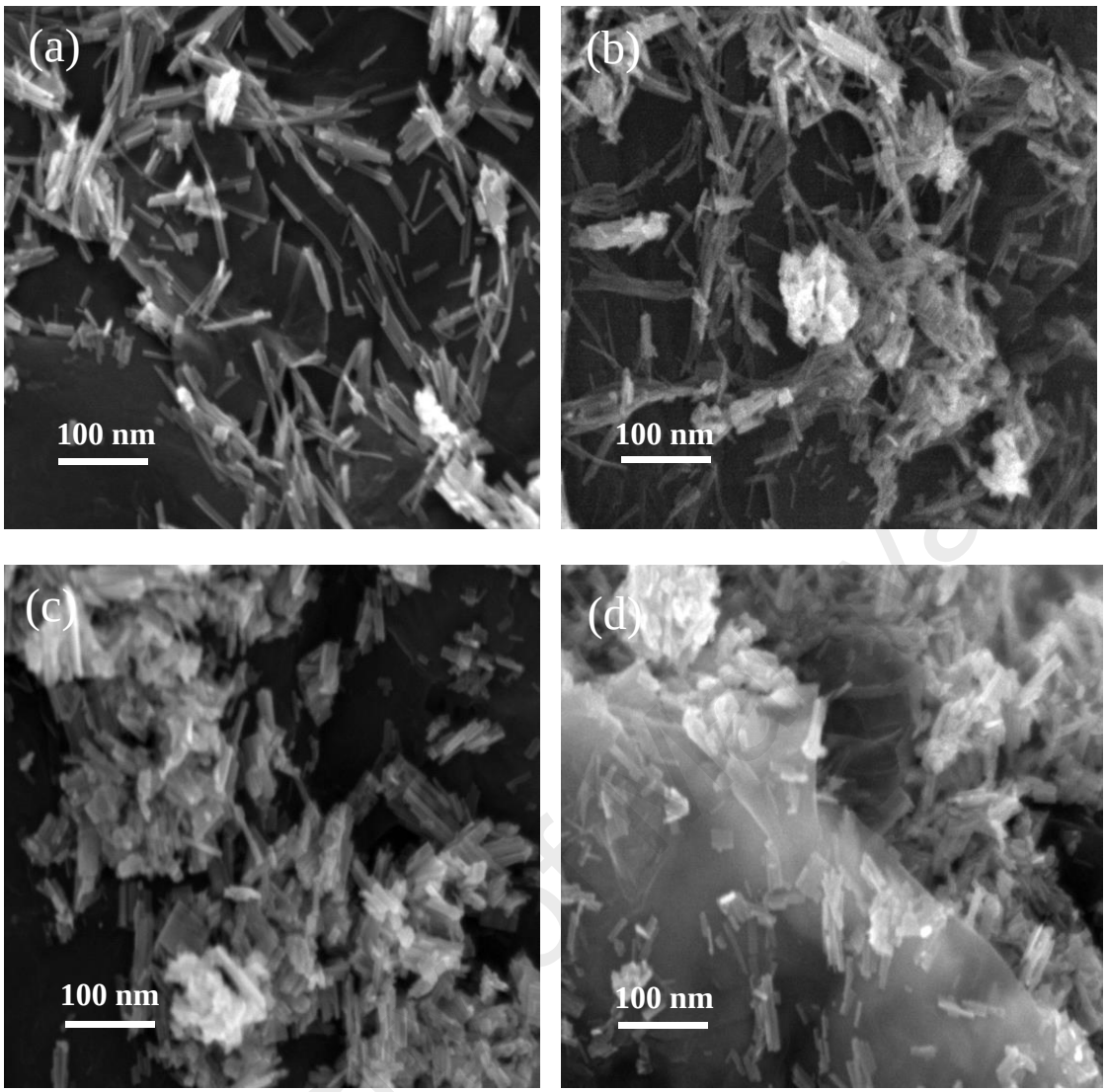

Figure 4.6: FESEM images of P-rGO/WO_3 nanocomposites prepared at different loading amount of APT (P-rGO:APT) (a) 1:50, (b) 1:100, (c) 1:150 and (d) 1:200.

Table 4.1 showed that nanofibers of about 16 nm or less in diameter could be successfully prepared through a hydrothermal process. It is noteworthy that the small diameter of fiber-like structure WO_3 in P-rGO/WO_3 nanocomposites make them attractive materials for use in electrochemical capacitors considering small fiber diameter shortened the diffusion length for electrolyte access (Wang et al., 2014b). As the loading amount of APT was further increased to 150, nanofibers tended to agglomerate and the surface of the composite nanofibers became rough and irregular (Figure 4.6 (c)). The diameter of the nanofiber was discovered dramatically increased to an average of about 22 nm and these nanofibers stacked and adhered together in various orientations with

respect to the long axis of the fiber. By increasing the amount of APT loaded (1:200), the surface morphology of the resulting nanocomposite was completely different compared to that in Figure 4.6 (a-c), where larger fiber-like crystals were formed because of the building-up of WO_3 agglomerates.

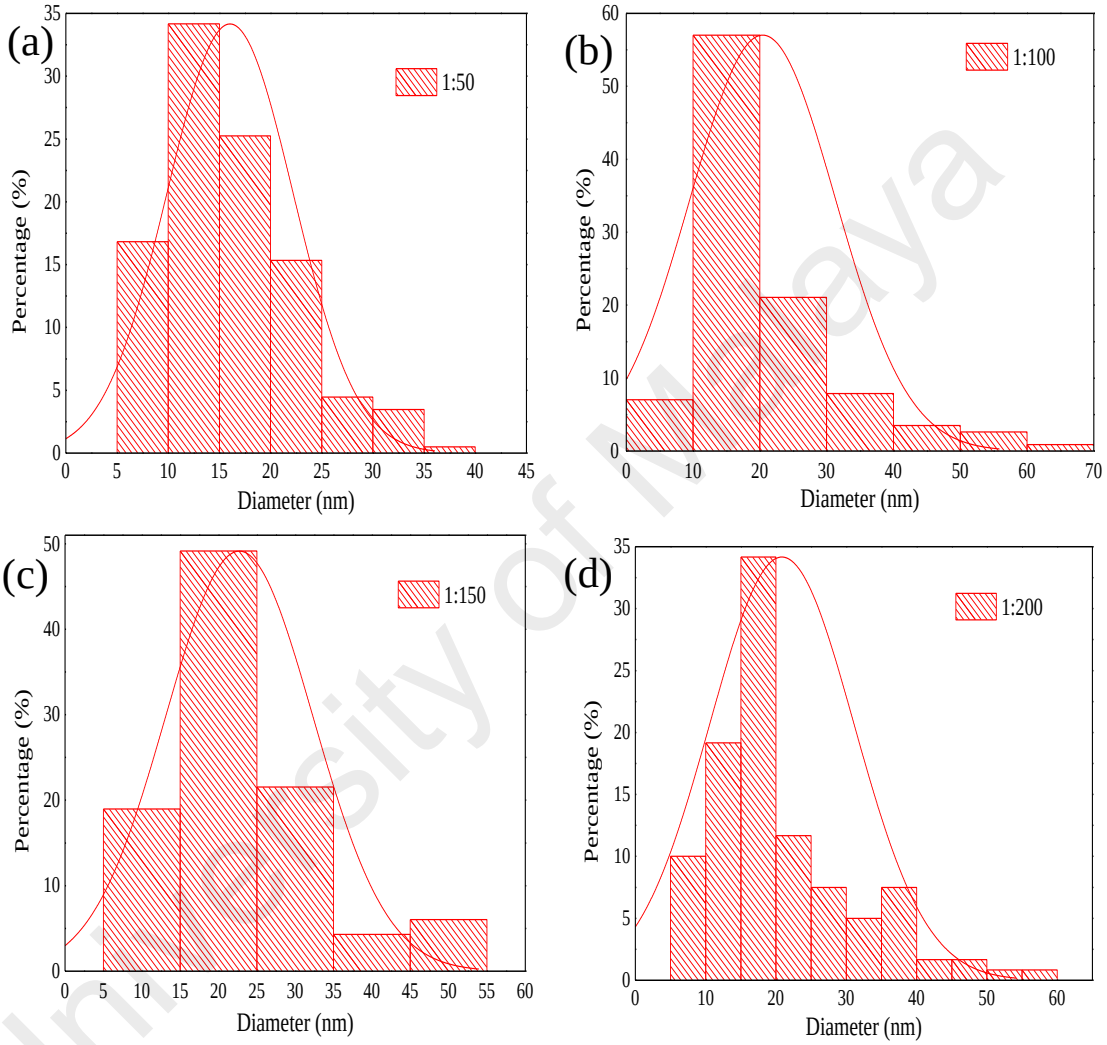

Figure 4.7: Diameter of P-rGO/WO_3 nanocomposites prepared at different loading amount of APT (P-rGO:APT) (a) 1:50, (b) 1:100, (c) 1:150 and (d) 1:200.

Table 4.1: Diameter of P-rGO/WO_3 nanocomposites prepared at different loading amount of APT (P-rGO:APT).

Samples	Diameter (nm)
1:50	16.04
1:100	20.43
1:150	22.72
1:200	20.84

Table 4.2 shows the elemental composition of the synthesized P-rGO/WO_3 nanocomposites containing different loading amounts of APT. Correspondingly, the EDX results revealed the W content of P-rGO/WO_3 nanocomposites appear to increase with increasing loading amount of APT from 1:50 to 1:200 of P-rGO:APT. The average W content dramatically increased approximately 3.02 at% as the loading amount of APT was further increased from 50 and 100. These findings gave us a hint that the WO_3 anchored on P-rGO became more prominent by increasing the APT loading amount.

Table 4.2: EDX results of P-rGO/WO_3 nanocomposites prepared at different loading amount of APT.

Ratio of P-rGO:APT	Elements		
	Tungsten, W (at%)	Oxygen, O (at%)	Carbon, C (at%)
1:50	4.52	15.46	80.02
1:100	7.54	21.90	70.56
1:150	10.70	36.52	52.78
1:200	14.74	41.06	44.20

Brunauer-Emmett-Teller (BET) specific surface area and pore size characteristic of P-rGO/WO_3 nanocomposites were investigated through isothermal nitrogen adsorption/desorption. Figure 4.8 (a-d) displays N_2 sorption isotherms of P-rGO/WO_3 nanocomposites with 1:50, 1:100, 1:150 and 1:200 of P-rGO:APT. All the synthesized samples exhibit similar Type V adsorption isotherms according to the IUPAC classification. A small number of N_2 was absorbed at low relative pressure ($P/P_0 < 0.1$), revealing the formation of micropores is in low quantities. At high relative pressure ($0.7 < P/P_0 < 1.0$), an obvious H1 hysteresis loop is obtained, suggesting the presence of mesoporous and some macroporous structure in the sample simultaneously (Pang et al., 2016). The BET surface area, pore volume and pore size of 1:50-, 1:100-, 1:150- and 1:200- P-rGO/WO_3 nanocomposites are listed in Table 4.3. The obtained results show that the specific surface area rises from 69.36 to 77.64 $m^2 g^{-1}$ with increasing

the loaded amount of APT from 50 up to 100 and thereafter decreases with further increase in amount of APT to 150 (65.36 m^2 g^{-1}) and 200 (37.57 m^2 g^{-1}). The higher amount of APT leading to reduction of surface area, suggesting the agglomerated and damaged of fiber-like structure of WO_3 may not favorable in electrochemical performance purpose. Furthermore, the increase in capacitance is linearly dependent on the surface area and pore volume.

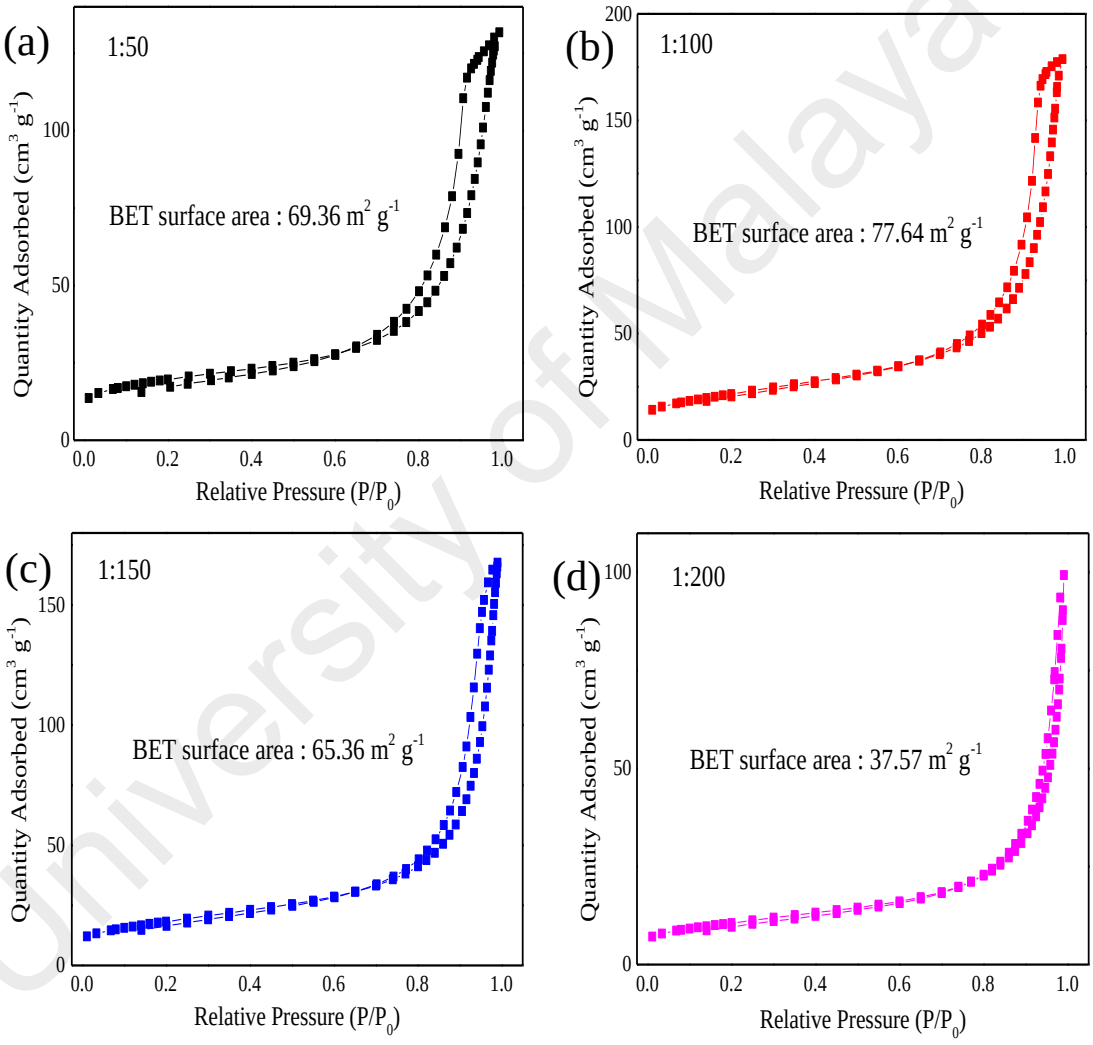

Figure 4.8: N_2 adsorption/desorption isotherms of P-rGO/WO_3 nanocomposites prepared at different loading amount of APT (P-rGO:APT) (a) 1:50, (b) 1:100, (c) 1:150 and (d) 1:200.

Table 4.3: Results of BET analysis of P-rGO/WO_3 nanocomposites prepared at different loading amount of APT (P-rGO:APT).

Samples	BET surface area (m^2 g^{-1})	Pore volume (cm^3 g^{-1})	Pore size (nm)
1:50	69.36	0.22	13.7
1:100	77.64	0.24	12.5
1:150	65.36	0.22	14.5
1:200	37.57	0.15	16.9

Figure 4.9 (a) shows the CV curves of P-rGO/WO_3 nanocomposite with different loading amounts of APT. The CV curves of the P-rGO/WO_3 nanocomposite exhibited nearly rectangular-like shapes with minor redox peaks. This implied that the P-rGO/WO_3 samples demonstrated the combination effects between the double-layer capacitance and pseudocapacitance (Peng et al., 2014), and the two pairs of cathodic and anodic peak corresponded well to the reversible reactions of W^{6+} <=> W^{5+} and W^{5+} <=> W^{4+} (Wang et al., 2014a). These findings were in line with the results of the aforementioned Raman studies (Figure 4.5 (b)), in which various oxidation state such as W^{6+}, W^{5+} and W^{4+} were found in tungsten metal as the result of ion reduction by intercalation into a solid electrode by means of faradaic oxidation/reduction reactions. On top of that, Figure 4.9 (b) illustrates that the specific capacitances of 1:50-, 1:100-, 1:150- and 1:200-P-rGO/WO_3 nanocomposites were found to be 60.6, 97.6, 41.4 and 10.3 F g^{-1}, respectively. The reduction of the specific capacitance of P-rGO/WO_3 nanocomposites with increasing the APT loading was mainly attributed to the agglomeration of WO_3. This is associated with the fact that agglomeration resulted in the decrease of surface area and eventually lowered the energy storage (Song et al., 2016).

Accordingly, Nyquist plots could be divided into three different frequency regions, namely high frequency, middle frequency and low frequency. At high frequency, the intercept of semicircle based on the real axis represented the equivalent series resistance (ESR the internal resistance between active material, electrode substrate and electrolyte). The diameter of semicircle at the middle frequency corresponded to the charge-transfer resistance (R_{ct}), while the straight line at the low frequency region was associated with the diffusion of ion or protons into the electrode surface, so-called the Warburg impedance (Xu et al., 2016). It is clearly illustrated in Figure 4.9 (c) that R_{ct} decreased with increasing the APT loading up to 1:100 of mass ratio, after which there was an increase. The R_{ct} value of 1:100 sample was detected to be 11.13 Ω, which was lower than that of those 1:50 (13.21 Ω), 1:150 (15.96 Ω) and 1:200 (21.58 Ω). This gave us a hint that 1:100 sample possessed the highest accessibility of ions within the electrode. Additionally, the inset in Figure 4.9 (c) also showed that the slope of the straight line for 1:100 was much steeper than others, suggesting a better mobility of ions (Sahu et al., 2015). This was mainly due to the fact that small diameter of fiber-like WO_3 possessed a shorter diffusion length for electrolyte access. Apart from that, at the high frequency region, a single peak designated as φ was also obtained at high frequency region (Figure 4.9 (d)). 1:200- and 1:150- composites showed almost similar value of φ_1 and φ_2, while the 1:100- composite exhibited the highest φ value at high frequency region (φ_3), implying that 1:100- composite acquired the highest specific capacitance. Taking these facts into consideration, it could be concluded that 1:100 of P-rGO:APT was the optimum mass ratio to obtain fiber-like WO_3 with high electrochemical performance.

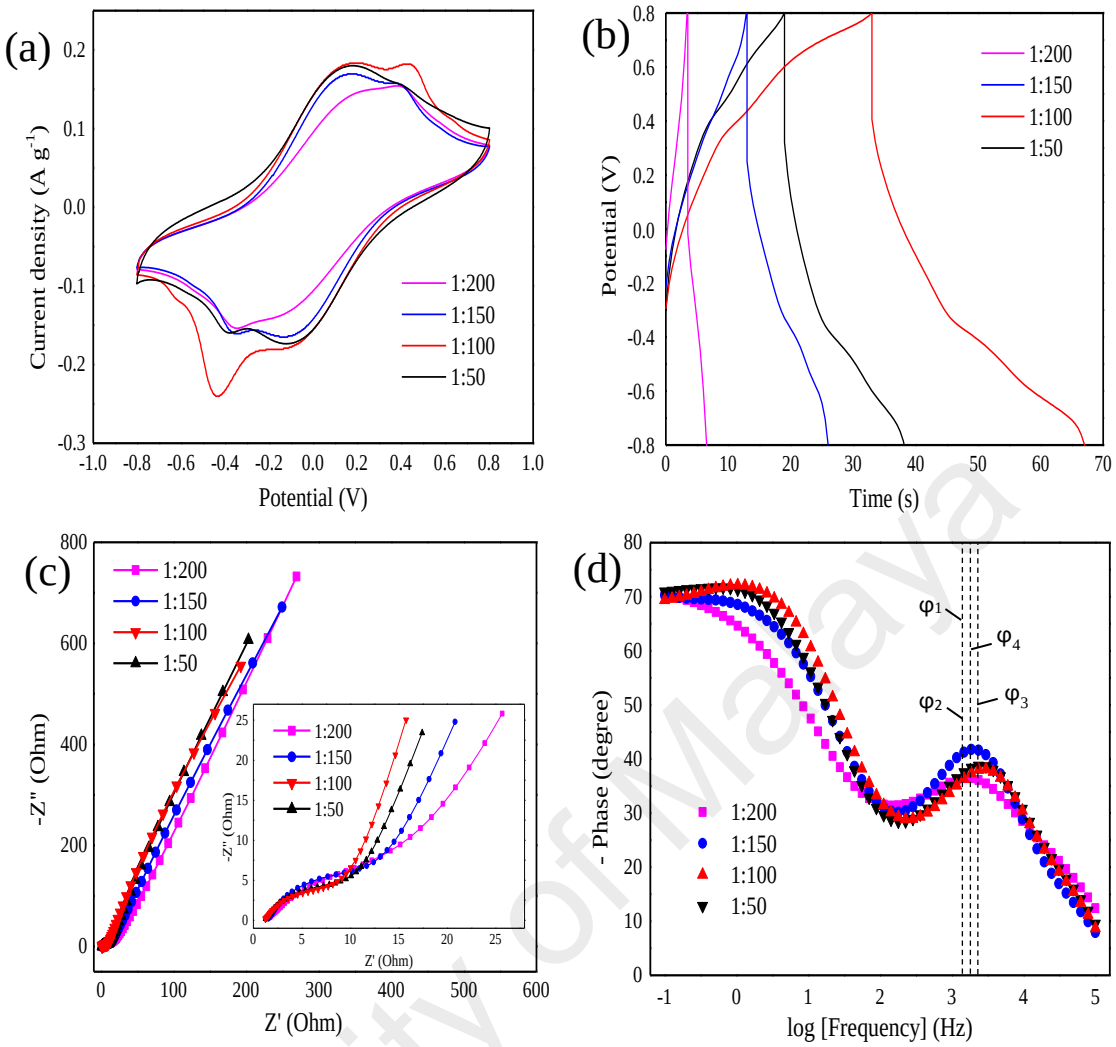

Figure 4.9: Electrochemical performances of P-rGO/WO_3 nanocomposites prepared at different loading amount of APT. (a) Cyclic voltammogram measured at scan rate of 25 mV s^{-1}; (b) Galvanostatic charge/discharge curves measured at current density of 0.7 A g^{-1}; (c) Nyquist plot of P-rGO/WO_3 nanocomposites (the inset of enlarged high frequency region); and (d) Bode phase plot for P-rGO/WO_3 nanocomposites in 1 M Na_2SO_3 electrolyte.

4.3.2 The Influence of Hydrothermal Temperature

It is worth to mention that the hydrothermal temperature has significant effects on the crystallinity and morphology of P-rGO/WO_3 nanocomposites. Of interest is, as shown in Figure 4.10 (a), only the hexagonal phase of WO_3 (JCPDS 85-2460) could be detected in XRD patterns by increasing the hydrothermal temperature progressively from 120 to 180 ºC. This is ascribed to the fact that the crystallinity of P-rGO/WO_3 nanocomposites increased as the hydrothermal temperature rose, suggesting the higher the temperature the more mature the crystal (Huang et al., 2012).

Figure 4.10 (b) illustrates the Raman spectra of P-rGO/WO_3 nanocomposites by the hydrothermal method at different reaction temperature. It can be seen that the reaction temperature has negligible effect on the Raman spectra. Three obvious peaks at 190, 290 and 327 cm^{-1} were assigned to the lattice modes, the W^{4+}-O mode and the W^{5+}-O mode, respectively. The peaks at 686 and 781 cm^{-1} attributed to the stretching modes of a long W^{6+}-O and a short W^{6+}-O bond, respectively while the peaks within 916-951 cm^{-1} indicated that WO_3 contained a large number of dangling bonds at its surface (Shi et al., 2016). This explained the formation of fiber-like structure. The emergence of broad peak in the lower wavenumber region (200-300 cm^{-1}), revealed the existence of low-valence-state W-O bending mode (Rajagopal et al., 2009). Additionally, the D and G bands were also clearly observed in P-rGO/WO_3 nanocomposite, suggesting the presence of P-rGO. Specifically, the D band peak appeared at 1338-1348 cm^{-1} was ascribed to the disorder-induced vibration of C-C bonds, while the G band peak located at 1594-1611 cm^{-1} arose from the C-C vibrations of sp^2 orbital structure.

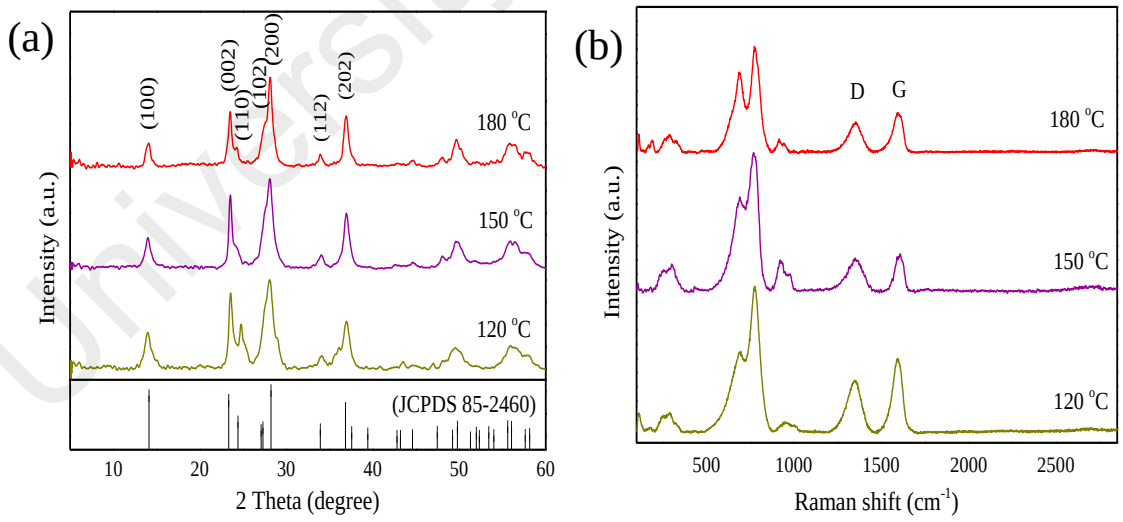

Figure 4.10: (a) XRD ptterns and (b) Raman spectra of P-rGO/WO_3 nanocomposite synthesized with different hydrothermal temperatures.

Figure 4.11 (a-c) displays the morphological evolution of the P-rGO/WO_3 nanocomposites containing 1:100 of P-rGO:APT synthesized at different hydrothermal temperatures. From the nanofiber length histogram given in Figure 4.11, it was found that WO_3 nanoplates obtained at 120 ºC was relatively small and short with measured length of 38.55 nm considering these nanoplates were typically bound together to form tight bundles on the surface of rGO as seen in Figure 4.11 (a). One possible explanation is that 120 ºC was insufficient to overcome the potential energy barrier to transform WO_3 to nanofibers from nanoplates (Adhikari and Sarkar, 2014). On top of that, the formation of relatively large architecture might be attributed to low diffusion rate of nanoparticles at low temperature (Zhang et al., 2014). It was interesting to observe that WO_3 grew up in thin fiber-like form without suffering from agglomeration when the hydrothermal temperature was increased to 150 ºC (Figure 4.11 (b)). Table 4.4 reveals the measured length of WO_3 nanofiber increases with increasing temperature to 150 ºC. However, as shown in Figure 4.11 (c), fiber-like structure of WO_3 started to agglomerate to minimize the surface energies when the temperature was further increased to 180 ºC (Huang et al., 2008). Considering these facts, it could be concluded that 150 ºC was the optimum hydrothermal temperature to grow the nanofibers with a uniform structure.

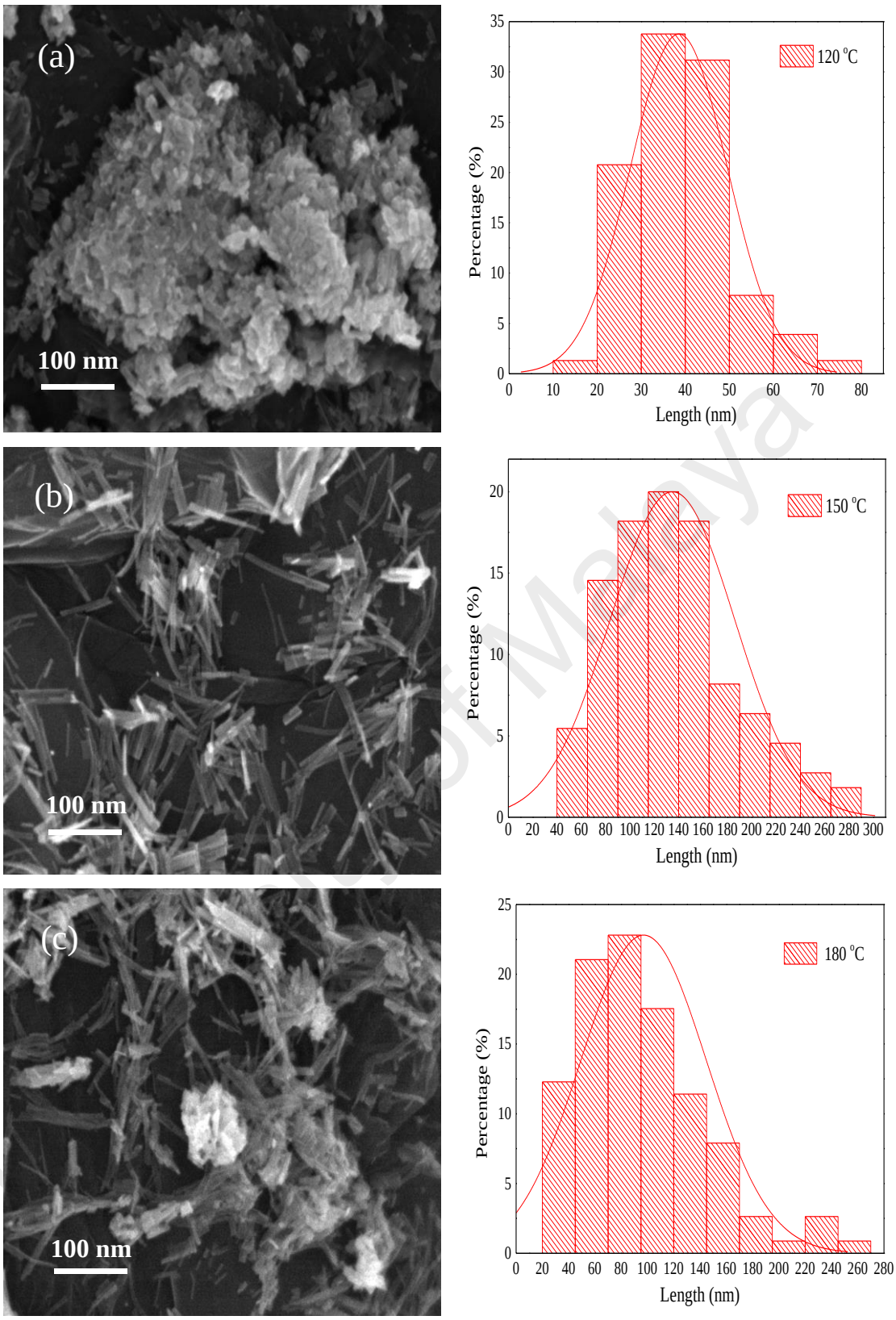

Figure 4.11: FESEM images of P-rGO/WO_3 nanocomposite synthesized with different hydrothermal temperature (a) 120 °C, (b) 150 °C, and (c) 180 °C and corresponding nanofiber length distribution (right).

Table 4.4: Length of P-rGO/WO_3 nanocomposite synthesized with different hydrothermal temperature.

Samples	Length (nm)
120 ºC	38.55
150 ºC	134.87
180 ºC	97.05

The N_2 adsorption/desorption isotherms of P-rGO/WO_3 nanocomposites prepared at different hydrothermal temperatures are shown in Figure 4.12 (a-c). All the isotherms show a similar Type V isotherms and H1 hysteresis loop is found at the end of the curve ($0.7 < P/P_0 < 1.0$). This hysteresis loop indicating the presence of both mesoporous and macroporous structure. At the beginning of the curve ($P/P_0 < 0.1$), a slightly increase in volume is related to the existence of small amount micropore structures. Surface area calculated by BET model are shown in each isotherm. The well-defined fiber-like structure of WO_3 in P-rGO/WO_3 nanocomposites give rise to a relatively high BET surface area of 85.75 $m^2 g^{-1}$ and the pore volume is around 0.30 $cm^3 g^{-1}$ as presented in Table 4.5. Such high surface area and appropriate pore volume, which is beneficial for rapid electron transport between the electrolyte and electrode. It is worthy to mention that the pore volume decreased with increasing the hydrothermal temperature to 180 ºC, which probably owing to the agglomeration of fiber-like WO_3 to minimize the surface energies.

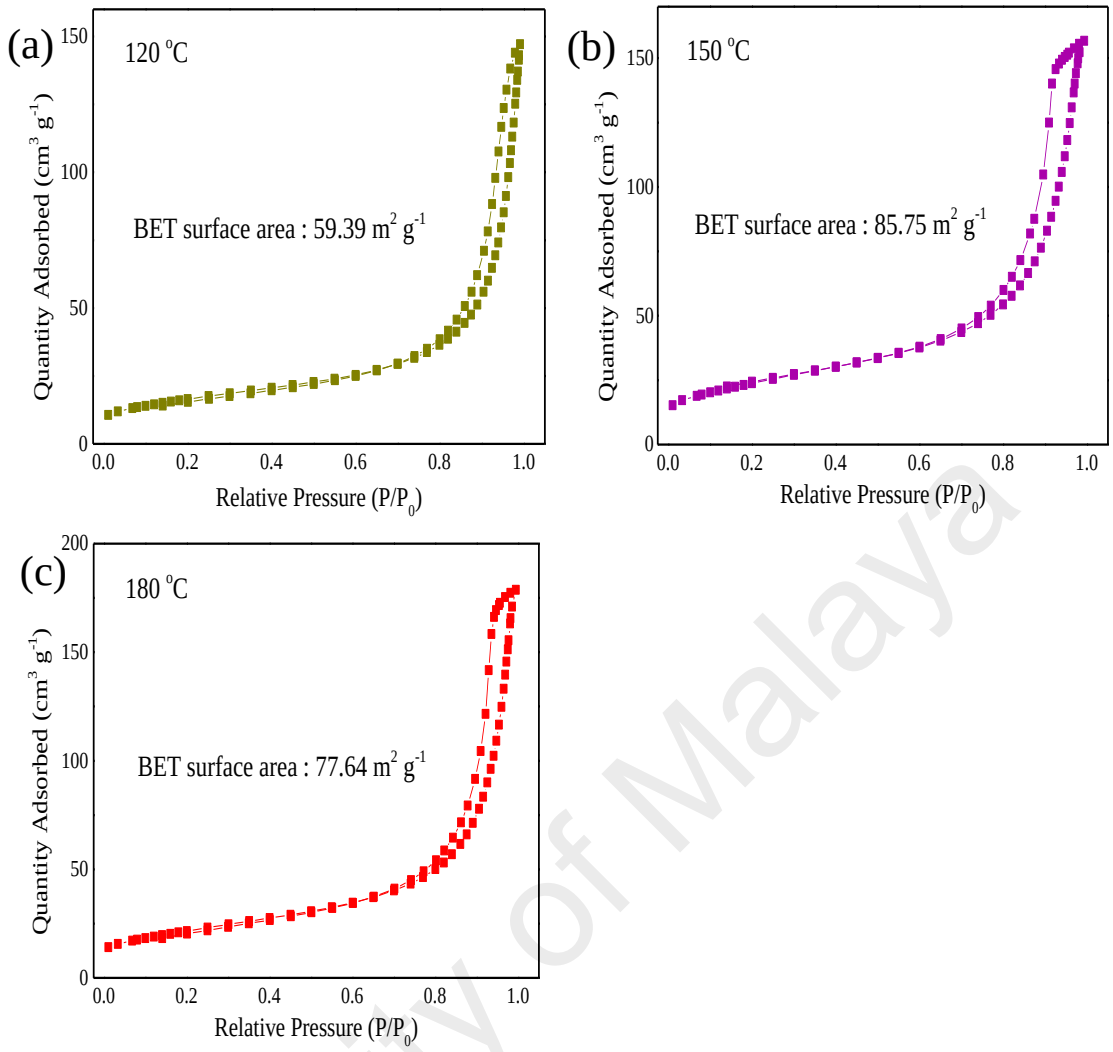

Figure 4.12: N_2 adsorption/desorption isotherms of P-rGO/WO_3 nanocomposite synthesized with different hydrothermal temperature (a) 120 °C, (b) 150 °C, and (c) 180 °C.

Table 4.5: Results of BET analysis of P-rGO/WO_3 nanocomposite synthesized with different hydrothermal temperature.

Samples	BET surface area (m^2 g^{-1})	Pore volume (cm^3 g^{-1})	Pore size (nm)
120 °C	59.39	0.20	15.5
150 °C	85.75	0.31	9.7
180 °C	77.64	0.24	12.5

As shown in Figure 4.13 (a), a symmetric shape of CV loop with a pair of redox peaks was recorded. This suggested the pseudocapacitive charge/discharge characteristics during the reversible intercalation/de-intercalation of ions leading to an additional capacitance. Figure 4.13 (b) shows the specific capacitance values of the P-rGO/WO_3 nanocomposites calculated from the discharge curves. The specific capacitances for samples synthesized at 120, 150, and 180 ºC were determined to be 20.9, 274.0 and 97.6 F g^{-1}, respectively. It is worth to mention that the significant improved electrochemical performance of the sample synthesized at 150 ºC may be ascribed to the thin fiber-like WO_3 acting as the spacer to inhibit the agglomeration of P-rGO (An et al., 2012), which could subsequently increase the surface area for the electrolyte access and promote the mobility of ions. Apart from that, it was found that the sample prepared at 120 ºC exhibited the lowest specific capacitance because of 120 ºC might be insufficient to get rid of the potential energy barrier to form fiber-like WO_3. At 180 ºC, the low specific capacitance was presumably dominated by the agglomeration of fiber-like WO_3. Additionally, the sample prepared at 150 ºC (6.92 Ω) exhibited a semicircle smaller than that of those 120 and 180 ºC (Figure 4.13 (c)). The smaller diameter of semicircle (R_{ct}) might be attributed to the direct WO_3 grown on P-rGO allowing higher diffusion of electrolyte ion at electrode interface (Rakhi et al., 2016). In comparison with 120 and 180 ºC, the straight line slope of the sample prepared at 150 ºC was greater than that of 45º, revealing a superior capacitive behavior with low diffusion resistance (inset Figure 4.13 (c)). It is also clearly shown in Figure 4.13 (d) that the composite synthesized at 150 ºC possessed a relatively lower diffusive resistance considering only the single peak (φ_2) was observed at high frequency region. This is ascribed to the fact that the introduction of 1D h-WO_3 into P-rGO could prevent the agglomeration of P-rGO and reduce the path length for ions diffusion.

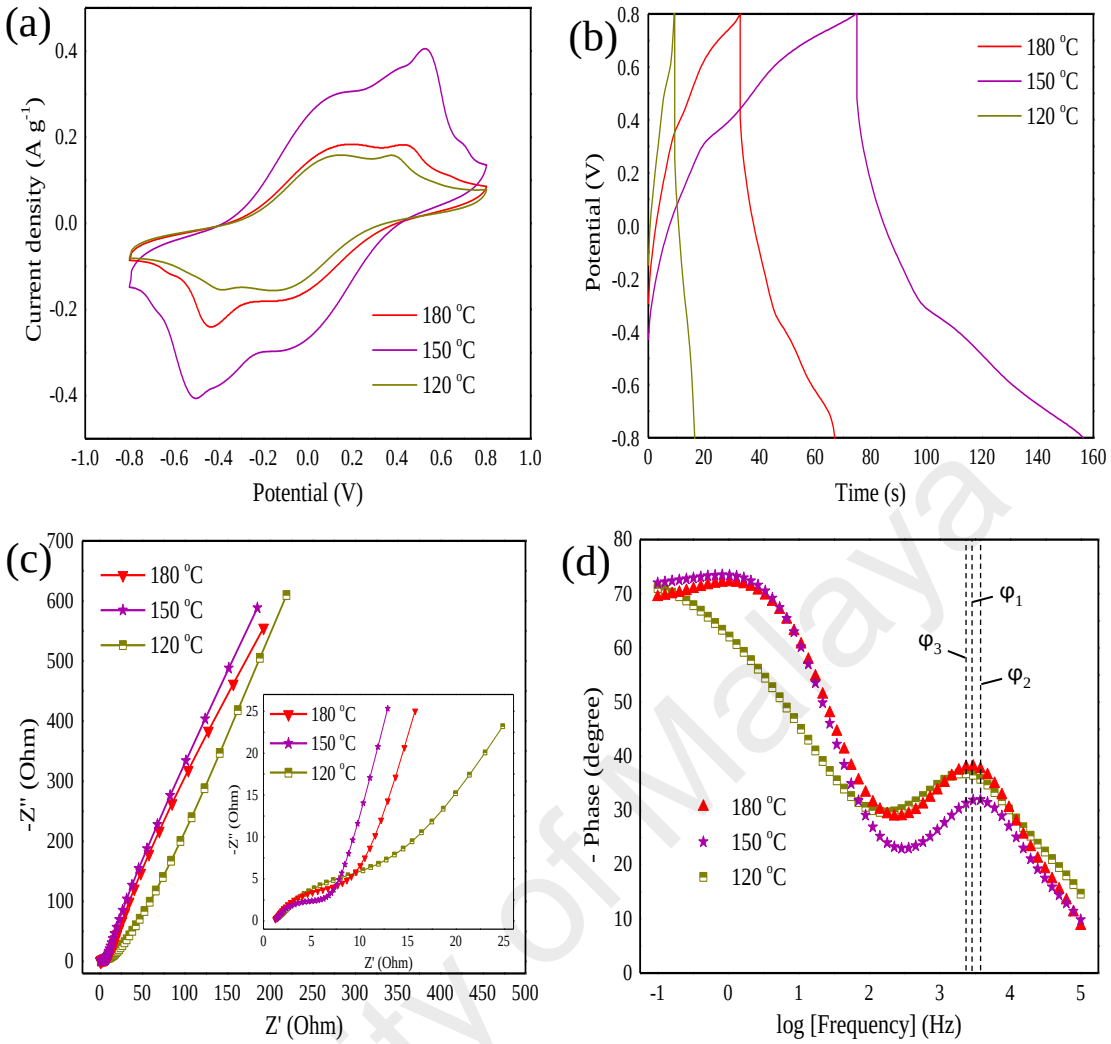

Figure 4.13: Electrochemical performances of P-rGO/WO_3 nanocomposites prepared at different hydrothermal temperature. (a) Cyclic voltammogram measured at scan rate of 25 mV s^{-1}; (b) Galvanostatic charge/discharge curves measured at current density of 0.7 A g^{-1}; (c) Nyquist plot of P-rGO/WO_3 nanocomposites (the inset of enlarged high frequency region); and (d) Bode phase plot for P-rGO/WO_3 nanocomposites in 1 M Na_2SO_3 electrolyte.

4.3.3 The Influence of Reaction Time

The influence of reaction time in synthesizing P-rGO/WO_3 nanocomposites by hydrothermal method was also evaluated in the present work. As demonstrated in Figure 4.14 (a), reaction time did not affect and alter the crystalline phase of P-rGO/WO_3 nanocomposites. Only hexagonal phase of WO_3 (JCPDS 85-2460) was detected and there was no obvious peak of other phases observed, indicating the samples consisted of pristine h-WO_3 phase.

As shown in Figure 4.14 (b) Raman spectra of the as-prepared P-rGO/WO_3 nanocomposites exhibited five main peaks: two W^{6+}-O stretching vibrations at approximately 682-694 and 768-777 cm^{-1}, one W^{5+}-O bending mode at 293-308 cm^{-1}, one W^{4+}-O bending vibration at 251-258 cm^{-1}, and one W^{6+}=O stretching mode at 919-946 cm^{-1}. The D band peaks for the P-rGO/WO_3 nanocomposites were positioned at 1346-1354 cm^{-1}, while the G band peaks were observed at 1505-1611 cm^{-1}, respectively. It is noteworthy that the intensity of D band peaks increased with increasing hydrothermal reaction time from 5 to 10 h due to the decreased of order in the carbon lattice (Rusi, 2015). Moreover, the interaction between the fiber-like structure of WO_3 and P-rGO nanosheets contributes to the enhancement of sp^3 defects in carbon (Wang et al., 2013). When the reaction duration was increased to 15 h, the growth of WO_3 on top of the P-rGO increased the W^{6+}-O stretching mode of WO_3 (denoted at 682-694 and 768-777 cm^{-1}), which in turn, reduced the peak intensity of D band in the nanocomposite (Ahmad et al., 2016).

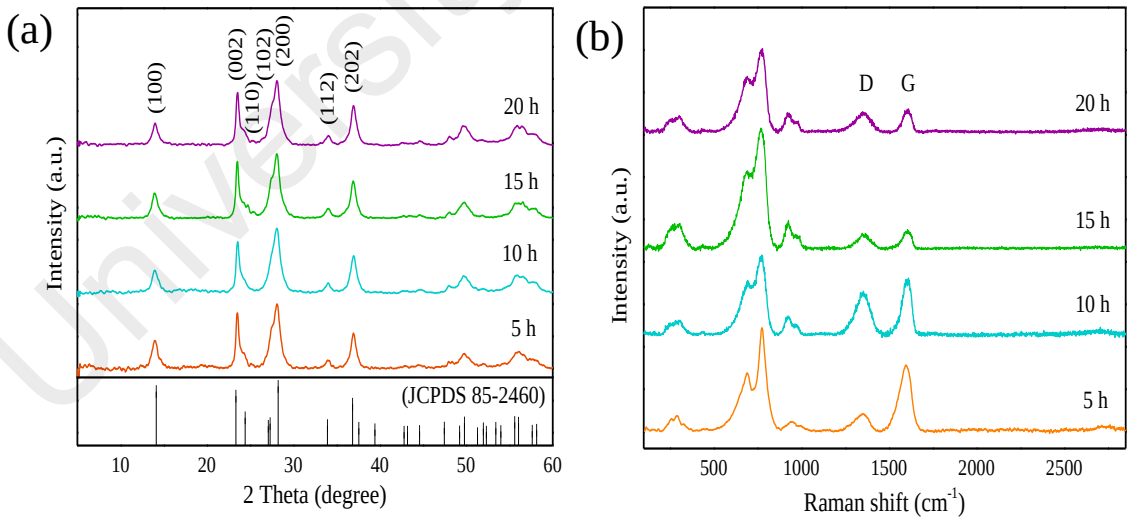

Figure 4.14: (a) XRD patterns and (b) Raman spectra for the influence of reaction time at 150 °C with ratio of 1:100 for P-rGO:APT.

FESEM was adopted in the present work to understand the influence of reaction time over the formation of fiber-like h-WO_3 nanostructures. It is clearly illustrated in Figure 4.15 (a-d) the morphology of the P-rGO/WO_3 nanocomposites was strongly influenced by the reaction times. Correspondingly, the length of nanofibers were found to increase with prolonged reaction time. Figure 4.15 (a) demonstrated that fiber-like structure of WO_3 with some non-uniform plates was just first formed after reaction of 5 h. The average nanofiber length of the sample were determined from the length distribution histogram as shown in Figure 4.16. Refer to Table 4.6, the obtained WO_3 plates had an average length of 50.98 nm. It is also found that fiber-like structure of WO_3 started to form with prolonging the reaction time to 10 h even though all samples possessed hexagonal lattice structure (Figure 4.14 (a)). With prolonging the reaction time to 15 h, a higher amount of fiber-like structure of WO_3 was observed on top of the P-rGO and the length of nanofibers was found to increase to 87.29 nm. However, the size and shape in the fiber-like WO_3 were considerably irregular and not homogeneous. It is interesting to note that a well-defined fiber-like WO_3 with length of about 134.87 nm, was obtained by further increasing the reaction time to 20 h (Figure 4.15 (d)). Based on these observations, it could be concluded that the growth mechanism of WO_3 altered from plate- to fiber-like structures with reaction time.

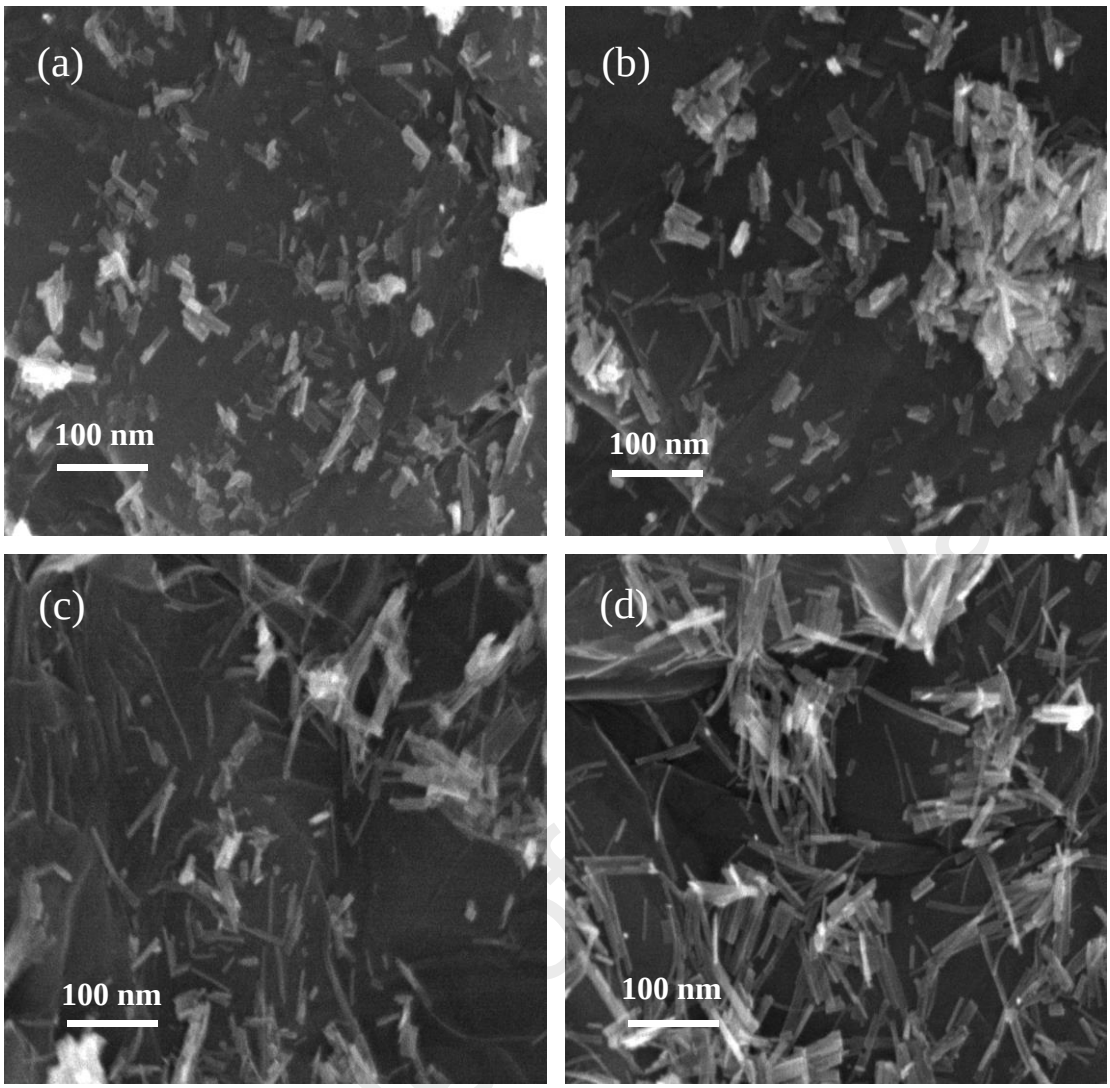

Figure 4.15: FESEM images of P-rGO/WO_3 nanocomposite synthesized with different reaction time (a) 5 h, (b) 10 h, (c) 15 h and (d) 20 h.

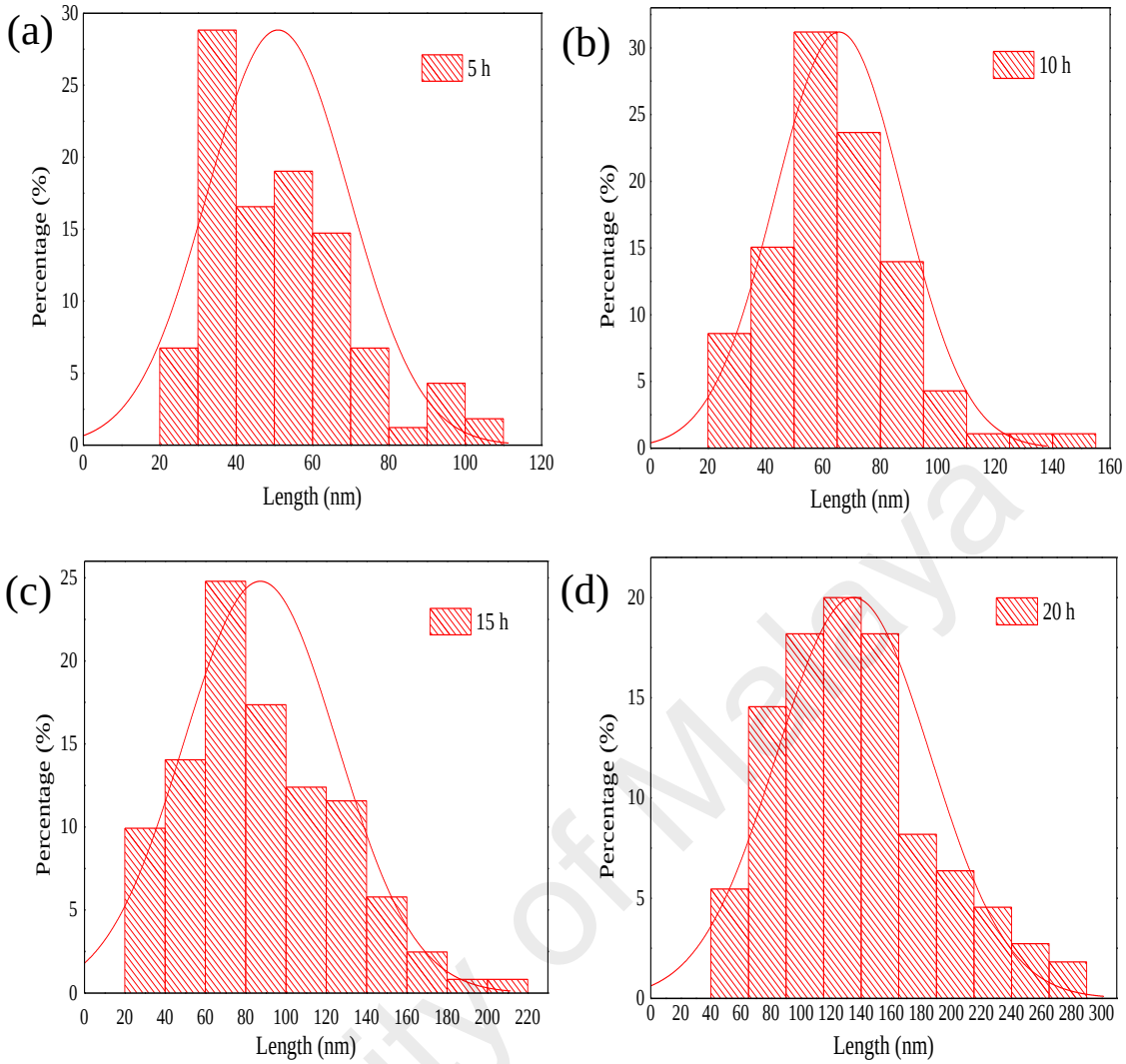

Figure 4.16: Length of P-rGO/WO_3 nanocomposite synthesized at reaction time (a) 5 h, (b) 10 h, (c) 15 h and (d) 20 h.

Table 4.6: Length of P-rGO/WO_3 nanocomposite synthesized with different reaction time.

Samples	Length (nm)
5 h	50.98
10 h	65.60
15 h	87.29
20 h	134.87

Figure 4.17 discloses the N_2 adsorption/desorption isotherms of P-rGO/WO_3 nanocomposites prepared at different reaction times. The corresponding isotherms exhibited Type V curve with noticeable H1 hysteresis loop at P/P_0 = 0.7 to 1.0, which are typically associated with mesoporous material. The BET surface area of P-rGO/WO_3 nanocomposites generally increases in the following order: 5 h < 10 h < 15 h < 20 h, from 79.86 to 85.75 m^2 g^{-1}, respectively. The results from BET analysis are well in agreement with the FESEM morphology, suggesting longer in length of fiber-like WO_3 possess the highest surface area for the contact of ions and thus better electrochemical performance can be obtained as depicts in Table 4.7 (Birch et al., 2013; Chowdhury et al., 2009).

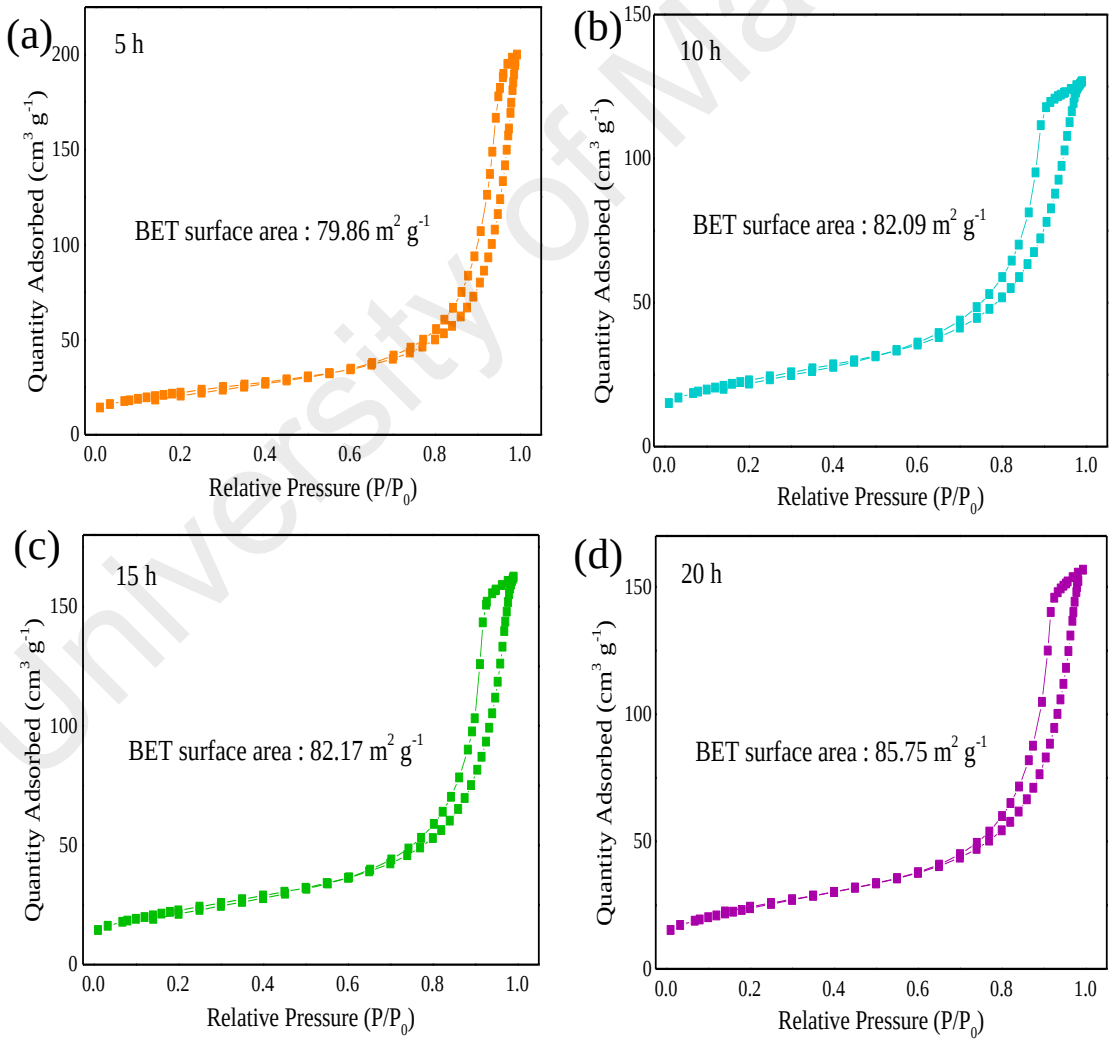

Figure 4.17: N_2 adsorption/desorption isotherms of P-rGO/WO_3 nanocomposite synthesized with different reaction time (a) 5 h, (b) 10 h, (c) 15 h and (d) 20 h.

Table 4.7: Results of BET analysis of P-rGO/WO_3 nanocomposite synthesized with different reaction time.

Samples	BET surface area (m^2 g^{-1})	Pore volume (cm^3 g^{-1})	Pore size (nm)
5 h	79.86	0.25	11.7
10 h	82.09	0.26	11.4
15 h	82.17	0.28	11.3
20 h	85.75	0.31	9.7

The CV spectra of P-rGO/WO_3 nanocomposite prepared at various reaction times showed obvious cathodic peaks at 0.2 and 0.5 V and the anodic peaks at -0.2 and -0.5 V. Accordingly, these peaks corresponded to the occurrence of reversible reaction features, i.e., $W^{4+} \rightarrow W^{5+}$ and $W^{5+} \rightarrow W^{6+}$ for cathodic peaks; $W^{6+} \rightarrow W^{5+}$ and $W^{5+} \rightarrow W^{4+}$ for anodic peaks (Figure 4.18 (a)). Figure 4.18 (b) shows the dependency of the specific capacitance on the synthesis duration. The calculated specific capacitances for the composites prepared at 20, 15, 10 and 5 h were found to be 274.0, 245.9, 208.9 and 120.9 F g^{-1}, respectively. As expected, the specific capacitance of the composites increased with increasing the synthesis duration. One possible explanation is that a longer synthesis duration provided sufficient time for the WO_3 to be transformed from plate-like to fiber-like morphology. It has also been reported that well-defined fiber-like WO_3 was more desirable for supercapacitors as it provided a shorter diffusion pathway and offered more reactive site for electrolyte facilitating intercalation/de-intercalation of ions or electrons between electrode and electrolyte interface. Furthermore, as indicated in Figure 4.18 (c), R_{ct} was found to decrease with increasing the synthesis reaction time in which the measured R_{ct} values were 19.59, 16.64, 14.34 and 6.92 Ω for 5, 10, 15 and 20 h, respectively. A steeper vertical slope was also observed in sample synthesized at 20 h (Figure 4.18 (c)). Figure 4.18 (d) shows that the phase angle of composite followed a decreasing order of 20 h (-72 º), 15 h (-69 º), 10 h (-67 º) and 5 h (-67 º). This finding indicated the sample synthesized at 20 h was closer to the ideal capacitor behavior (-90 º)

(Balasubramaniam and Balakumar, 2016). Based on the above results, the optimum conditions for the preparation of rGO/WO_3 nanocomposites were found to be 1:100 of P-rGO:APT, 150 ºC of hydrothermal temperature and 20 h of duration.

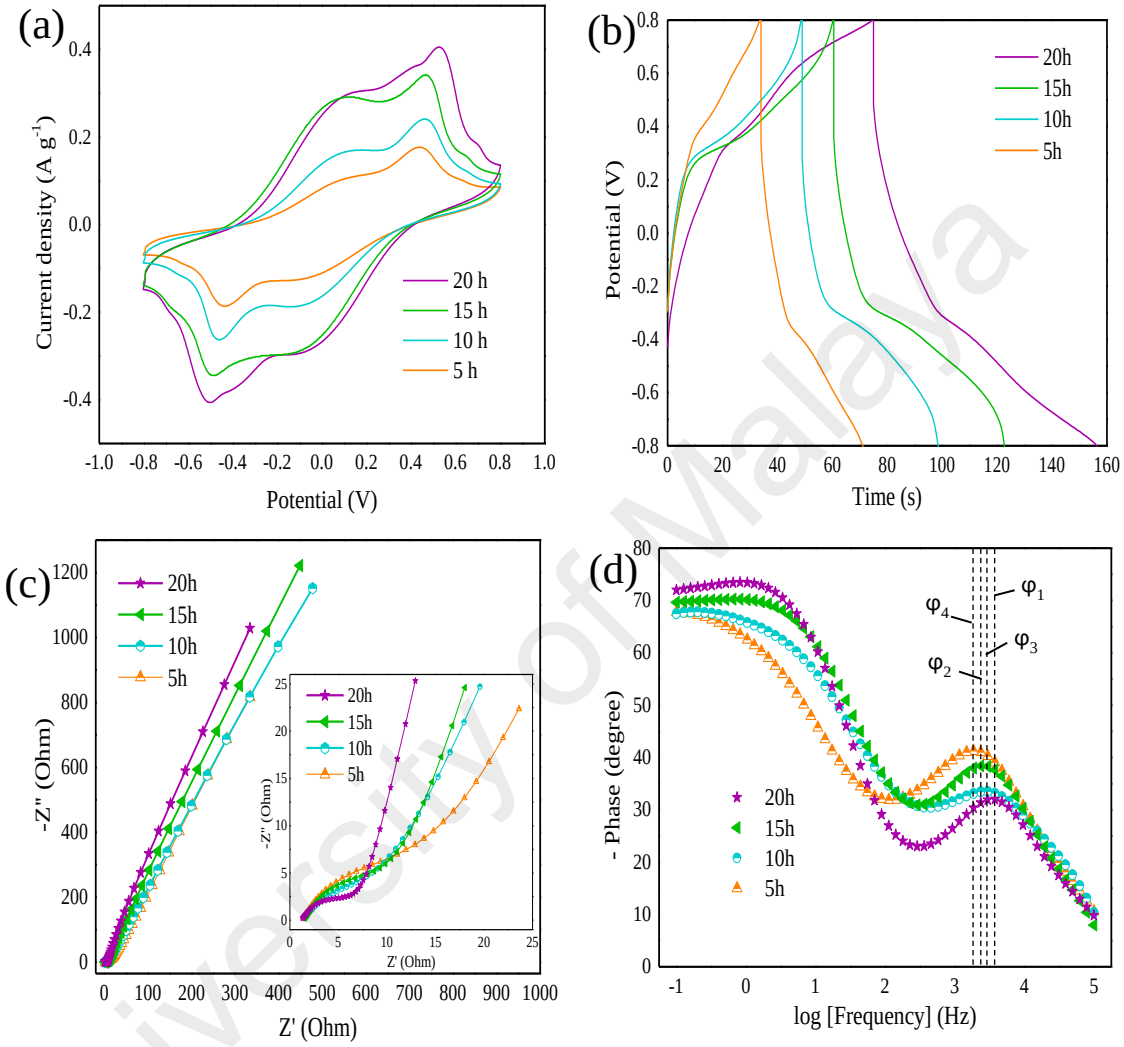

Figure 4.18: Electrochemical characterizations of P-rGO/WO_3 nanocomposites prepared at different reaction time. (a) Cyclic voltammogram at scan rate of 25 mV s^{-1}; (b) Galvanostatic charge/discharge curves at current density of 0.7 A g^{-1}; (c) Nyquist plot of P-rGO/WO_3 nanocomposites (the inset of enlarged high frequency region); and (d) Bode phase plot for P-rGO/WO_3 nanocomposites in 1 M Na_2SO_3 electrolyte.

4.3.4 Formation of P-rGO/WO_3 Nanocomposites

Based on aforementioned discussion, P-rGO/WO_3 nanocomposite was synthesized using hydrothermal technique under optimum conditions. The possible formation and growth mechanisms of fiber-like WO_3 in P-rGO/WO_3 nanocomposite was proposed and illustrated in Figure 4.19. At the early stage, tungstic acid (H_2WO_4) was formed by the addition of HCl into the APT solution. The H_2WO_4 colloidal solution formed was not stable and thereby tended to be hydrolyzed to form the hydrated tungsten oxides (WO_3•H_2O) within a couple of hours. Considering this fact, H_2WO_4 colloidal solution should just be stirred for a certain duration to prevent the formation of WO_3•H_2O precipitates (Kalanur et al., 2013). It has also been reported in literatures that H_2WO_4 would decompose to form h-WO_3 nuclei under relatively high pressure and temperature (hydrothermal conditions) (Zhu et al., 2014).

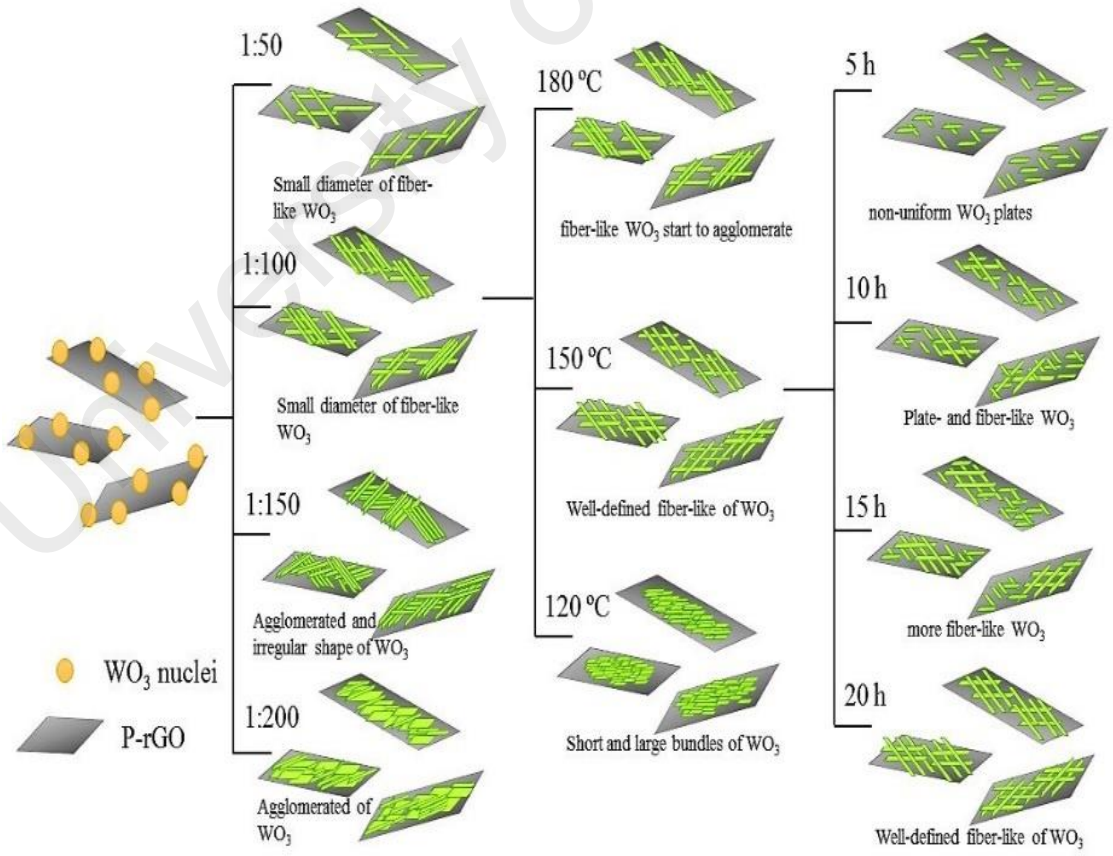

Figure 4.19: Proposed formation mechanism of fiber-like WO_3 in P-rGO/WO_3 nanocomposites.

4.4 Comparison of P-rGO/WO_3 Nanocomposites and WO_3

In order to have a better understanding on the synergistic effects between WO_3 and P-rGO, the properties of obtained P-rGO/WO_3 nanocomposite and pure WO_3 and their supercapacitor performance are investigated in this section. For comparison purpose, pure WO_3 was prepared under the same optimum conditions.

As presented in Figure 4.20, the P-rGO/WO_3 nanocomposite shows XRD patterns similar to those WO_3 but with lower intensity. It may be due to the presence of amorphous nature of P-rGO (Sahu et al., 2015). Noticeably, there are no P-rGO diffraction peaks (2θ = 24.5º) observed in the composite, indicating the fiber-like WO_3 are successfully anchored on the surface of P-rGO leading to disordered structure of P-rGO instead of well-stacked sheets (Cheng et al., 2014).

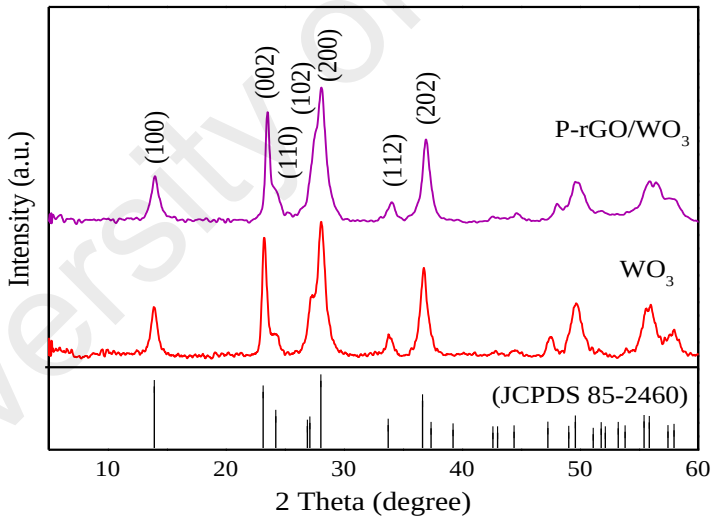

Figure 4.20: XRD pattern of P-rGO/WO_3 nanocomposite and WO_3.

Figure 4.21 displays the Raman spectra of P-rGO/WO_3 nanocomposite and WO_3. In contrast, the pure WO_3, the Raman peak of WO_3 at 710 cm^{-1} is broadened and downshifted to 682 cm^{-1} in P-rGO/WO_3 nanocomposite, probably due to the formation of W-O-C bonds and weaken the initial W=O bonds. This finding is in agreement with Guo et al. (2012) and Jie at al. (2015). Compared with the P-rGO (0.84), the I_D/I_G of

P-rGO/WO_3 nanocomposite increased to 0.86, showing that the P-rGO was further reduced during hydrothermal treatment with the assistance of APT and thus create more defects.

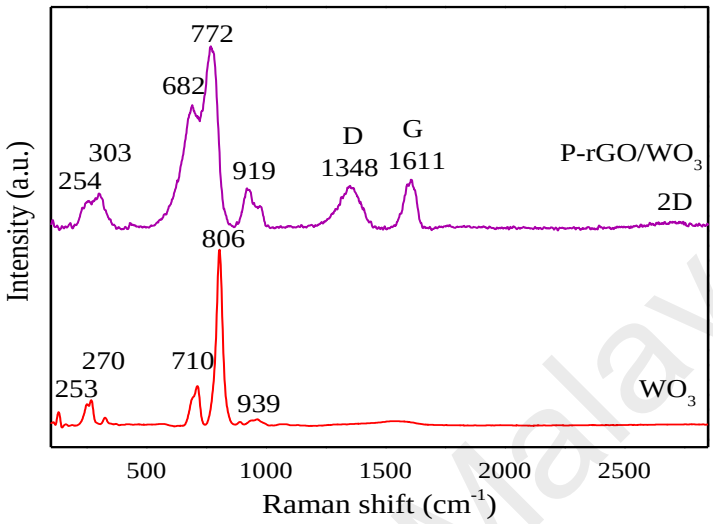

Figure 4.21: Raman spectra of P-rGO/WO_3 nanocomposite and WO_3.

FESEM images of WO_3 and P-rGO/WO_3 nanocomposite are depicted in Figure 4.22 (a) and (b), respectively. It is obviously seen that WO_3 exhibits fiber-like morphology and assembled by large number of individual nanofibers stacked together. As observed in Figure 4.22 (b), the addition of large surface area of P-rGO sheets could facilitate the growth of WO_3, leading to the WO_3 nanofibers homogenously decorated on the P-rGO sheets. The EDX spectrum in Figure 4.22 (c) implied that the synthesized P-rGO/WO_3 nanocomposite composed of carbon (C), tungsten (W) and oxygen (O) peaks, indicating the elementary composition of sample is pure (Yaqoob et al., 2016).

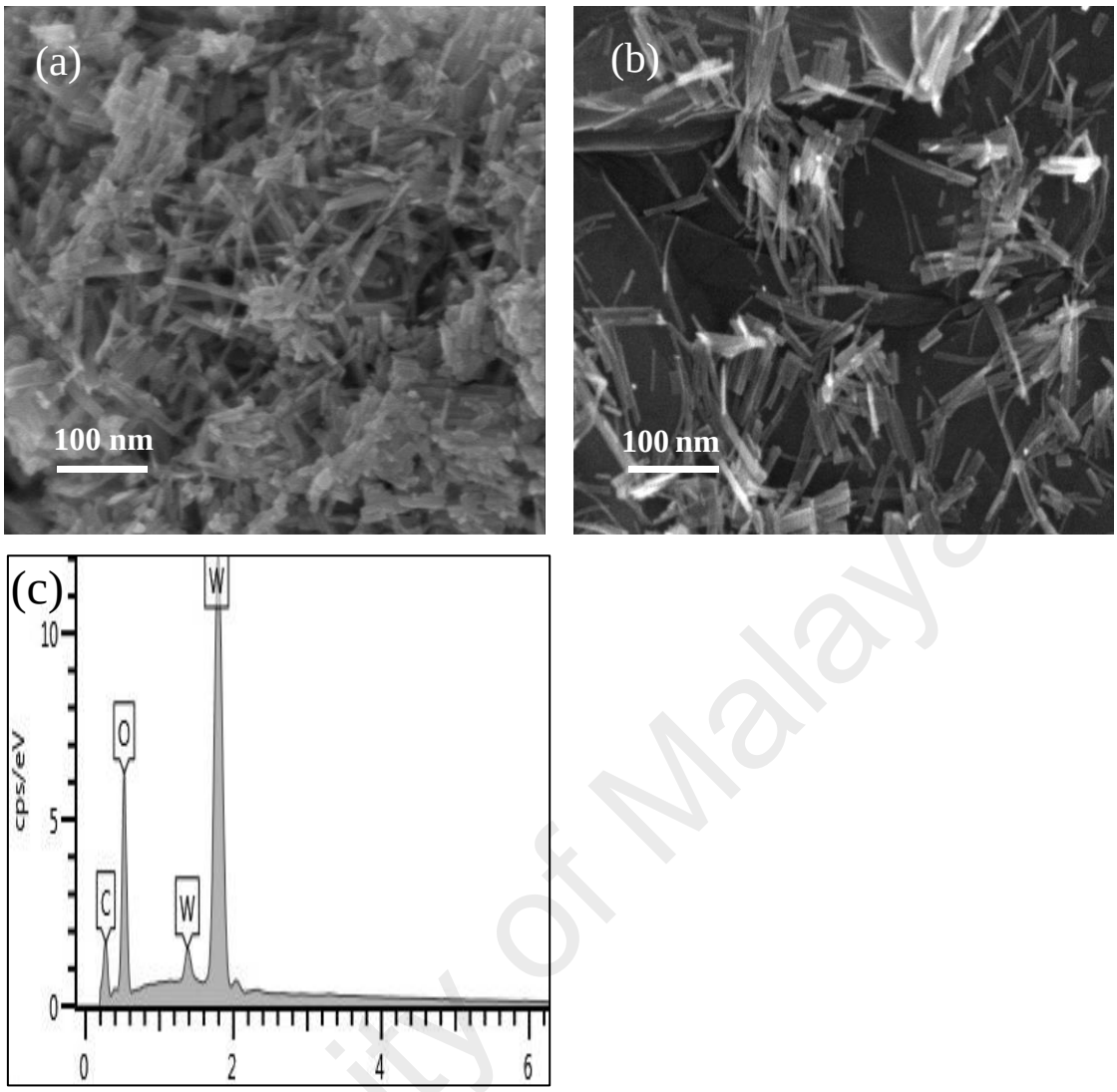

Figure 4.22: FESEM images of (a) WO_3, (b) P-rGO/WO_3 nanocomposite and (c) EDX spectrum of P-rGO/WO_3 nanocomposite.

Figure 4.23 (a) demonstrates the TEM image of the synthetic WO_3 without the addition of P-rGO. In the bulk WO_3, fibers-like WO_3 aggregated severely. After the formation of composite, both components of WO_3 and P-rGO act as spacers to diminish the agglomeration of each other and thus significantly increasing the surface area for electrolyte access (Figure 4.23 (b)) (Liang et al., 2016). As shown in Figure 4.23 (c), the measured lattice fringe spacing between the adjacent planes is about 0.38 nm in P-rGO/WO_3 nanocomposite which is in accordance with the lattice spacing of the (002) planes of h-WO_3 (Gao et al., 2013). This indicates that the h-WO_3 may preferably grow along the (002) direction.

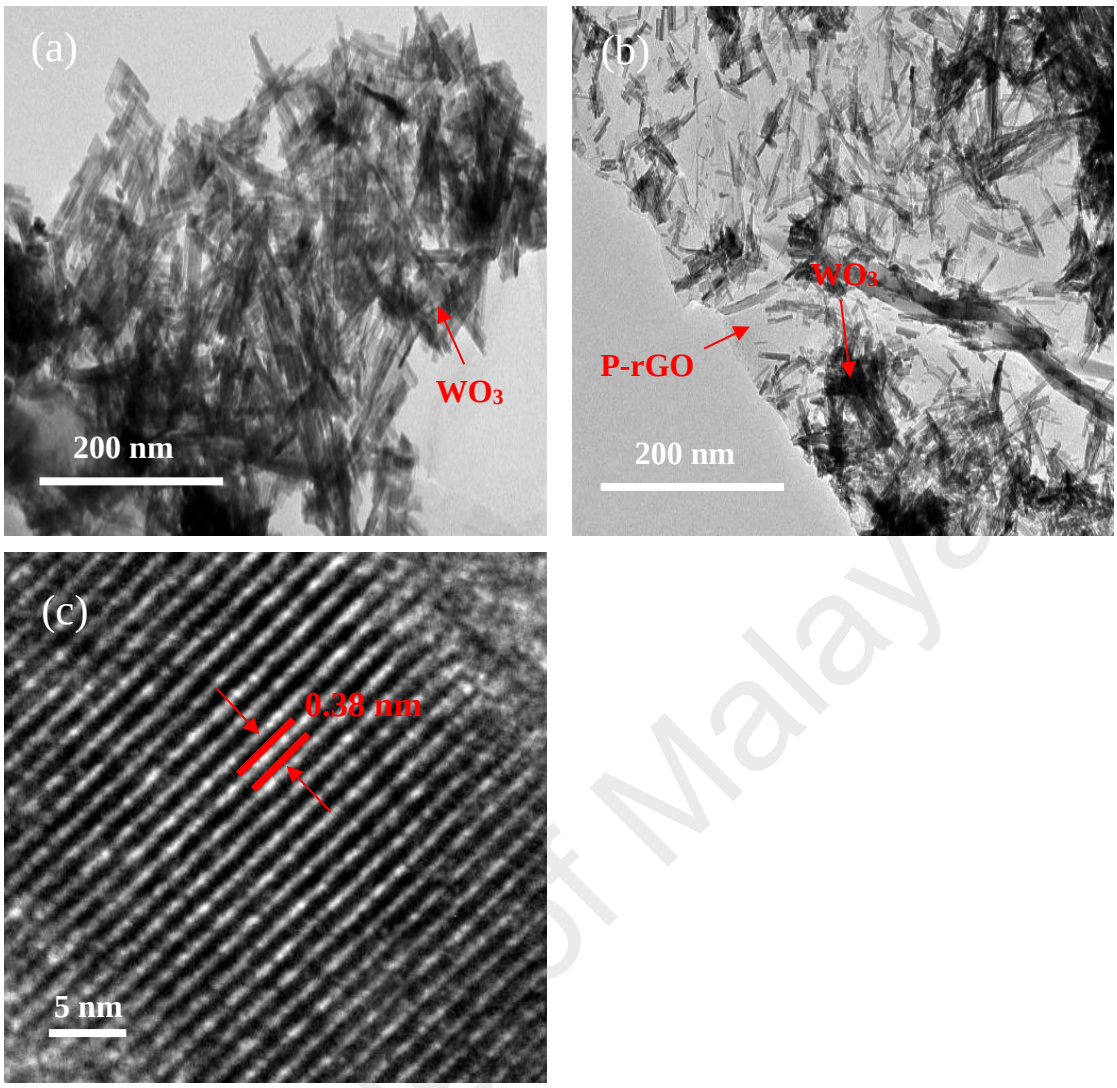

Figure 4.23: HRTEM images of (a) WO_3, (b) P-rGO/WO_3 nanocomposite and (c) EDX spectrum of P-rGO/WO_3 nanocomposite.

Figure 4.24 (a) reveals that the P-rGO/WO_3 nanocomposite has higher capacitance than that of WO_3 due to the larger area of CV loop (Ma et al., 2015). The result is in agreement with the specific capacitance values calculated from discharge curves in Figure 4.24 (b). The specific capacitances of P-rGO/WO_3 nanocomposite and WO_3 are calculated to be 274.0 and 108.0 F g^{-1}, respectively. The reason for improved electrochemical performance of P-rGO/WO_3 nanocomposite probably might be explained by the incorporation of high conductivity of P-rGO and fiber-like structure of WO_3, which increase the surface area and thus benefiting the interfacial contact between electrode-electrolyte (Mu et al., 2015). Among P-rGO, WO_3 and P-rGO/WO_3 nanocomposite, WO_3

demonstrates the lowest specific capacitance (108.0 F g^{-1}), which is probably associated with the low conductivity of WO_3 in nature. Furthermore, the discharge profile of P-rGO/WO_3 nanocomposite does not exhibit linear shape suggesting the total capacitance of composite is dominant contributed from pseudocapacitance. Pure WO_3 shows similar charge/discharge curve as composite. In contrast, the discharge curve of P-rGO (seen in Figure 4.4 (b)) exhibits symmetry triangular shape, revealing the absence of faradaic reaction process.

Figure 4.24 (c) compares the rate capabilities of P-rGO/WO_3 nanocomposite and WO_3 at different current densities. At current density of 0.3, 0.5, 0.7 and 1.0 A g^{-1}, the specific capacitance of P-rGO/WO_3 nanocomposite are 1360.9, 674.5, 274.0, and 70.7 F g^{-1}, respectively. Meanwhile, the specific capacitance of WO_3 are 462.2, 198.9, 108.0, and 28.1 F g^{-1} at similar current densities. The specific capacitance of P-rGO/WO_3 nanocomposite and WO_3 decreases with the increase of the charge/discharge current density. This may be attributed to the sulfite ions from electrolyte have sufficient time to penetrate into the reactive species at slow potential changes while only outer active surfaces are utilized at high potential (Karthikeyan et al., 2012).

The impedance of P-rGO/WO_3 nanocomposite and WO_3 are shown in Figure 4.24 (d). At high frequency region, the P-rGO/WO_3 nanocomposite electrode shows the smallest internal resistance of 6.92 Ω. While, the internal resistance of WO_3 electrode is almost 2 times higher than composite electrode, which is 12.30 Ω. The P-rGO/WO_3 nanocomposite electrode exhibits superior electrochemical performance, owing to the additional of P-rGO with high electronic conductivity which facilitate electron migration during charge/discharge process (Zhang et al., 2016b).

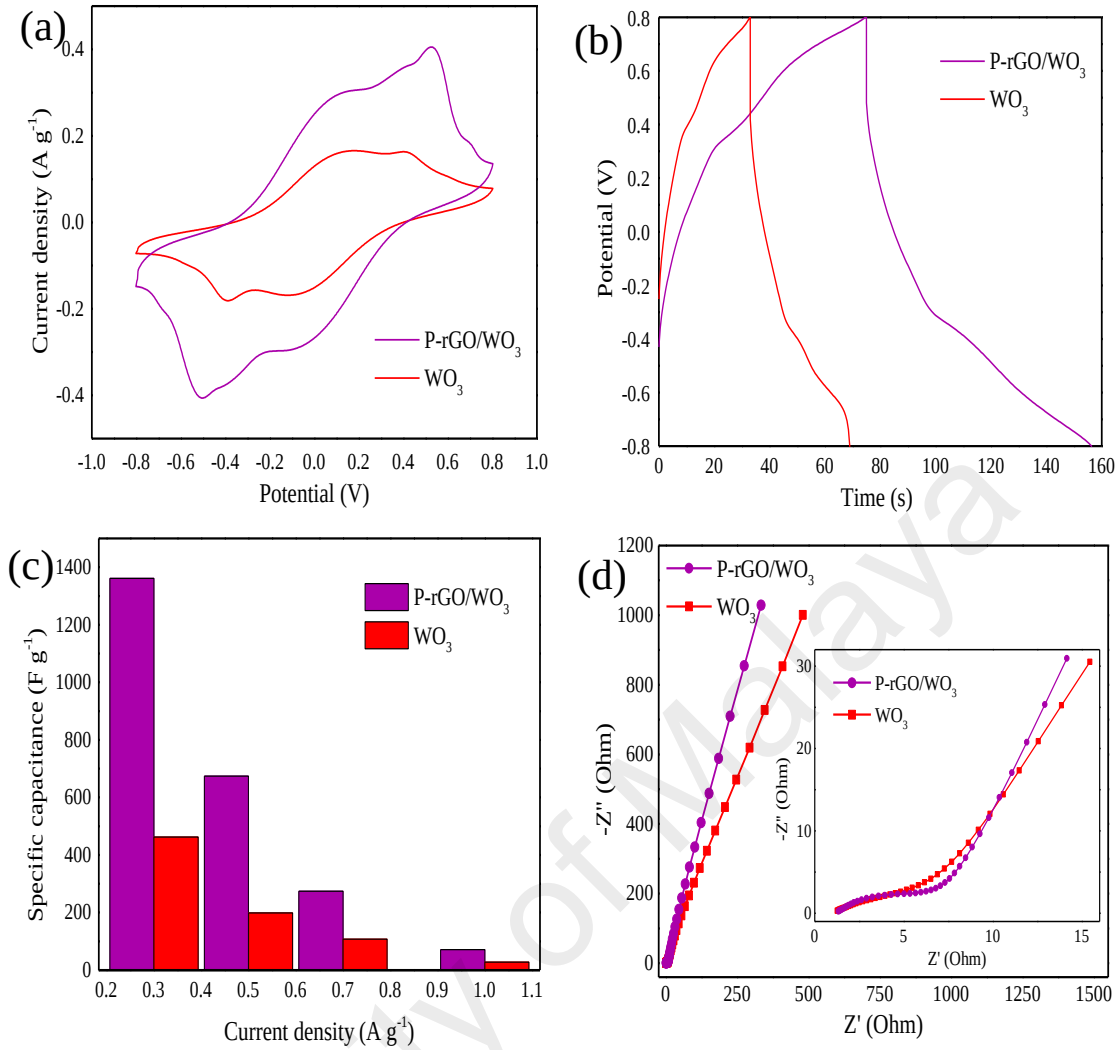

Figure 4.24: Comparison electrochemical performance of P-rGO/WO_3 nanocomposite and WO_3. (a) Cyclic voltammogram at scan rate of 25 mV s^{-1}; (b) Galvanostatic charge/discharge curves at current density of 0.7 A g^{-1}; (c) capacitance versus current densities; and (d) Nyquist plot of P-rGO/WO_3 nanocomposite and WO_3 at open circuit potential (OCP) (the inset of enlarged high frequency region).

Figure 4.25 (a) shows the Ragone plots of P-rGO/WO_3 nanocomposite and WO_3 at various current density (0.3, 0.5, 0.7 and 1 A g^{-1}), which calculated using Equations 3.4 and 3.5. The P-rGO/WO_3 nanocomposite exhibits the highest energy density of 121 Wh kg^{-1} at power density of 780.4 W kg^{-1}, which ascribed to its high specific capacitance and the use of neutral aqueous electrolyte with wider potential window. As the current density increased from 0.3 to 1 A g^{-1}, the power density increased from 780.4 W kg^{-1} to 1811 W kg^{-1}, but only 6.3 Wh kg^{-1} of energy density can still remain in supercapacitor. These results clearly show that the energy density decreases with

increasing in the current density, indicating only outer regions of electrode are used for charge storage at high discharge current (Xing et al., 2009). In contrast, WO_3 delivered a much lower energy density of 41.1 Wh kg^{-1} at power density of 666.2 W kg^{-1} due to its low specific capacitance (462.2 F g^{-1} at current density of 0.3 A g^{-1}) (Xiang et al., 2013).

Cycle stability is the most important requirement for practical applications. The stability of the optimized P-rGO/WO_3 nanocomposite was examined through galvanostatic charge/discharge test between -0.8 and 0.8 V at current density of 0.7 A g^{-1} and is depicted in Figure 4.25 (b). It can be seen that 75% of its initial specific capacitance remains even after 1000 cycles. This indicated that the nanocomposite shows excellent cycling stability. The good interaction between WO_3 and P-rGO provides a larger surface area for electrolyte access and the reversible capability provided by P-rGO.

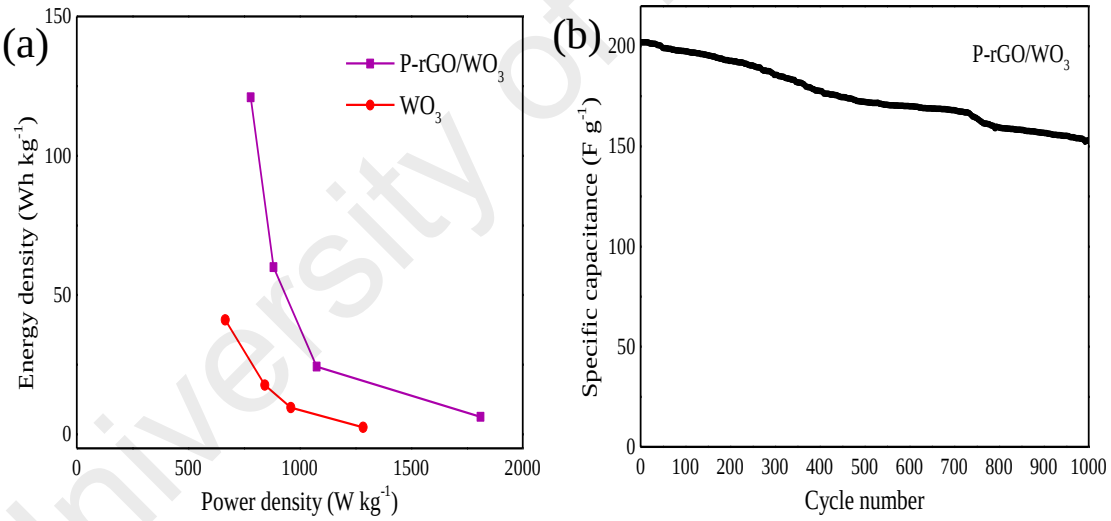

Figure 4.25: (a) Ragone plots of P-rGO/WO_3 nanocomposite and WO_3; and (b) Cycling performance of P-rGO/WO_3 nanocomposite at current density of 0.7 A g^{-1}.

4.5 Electrolytes

4.5.1 Types of neutral aqueous electrolyte

Besides electrodes, electrolyte also plays a vital role in determining the electrochemical performance of supercapacitor. Indeed, they influence the operating voltages range, power output and cycles life of supercapacitor. Neutral aqueous

electrolytes have the advantages of high ionic conductivity, high operating voltage (1-2 V) and low cost. Figure 4.26 displays the conductivity curve of electrolytes with different anions over the entire range of concentrations. It shows that the electrolytes conductivity increases with increasing the concentration until optimum values, which may attributed to the solubility of salt (Ruiz et al., 2012).

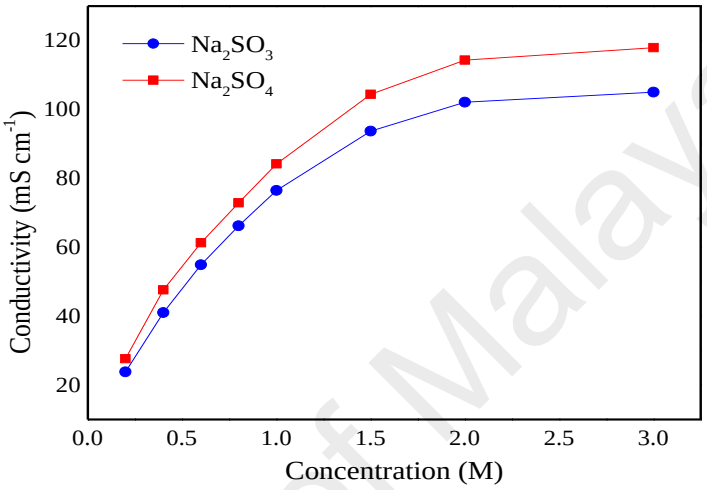

Figure 4.26: Ionic conductivity versus concentration of neutral aqueous electrolyte. Neutral aqueous electrolytes including Na_2SO_3 and Na_2SO_4.

From Figure 4.27 (a), the CV curves for P-rGO/WO_3 nanocomposite in 1M Na_2SO_3 and 1M Na_2SO_4 electrolyte demonstrate a non-ideal rectangular shape, implying the presence of pseudocapacitor behavior. Two pairs of redox peaks were observed for P-rGO/WO_3 nanocomposite electrode in Na_2SO_3 and Na_2SO_4 electrolyte corresponding to the reversible redox reaction of W^{6+}/W^{5+} and W^{5+}/W^{4+}. The anodic and cathodic peak of P-rGO/WO_3 electrode in Na_2SO_3 electrolyte were shown at 0.526 and -0.502 V, respectively. The anodic and cathodic peak of P-rGO/WO_3 electrode in Na_2SO_4 electrolyte were shown at 0.189 and -0.114 V, respectively. Na_2SO_4 electrolyte (1M = 84.2 mS cm^{-1}) possesses higher ionic conductivity compared with Na_2SO_3 (1M = 76.5 mS cm^{-1}), hence higher specific capacitance is expected. This fact is beneficial for electrochemical applications because high conductivity of electrolyte increases the ion mobility between the interface of electrode and electrolyte. However, Figure 4.27 (b)

shows the P-rGO/WO_3 electrode in Na_2SO_3 electrolyte have longer discharge time as compared to Na_2SO_4 electrolyte. In other words, the P-rGO/WO_3 electrode performed a better electrochemical properties in Na_2SO_3 than Na_2SO_4 electrolytes, as the obtained specific capacitance is 274 and 2.9 F g^{-1} at current density of 0.7 A g^{-1}, respectively. This results indicated that conductivity of electrolyte is not the only factor that influence the capacitive performance. The enhanced capacitance in Na_2SO_3 may attributed to the smaller ion size of SO_3^{2-} than SO_4^{2-}, which easy the penetration of ions into inner surface and that determine the overall capacitance. In order to further evidence the above results, the active sites occupied by the SO_3^{2-} and SO_4^{2-} ions are calculated using the following equation:

$$Z = (C_{sp}*\Delta V*MW)/F \qquad \text{(Equation 4.1)}$$

where C_{sp} is the specific capacitance, ΔV is operating potential window, MW is molecular weight of WO_3 (231.84 g mol^{-1}) and F is Faradaic constant (96485.33 s A mol^{-1}) (Maheswari and Muralidharan, 2015). Figure 4.27 (c-d) present the specific capacitance and active site versus current density in Na_2SO_3 and Na_2SO_4 electrolyte, respectively. It reveals that the SO_3^{2-} ions have the ability to diffuse into inner surface of the electrode leads to high number of active site. In contrast, only limited active site can be accessed by SO_4^{2-} ions even at low current density. Figure 4.27 (e) depicts Nyquist plot of P-rGO/WO_3 electrode in different electrolytes evaluated from the EIS experiments. A steeper vertical slope was observed for Na_2SO_3 than Na_2SO_4 electrolyte, suggesting Na_2SO_3 electrolyte exhibits low Warburg impedance at low frequency regions. These results are agreed well with the obtained charge/discharge curves. As shown in the enlarged spectra inset in Figure 4.27 (e), the R_{ct} value of Na_2SO_3 electrolyte is 6.92 **Ω** while the R_{ct} value obtained in Na_2SO_4 electrolyte is 4.82 **Ω**, suggesting the Na_2SO_4 electrolyte has higher conductivity than Na_2SO_3 electrolyte.

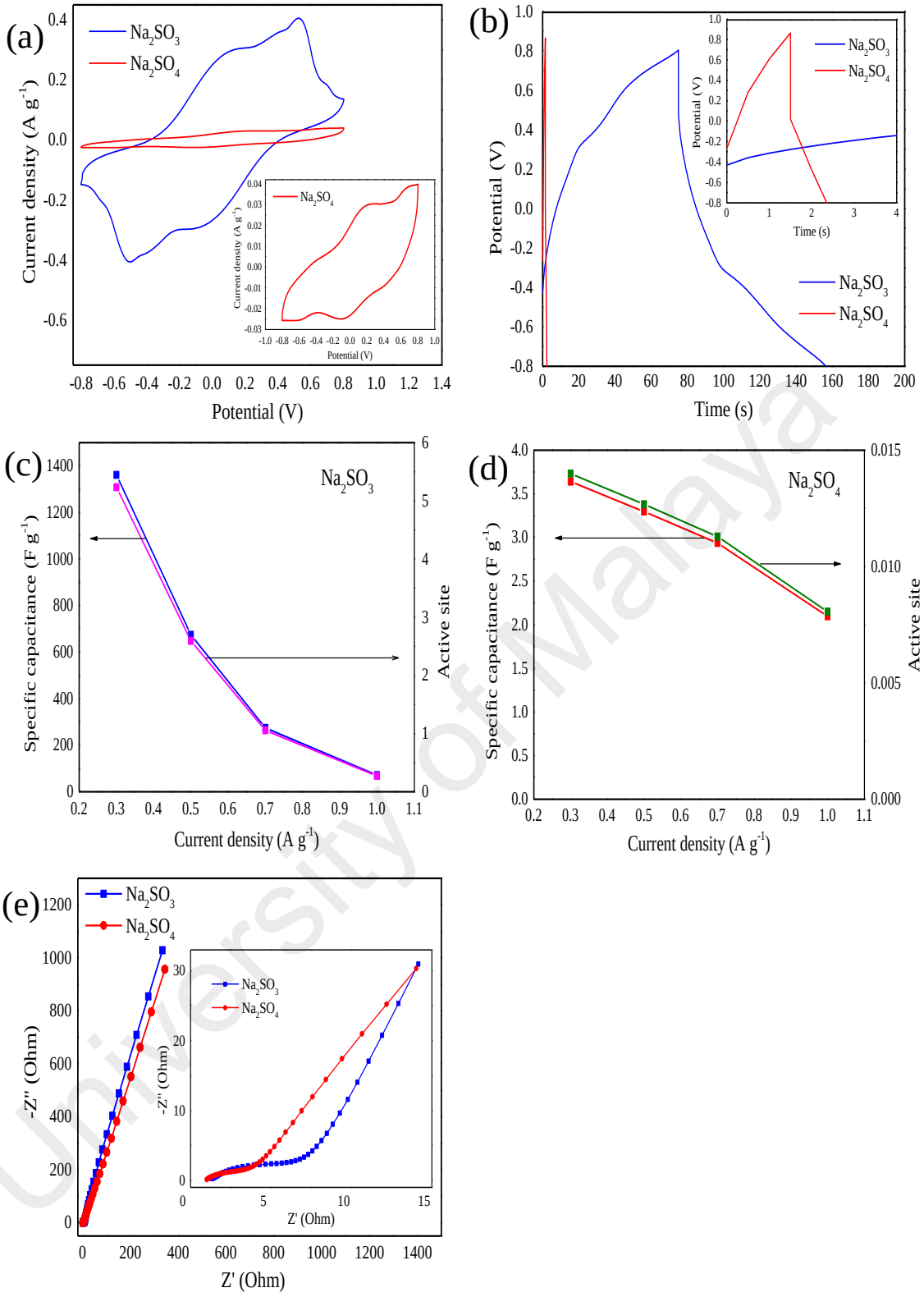

Figure 4.27: Comparison between Na_2SO_3 and Na_2SO_4 electrolyte. (a) Cyclic voltammogram of P-rGO/WO_3 nanocomposite at scan rate of 25 mV s^{-1}; (b) Galvanostatic charge/discharge curves at current density of 0.7 A g^{-1}; (c) Specific capacitance and active site vs. current density in Na_2SO_3 electrolyte; (d) Specific capacitance and active site vs. current density in Na_2SO_4 electrolyte; (e) Nyquist plot of P-rGO/WO_3 nanocomposite at OCP (the inset of enlarged high frequency region) for different electrolytes.

CHAPTER 5: CONCLUSION

5.1 Conclusion

In summary, the objectives of this research are well achieved. In the first stage of research study, the method that used to synthesis GO and rGO were determined. The conclusions attained in this part of research work was as following: (i) P-GO was successfully synthesized using two-steps modified Hummers' method. P-GO exhibited higher interlayer spacing and more oxygen functional groups were attached as compared to the GO that synthesized via a single-step modified Hummers' method. This high interlayer spacing easy the restoration of sp^2 structure during chemical reduction process, leadings to high diffusion rate of electrolyte ions; (ii) P-rGO and rGO were successfully synthesized using chemical reduction method. The prepared P-rGO exhibited higher capacitance as compared to rGO owing to its large number of aromatic domains. This restoration increased the conductivity of P-rGO. The obtained P-rGO was then adopted to synthesis P-rGO/WO_3 nanocomposite.

In order to further improve the capacitance of P-rGO, considerable effort has been conducted to improve the electrochemical performance by loading optimum content of APT (WO_3 precursor) using hydrothermal techniques. Interestingly, P-rGO/WO_3 nanocomposite with mass ratio of 1:100 showed the highest specific capacitance of 274 F g^{-1} under optimal conditions of 150 ºC and 20 h, give rise to 2-fold increment of specific capacitance over pure WO_3. A working voltage range of -0.8 to 0.8 V and high energy density of 121 Wh kg^{-1} at power density of 780.4 W kg^{-1} were obtained for P-rGO/WO_3 based symmetric cell. More significantly, P-rGO/WO_3 nanocomposite exhibited a good cycling performance and retained 75% of initial capacitance after 1000 cycles of galvanostatic charge/discharge. By carefully control the synthesis parameters (i.e., loadings of APT, temperature and reaction time), fiber-like structure of P-rGO/WO_3 nanocomposite was obtained and exhibited lower resistance due to fiber-like WO_3 acting

as the spacer to prevent the restacking of P-rGO as well as to provide a larger surface area for electrolyte access. Moreover, the addition of conductive P-rGO could decrease the resistance of ions between the electrolyte and electrode, leading to fast electron transport. A possible formation of WO_3 on P-rGO and WO_3 as an effective synergist is proposed. The present experimental works provide a better understanding on the role of fiber-like WO_3 in anchoring P-rGO/WO_3 nanocomposite for efficient electrochemical study.

Furthermore, the role of electrolyte in determining the electrochemical performance of P-rGO/WO_3 nanocomposites were evaluated using two different neutral electrolytes, namely 1 M Na_2SO_4 and 1 M Na_2SO_3. It is worthy to note that the P-rGO/WO_3 electrode performed better electrochemical properties in Na_2SO_3 than Na_2SO_4 electrolytes, as the obtained specific capacitance is 274 and 2.9 F g^{-1} at current density of 0.7 A g^{-1}, respectively. This excellent specific capacitance proved that Na_2SO_3 is more suitable used in this study owing to its small SO_3^{2-} ions.

As an overall remarks of this research work, it is concluded that the amount of WO_3 precursor, hydrothermal temperature and reaction time play an important role in developing a desired P-rGO/WO_3 electrode in order to further improve their electrochemical properties.

5.2 Recommendations for Future Research

In order to enhance the electrochemical performance of supercapacitors, several suggestions and recommendations should be noteworthy for future developments were proposed as follows:

1. Ternary composites have attracted great concern to improve the performance of devices due to the advantages of each component and the synergistic effect between them tends to eliminate the demerits of each other. In ternary composite,

conductive rGO acts as support to facilitate the nucleation and growth of metal oxide with well-defined structures and enhanced the electrical conductivity of composite. Metal oxide prevent the restacking of rGO leads to an increase of active sites for ions contact and contributing high pseudocapacitance. Conducting polymers possess high electrical conductivity and fast reversible electrochemical behavior. Thus, it can served as conductive additives to improve the interconnectivity within metal oxides and participate in contributing pseudocapacitance.

2. Widening the operating voltage of the cell by using non-aqueous electrolyte (mixture of ionic liquid and organic electrolyte) is an effective way to improve its energy and power density. High cell voltage can reduces the number of cells that used in series for high power system as well as increase the reliability of the devices. The ionic liquid electrolytes can be modified by adding an organic electrolyte to reduce the viscosity of ionic liquids such as acetonitrile and propylene carbonate. Ionic liquids can lower the vapor pressure of organic electrolytes and the high conductivity of acetonitrile is also able to enhance the conductivity of ionic liquids.

3. Designing a low cost supercapacitor is also one of the great challenge in which cost determines its use in most of the applications. Thus, energy-saving synthesis method without complicated system would be beneficial for design electrode materials. Recently, there are many reports on synthesis of nanomaterials using microwave-assisted hydrothermal methods, suggesting it requires only a short time to achieve uniform heating throughout the system. Moreover, the combination of microwave and conventional hydrothermal also possesses several advantages, including low temperature and pressure, low cost, high yield and morphology controllability.

REFERENCES

Adhikari, S., and Sarkar, D. (2014). Hydrothermal synthesis and electrochromism of WO_3 nanocuboids. *RSC Advances, 4*(39): 20145-20153.

Ahmad, M., Mokhtar, S., Soon, C., Nafarizal, N., Suriani, A., Mohamed, A., Mamat, M., Malek, M., Shimomura, M., and Murakami, K. (2016). Raman investigation of rutile-phased TiO_2. *Journal of Materials Science: Materials in Electronics*, 27(8): 7920-7926.

Akhavan, O. (2015). Bacteriorhodopsin as a superior substitute for hydrazine in chemical reduction of single-layer graphene oxide sheets. *Carbon, 81*: 158-166.

An, K. H., Kim, W. S., Park, Y. S., Moon, J. M., Bae, D. J., Lim, S. C., Lee, Y. S., and Lee, Y. H. (2001). Electrochemical properties of high-power supercapacitors using single-walled carbon nanotube electrodes. *Advanced Functional Materials, 11*(5): 387-392.

An, X., Jimmy, C. Y., Wang, Y., Hu, Y., Yu, X., and Zhang, G. (2012). WO_3 nanorods/graphene nanocomposites for high-efficiency visible-light-driven photocatalysis and NO_2 gas sensing. *Journal of Materials Chemistry, 22*(17): 8525-8531.

Azaïs, P., Duclaux, L., Florian, P., Massiot, D., Lillo-Rodenas, M. A., Linares-Solano, A., Peres, J. P., Jehoulet, C., and Béguin, F. (2007). Causes of supercapacitors ageing in organic electrolyte. *Journal of Power Sources, 171*(2): 1046-1053.

Bak, S. M., Nam, K. W., Lee, C. W., Kim, K. H., Jung, H. C., Yang, X. Q., and Kim, K. B. (2011). Spinel $LiMn_2O_4$/reduced graphene oxide hybrid for high rate lithium ion batteries. *Journal of Materials Chemistry, 21*(43): 17309-17315.

Balasubramaniam, M., and Balakumar, S. (2016). Exploration of electrochemical properties of zinc antimonate nanoparticles as supercapacitor electrode material. *Materials Science in Semiconductor Processing, 56*: 287-294.

Béguin, F., Presser, V., Balducci, A., and Frackowiak, E. (2014). Carbons and electrolytes for advanced supercapacitors. *Advanced Materials, 26*(14): 2219-2251.

Bianco, A., Cheng, H. M., Enoki, T., Gogotsi, Y., Hurt, R. H., Koratkar, N., Kyotani, T., Monthioux, M., Park, C. R., and Tascon, J. M. (2013). All in the graphene family–A recommended nomenclature for two-dimensional carbon materials. *Carbon, 65*: 1-6.

Birch, M. E., Ruda-Eberenz, T. A., Chai, M., Andrews, R., and Hatfield, R. L. (2013). Properties that influence the specific surface areas of carbon nanotubes and nanofibers. *Annals of Occupational Hygiene, 57*(9): 1148-1166.

Bo, Z., Wen, Z., Kim, H., Lu, G., Yu, K., and Chen, J. (2012). One-step fabrication and capacitive behavior of electrochemical double layer capacitor electrodes using vertically-oriented graphene directly grown on metal. *Carbon, 50*(12): 4379-4387.

Bonso, J. S., Rahy, A., Perera, S. D., Nour, N., Seitz, O., Chabal, Y. J., Balkus, K. J., Ferraris, J. P., and Yang, D. J. (2012). Exfoliated graphite nanoplatelets–V_2O_5 nanotube composite electrodes for supercapacitors. *Journal of Power Sources, 203*: 227-232.

Brousse, K., Huang, P., Pinaud, S., Respaud, M., Daffos, B., Chaudret, B., Lethien, C., Taberna, P., and Simon, P. (2016). Electrochemical behavior of high performance on-chip porous carbon films for micro-supercapacitors applications in organic electrolytes. *Journal of Power Sources, 328*: 520-526.

Burke, A. (2000). Ultracapacitors: why, how, and where is the technology. *Journal of Power Sources, 91*(1): 37-50.

Cai, Y., Wang, Y., Deng, S., Chen, G., Li, Q., Han, B., Han, R., and Wang, Y. (2014). Graphene nanosheets-tungsten oxides composite for supercapacitor electrode. *Ceramics International, 40*(3): 4109-4116.

Cao, N., and Zhang, Y. (2015). Study of reduced graphene oxide preparation by Hummers' method and related characterization. *Journal of Nanomaterials, 2015*: 2.

Chae, J. H., and Chen, G. Z. (2012). 1.9 V aqueous carbon–carbon supercapacitors with unequal electrode capacitances. *Electrochimica Acta, 86*: 248-254.

Chae, J. H., and Chen, G. Z. (2014). Influences of ions and temperature on performance of carbon nano-particulates in supercapacitors with neutral aqueous electrolytes. *Particuology, 15*: 9-17.

Chang, H. H., Chang, C. K., Tsai, Y. C., and Liao, C. S. (2012). Electrochemically synthesized graphene/polypyrrole composites and their use in supercapacitor. *Carbon, 50*(6): 2331-2336.

Chang, K. H., Hu, C. C., Huang, C. M., Liu, Y. L., and Chang, C. I. (2011). Microwave-assisted hydrothermal synthesis of crystalline WO_3–WO_3•$0.5H_2O$ mixtures for pseudocapacitors of the asymmetric type. *Journal of Power Sources, 196*(4): 2387-2392.

Chen, H., Zhou, S., and Wu, L. (2014). Porous nickel hydroxide–manganese dioxide-reduced graphene oxide ternary hybrid spheres as excellent supercapacitor electrode materials. *ACS Applied Materials & Interfaces, 6*(11): 8621-8630.

Chen, J., Li, W., Wang, D., Yang, S., Wen, J., and Ren, Z. (2002). Electrochemical characterization of carbon nanotubes as electrode in electrochemical double-layer capacitors. *Carbon, 40*(8): 1193-1197.

Chen, T., and Dai, L. (2013). Carbon nanomaterials for high-performance supercapacitors. *Materials Today, 16*(7): 272-280.

Chen, Y., Zhang, X., Zhang, D., Yu, P., and Ma, Y. (2011). High performance supercapacitors based on reduced graphene oxide in aqueous and ionic liquid electrolytes. *Carbon, 49*(2): 573-580.

Chen, Z., Peng, Y., Liu, F., Le, Z., Zhu, J., Shen, G., Zhang, D., Wen, M., Xiao, S., and Liu, C. P. (2015). Hierarchical nanostructured WO_3 with biomimetic proton channels and mixed ionic-electronic conductivity for electrochemical energy storage. *Nano Letters, 15*(10): 6802-6808.

Cheng, H., Long, L., Shu, D., Wu, J., Gong, Y., He, C., Kang, Z., and Zou, X. (2014). The supercapacitive behavior and excellent cycle stability of graphene/MnO_2 composite prepared by an electrostatic self-assembly process. *International Journal of Hydrogen Energy, 39*(28): 16151-16161.

Chowdhury, M. B., Sui, R., Lucky, R. A., and Charpentier, P. A. (2009). One-pot procedure to synthesize high surface area alumina nanofibers using supercritical carbon dioxide. *Langmuir, 26*(4): 2707-2713.

Chu, J., Lu, D., Wang, X., Wang, X., and Xiong, S. (2017). WO_3 nanoflower coated with graphene nanosheet: Synergetic energy storage composite electrode for supercapacitor application. *Journal of Alloys and Compounds, 702*: 568-572.

Chua, C. K., and Pumera, M. (2014). Chemical reduction of graphene oxide: a synthetic chemistry viewpoint. *Chemical Society Reviews, 43*(1): 291-312.

Conway, B. E. (1991). Transition from "supercapacitor" to "battery" behavior in electrochemical energy storage. *Journal of the Electrochemical Society, 138*(6): 1539-1548.

Davies, A., and Yu, A. (2011). Material advancements in supercapacitors: from activated carbon to carbon nanotube and graphene. *The Canadian Journal of Chemical Engineering, 89*(6): 1342-1357.

Elmouwahidi, A., Bailón-García, E., Pérez-Cadenas, A. F., Maldonado-Hódar, F. J., and Carrasco-Marín, F. (2017). Activated carbons from KOH and H_3PO_4-activation of olive residues and its application as supercapacitor electrodes. *Electrochimica Acta, 229*: 219-228.

Emiru, T. F., and Ayele, D. W. (2017). Controlled synthesis, characterization and reduction of graphene oxide: A convenient method for large scale production. *Egyptian Journal of Basic and Applied Sciences, 4*(1): 74-79.

Faraji, S., and Ani, F. N. (2014). Microwave-assisted synthesis of metal oxide/hydroxide composite electrodes for high power supercapacitors–A review. *Journal of Power Sources, 263*: 338-360.

Faraji, S., and Ani, F. N. (2015). The development supercapacitor from activated carbon by electroless plating—A review. *Renewable and Sustainable Energy Reviews, 42*: 823-834.

Farma, R., Deraman, M., Awitdrus, A., Talib, I., Taer, E., Basri, N., Manjunatha, J., Ishak, M., Dollah, B., and Hashmi, S. (2013). Preparation of highly porous binderless activated carbon electrodes from fibres of oil palm empty fruit bunches for application in supercapacitors. *Bioresource Technology, 132*: 254-261.

Feng, H., Hu, H., Dong, H., Xiao, Y., Cai, Y., Lei, B., Liu, Y., and Zheng, M. (2016). Hierarchical structured carbon derived from bagasse wastes: A simple and efficient synthesis route and its improved electrochemical properties for high-performance supercapacitors. *Journal of Power Sources, 302*: 164-173.

Fic, K., Meller, M., Menzel, J., and Frackowiak, E. (2016). Around the thermodynamic limitations of supercapacitors operating in aqueous electrolytes. *Electrochimica Acta, 206*: 496-503.

Frackowiak, E., Abbas, Q., and Béguin, F. (2013). Carbon/carbon supercapacitors. *Journal of Energy Chemistry, 22*(2): 226-240.

Fu, C., Kuang, Y., Huang, Z., Wang, X., Yin, Y., Chen, J., and Zhou, H. (2011). Supercapacitor based on graphene and ionic liquid electrolyte. *Journal of Solid State Electrochemistry, 15*(11-12): 2581-2585.

Gao, L., Wang, X., Xie, Z., Song, W., Wang, L., Wu, X., Qu, F., Chen, D., and Shen, G. (2013). High-performance energy-storage devices based on WO_3 nanowire arrays/carbon cloth integrated electrodes. *Journal of Materials Chemistry A, 1*(24): 7167-7173.

Gholipour-Ranjbar, H., Soleimani, M., and Naderi, H. R. (2016). Application of Ni/Co-based metal–organic frameworks (MOFs) as an advanced electrode material for supercapacitors. *New Journal of Chemistry, 40*(11): 9187-9193.

González, A., Goikolea, E., Barrena, J. A., and Mysyk, R. (2016). Review on supercapacitors: Technologies and materials. *Renewable and Sustainable Energy Reviews, 58*: 1189-1206.

Gu, Y., Zhuo, Q., and Wu, D. (2016). Large-mesopore hierarchical tungsten trioxide hydrate with exposed high energy facets: Facile synthesis and enhanced photocatalysis. *Materials Science in Semiconductor Processing, 53*: 18-27.

Gujar, T., Shinde, V., Lokhande, C., Kim, W. Y., Jung, K. D., and Joo, O. S. (2007). Spray deposited amorphous RuO_2 for an effective use in electrochemical supercapacitor. *Electrochemistry Communications, 9*(3): 504-510.

Guo, J., Li, Y., Zhu, S., Chen, Z., Liu, Q., Zhang, D., Moon, W. J., and Song, D. M. (2012). Synthesis of WO_3@ Graphene composite for enhanced photocatalytic oxygen evolution from water. *RSC Advances, 2*(4): 1356-1363.

Han, Y., Shen, N., Zhang, S., Li, D., and Li, X. (2017). Fish gill-derived activated carbon for supercapacitor application. *Journal of Alloys and Compounds, 694*: 636-642.

Huang, C. C., Xing, W., and Zhuo, S. P. (2009). Capacitive performances of amorphous tungsten oxide prepared by microwave irradiation. *Scripta Materialia, 61*(10): 985-987.

Huang, H., Yue, Z., Li, G., Wang, X., Huang, J., Du, Y., and Yang, P. (2013a). Ultraviolet-assisted preparation of mesoporous WO_3/reduced graphene oxide composites: superior interfacial contacts and enhanced photocatalysis. *Journal of Materials Chemistry A, 1*(47): 15110-15116.

Huang, K. J., Wang, L., Liu, Y. J., Liu, Y. M., Wang, H. B., Gan, T., and Wang, L. L. (2013b). Layered MoS_2–graphene composites for supercapacitor applications with enhanced capacitive performance. *International Journal of Hydrogen Energy, 38*(32): 14027-14034.

Huang, K., Pan, Q., Yang, F., Ni, S., Wei, X., and He, D. (2008). Controllable synthesis of hexagonal WO_3 nanostructures and their application in lithium batteries. *Journal of Physics D: Applied Physics, 41*(15): 155417.

Huang, R., Shen, Y., Zhao, L., and Yan, M. (2012). Effect of hydrothermal temperature on structure and photochromic properties of WO_3 powder. *Advanced Powder Technology, 23*(2): 211-214.

Huo, N., Yang, S., Wei, Z., and Li, J. (2013). Synthesis of WO_3 nanostructures and their ultraviolet photoresponse properties. *Journal of Materials Chemistry C, 1*(25): 3999-4007.

Iwu, K. O., Galeckas, A., Rauwel, P., Kuznetsov, A. Y., and Norby, T. (2012). One-dimensional WO_3 and its hydrate: One-step synthesis, structural and spectroscopic characterization. *Journal of Solid State Chemistry, 185*: 245-252.

Jayalakshmi, M., and Balasubramanian, K. (2008). Simple capacitors to supercapacitors-An overview. *International Journal Electrochemical Science, 3*(11): 1196-1217.

Jie, X., Zeng, D., Zhang, J., Xu, K., Wu, J., Zhu, B., and Xie, C. (2015). Graphene-wrapped WO_3 nanospheres with room-temperature NO_2 sensing induced by interface charge transfer. *Sensors and Actuators B: Chemical, 220*: 201-209.

Jo, C., Hwang, J., Song, H., Dao, A. H., Kim, Y. T., Lee, S. H., Hong, S. W., Yoon, S., and Lee, J. (2013). Block‐Copolymer‐Assisted One‐Pot Synthesis of Ordered Mesoporous WO_{3-x}/Carbon Nanocomposites as High‐Rate‐Performance Electrodes for Pseudocapacitors. *Advanced Functional Materials, 23*(30): 3747-3754.

Jo, E. H., Choi, J. H., Park, S. R., Lee, C. M., Chang, H., and Jang, H. D. (2016). Size and structural effect of crumpled graphene balls on the electrochemical properties for supercapacitor application. *Electrochimica Acta, 222*: 58-63.

Kalambate, P. K., Dar, R. A., Karna, S. P., and Srivastava, A. K. (2015). High performance supercapacitor based on graphene-silver nanoparticles-polypyrrole nanocomposite coated on glassy carbon electrode. *Journal of Power Sources, 276*: 262-270.

Kalanur, S. S., Hwang, Y. J., Chae, S. Y., and Joo, O. S. (2013). Facile growth of aligned WO_3 nanorods on FTO substrate for enhanced photoanodic water oxidation activity. *Journal of Materials Chemistry A, 1*(10): 3479-3488.

Karthikeyan, K., Kalpana, D., Amaresh, S., and Lee, Y. S. (2012). Microwave synthesis of graphene/magnetite composite electrode material for symmetric supercapacitor with superior rate performance. *RSC Advances, 2*(32): 12322-12328.

Khomenko, V., Raymundo-Pinero, E., and Béguin, F. (2006). Optimisation of an asymmetric manganese oxide/activated carbon capacitor working at 2 V in aqueous medium. *Journal of Power Sources, 153*(1): 183-190.

Kim, J. H., Nam, K. W., Ma, S. B., and Kim, K. B. (2006). Fabrication and electrochemical properties of carbon nanotube film electrodes. *Carbon, 44*(10): 1963-1968.

Kim, K. H., Yang, M., Cho, K. M., Jun, Y. S., Lee, S. B., and Jung, H. T. (2013). High quality reduced graphene oxide through repairing with multi-layered graphene ball nanostructures. *Scientific Reports, 3*.

Kovtyukhova, N. I., Ollivier, P. J., Martin, B. R., Mallouk, T. E., Chizhik, S. A., Buzaneva, E. V., and Gorchinskiy, A. D. (1999). Layer-by-layer assembly of ultrathin composite films from micron-sized graphite oxide sheets and polycations. *Chemistry of Materials, 11*(3): 771-778.

Lei, Z., Liu, Z., Wang, H., Sun, X., Lu, L., and Zhao, X. (2013). A high-energy-density supercapacitor with graphene–CMK-5 as the electrode and ionic liquid as the electrolyte. *Journal of Materials Chemistry A, 1*(6): 2313-2321.

Li, W., Chen, J., Zhao, J., Zhang, J., and Zhu, J. (2005). Application of ultrasonic irradiation in preparing conducting polymer as active materials for supercapacitor. *Materials Letters, 59*(7): 800-803.

Li, X., Wang, G., Wang, X., Li, X., and Ji, J. (2013). Flexible supercapacitor based on MnO_2 nanoparticles via electrospinning. *Journal of Materials Chemistry A, 1*(35): 10103-10106.

Liang, C. L., Liu, Y., Bao, R. Y., Luo, Y., Yang, W., Xie, B. H., and Yang, M. B. (2016). Effects of Fe_3O_4 loading on the cycling performance of Fe_3O_4/rGO composite anode material for lithium ion batteries. *Journal of Alloys and Compounds, 678*: 80-86.

Liang, L., Zhang, J., Zhou, Y., Xie, J., Zhang, X., Guan, M., Pan, B., and Xie, Y. (2013). High-performance flexible electrochromic device based on facile semiconductor-to-metal transition realized by $WO_3 \bullet 2H_2O$ ultrathin nanosheets. *Scientific Reports, 3*.

Liew, C. W., Ramesh, S., and Arof, A. (2016). Investigation of ionic liquid-doped ion conducting polymer electrolytes for carbon-based electric double layer capacitors (EDLCs). *Materials & Design, 92*: 829-835.

Lin, R., Taberna, P. L., Fantini, S., Presser, V., Pérez, C. R., Malbosc, F., Rupesinghe, N. L., Teo, K. B., Gogotsi, Y., and Simon, P. (2011). Capacitive energy storage from − 50 to 100 ºC using an ionic liquid electrolyte. *The Journal of Physical Chemistry Letters, 2*(19): 2396-2401.

Liu, C., Yu, Z., Neff, D., Zhamu, A., and Jang, B. Z. (2010). Graphene-based supercapacitor with an ultrahigh energy density. *Nano Letters, 10*(12): 4863-4868.

Liu, R., Cho, S. I., and Lee, S. B. (2008). Poly (3, 4-ethylenedioxythiophene) nanotubes as electrode materials for a high-powered supercapacitor. *Nanotechnology, 19*(21): 215710.

Lu, T., Zhang, Y., Li, H., Pan, L., Li, Y., and Sun, Z. (2010). Electrochemical behaviors of graphene–ZnO and graphene–SnO_2 composite films for supercapacitors. *Electrochimica Acta, 55*(13): 4170-4173.

Lukatskaya, M. R., Dunn, B., and Gogotsi, Y. (2016). Multidimensional materials and device architectures for future hybrid energy storage. *Nature Communications, 7*.

Ma, L., Zhou, X., Xu, L., Xu, X., Zhang, L., Ye, C., Luo, J., and Chen, W. (2015). Hydrothermal preparation and supercapacitive performance of flower-like WO_3•H_2O/reduced graphene oxide composite. *Colloids and Surfaces A: Physicochemical and Engineering Aspects, 481*: 609-615.

Maheswari, N., and Muralidharan, G. (2015). Supercapacitor behavior of cerium oxide nanoparticles in neutral aqueous electrolytes. *Energy & Fuels, 29*(12): 8246-8253.

Masoumi, M. M., and Naderinezhad, S. (2014). One of two conductors in capacitor substitute by Mercury. *Bonfring International Journal of Power Systems and Integrated Circuits, 4*(1): 1.

Mirghni, A. A., Madito, M. J., Masikhwa, T. M., Oyedotun, K. O., Bello, A., and Manyala, N. (2017). Hydrothermal synthesis of manganese phosphate/graphene foam composite for electrochemical supercapacitor applications. *Journal of Colloid and Interface Science, 494*: 325-337.

Mishra, A. K., and Ramaprabhu, S. (2011). Functionalized graphene-based nanocomposites for supercapacitor application. *The Journal of Physical Chemistry C, 115*(29): 14006-14013.

Mu, B., Zhang, W., Xu, W., and Wang, A. (2015). Hollowed-out tubular carbon@ MnO_2 hybrid composites with controlled morphology derived from kapok fibers for supercapacitor electrode materials. *Electrochimica Acta, 178*: 709-720.

Ou, J. Z., Balendhran, S., Field, M. R., McCulloch, D. G., Zoolfakar, A. S., Rani, R. A., Zhuiykov, S., O'Mullane, A. P., and Kalantar-zadeh, K. (2012). The anodized crystalline WO_3 nanoporous network with enhanced electrochromic properties. *Nanoscale, 4*(19): 5980-5988.

Pang, H., Gao, F., Chen, Q., Liu, R., and Lu, Q. (2012). Dendrite-like Co_3O_4 nanostructure and its applications in sensors, supercapacitors and catalysis. *Dalton Transactions, 41*(19): 5862-5868.

Pang, L., Zou, B., Zou, Y., Han, X., Cao, L., Wang, W., and Guo, Y. (2016). A new route for the fabrication of corn starch-based porous carbon as electrochemical supercapacitor electrode material. *Colloids and Surfaces A: Physicochemical and Engineering Aspects, 504*: 26-33.

Park, S., An, J., Potts, J. R., Velamakanni, A., Murali, S., and Ruoff, R. S. (2011). Hydrazine-reduction of graphite-and graphene oxide. *Carbon, 49*(9): 3019-3023.

Peng, C., Yan, X. B., Wang, R. T., Lang, J. W., Ou, Y. J., and Xue, Q. J. (2013). Promising activated carbons derived from waste tea-leaves and their application in high performance supercapacitors electrodes. *Electrochimica Acta, 87*: 401-408.

Peng, H., Ma, G., Sun, K., Mu, J., Luo, M., and Lei, Z. (2014). High-performance aqueous asymmetric supercapacitor based on carbon nanofibers network and tungsten trioxide nanorod bundles electrodes. *Electrochimica Acta, 147*: 54-61.

Peng, X. Y., Liu, X. X., Diamond, D., and Lau, K. T. (2011). Synthesis of electrochemically-reduced graphene oxide film with controllable size and thickness and its use in supercapacitor. *Carbon, 49*(11): 3488-3496.

Perera, S. D., Mariano, R. G., Nijem, N., Chabal, Y., Ferraris, J. P., and Balkus, K. J. (2012). Alkaline deoxygenated graphene oxide for supercapacitor applications: An effective green alternative for chemically reduced graphene. *Journal of Power Sources, 215*: 1-10.

Phiri, J., Gane, P., and Maloney, T. C. (2017). General overview of graphene: Production, properties and application in polymer composites. *Materials Science and Engineering: B, 215*: 9-28.

Rajagopal, S., Nataraj, D., Mangalaraj, D., Djaoued, Y., Robichaud, J., and Khyzhun, O. Y. (2009). Controlled growth of WO_3 nanostructures with three different morphologies and their structural, optical, and photodecomposition studies. *Nanoscale Research Letters, 4*(11): 1335.

Rakhi, R., Nagaraju, D., Beaujuge, P., and Alshareef, H. N. (2016). Supercapacitors based on two dimensional VO_2 nanosheet electrodes in organic gel electrolyte. *Electrochimica Acta, 220*: 601-608.

Ren, S., Wang, M., Xu, M., Yang, Y., Jia, C., and Hao, C. (2014). Fabrication of high-performance supercapacitors based on hollow SnO_2 microspheres. *Journal of Solid State Electrochemistry, 18*(4): 909-916.

Roberts, M. E., Wheeler, D. R., McKenzie, B. B., and Bunker, B. C. (2009). High specific capacitance conducting polymer supercapacitor electrodes based on poly (tris (thiophenylphenyl) amine). *Journal of Materials Chemistry, 19*(38): 6977-6979.

Ruiz, V., Huynh, T., Sivakkumar, S., and Pandolfo, A. (2012). Ionic liquid–solvent mixtures as supercapacitor electrolytes for extreme temperature operation. *RSC Advances, 2*(13): 5591-5598.

Rusi, S. (2015). Green synthesis of in situ electrodeposited rGO/MnO_2 nanocomposite for high energy density supercapacitors. *Scientific Reports, 5*.

Sadhukhan, S., Ghosh, T. K., Rana, D., Roy, I., Bhattacharyya, A., Sarkar, G., Chakraborty, M., and Chattopadhyay, D. (2016). Studies on synthesis of reduced graphene oxide (RGO) via green route and its electrical property. *Materials Research Bulletin, 79*: 41-51.

Sahu, V., Goel, S., Sharma, R. K., and Singh, G. (2015). Zinc oxide nanoring embedded lacey graphene nanoribbons in symmetric/asymmetric electrochemical capacitive energy storage. *Nanoscale, 7*(48): 20642-20651.

Samdani, J., Samdani, K., Kim, N. H., and Lee, J. H. (2017). A new protocol for the distribution of MnO_2 nanoparticles on rGO sheets and the resulting electrochemical performance. *Applied Surface Science, 399*: 95-105.

Sankar, K. V., and Selvan, R. K. (2014). The preparation of $MnFe_2O_4$ decorated flexible graphene wrapped with PANI and its electrochemical performances for hybrid supercapacitors. *RSC Advances, 4*(34): 17555-17566.

Satheesh, K., and Jayavel, R. (2013). Synthesis and electrochemical properties of reduced graphene oxide via chemical reduction using thiourea as a reducing agent. *Materials Letters, 113*: 5-8.

Shao, Y., Wang, J., Engelhard, M., Wang, C., and Lin, Y. (2010). Facile and controllable electrochemical reduction of graphene oxide and its applications. *Journal of Materials Chemistry, 20*(4): 743-748.

Sharma, P., and Bhatti, T. (2010). A review on electrochemical double-layer capacitors. *Energy Conversion and Management, 51*(12): 2901-2912.

Shi, J., Cheng, Z., Gao, L., Zhang, Y., Xu, J., and Zhao, H. (2016). Facile synthesis of reduced graphene oxide/hexagonal WO_3 nanosheets composites with enhanced H_2S sensing properties. *Sensors and Actuators B: Chemical, 230*: 736-745.

Shinde, N. M., Jagadale, A. D., Kumbhar, V. S., Rana, T. R., Kim, J., and Lokhande, C. D. (2015). Wet chemical synthesis of WO_3 thin films for supercapacitor application. *Korean Journal of Chemical Engineering, 32*(5): 974-979.

Shivakumara, S., Kishore, B., Penki, T. R., and Munichandraiah, N. (2014a). Symmetric supercapacitor based on partially exfoliated and reduced graphite oxide in neutral aqueous electrolyte. *Solid State Communications, 199*: 26-32.

Shivakumara, S., Penki, T. R., and Munichandraiah, N. (2014b). Preparation and electrochemical performance of porous hematite (α-Fe_2O_3) nanostructures as supercapacitor electrode material. *Journal of Solid State Electrochemistry, 18*(4): 1057-1066.

Sk, M. M., Yue, C. Y., Ghosh, K., and Jena, R. K. (2016). Review on advances in porous nanostructured nickel oxides and their composite electrodes for high-performance supercapacitors. *Journal of Power Sources, 308*: 121-140.

Song, Z., Liu, W., Wei, W., Quan, C., Sun, N., Zhou, Q., Liu, G., and Wen, X. (2016). Preparation and electrochemical properties of Fe_2O_3/reduced graphene oxide aerogel (Fe_2O_3/rGOA) composites for supercapacitors. *Journal of Alloys and Compounds, 685*: 355-363.

Staaf, L., Lundgren, P., and Enoksson, P. (2014). Present and future supercapacitor carbon electrode materials for improved energy storage used in intelligent wireless sensor systems. *Nano Energy, 9*: 128-141.

Stankovich, S., Dikin, D. A., Piner, R. D., Kohlhaas, K. A., Kleinhammes, A., Jia, Y., Wu, Y., Nguyen, S. T., and Ruoff, R. S. (2007). Synthesis of graphene-based nanosheets via chemical reduction of exfoliated graphite oxide. *Carbon, 45*(7): 1558-1565.

Stoller, M. D., Park, S., Zhu, Y., An, J., and Ruoff, R. S. (2008). Graphene-based ultracapacitors. *Nano Letters, 8*(10): 3498-3502.

Su, X., Li, Y., Jian, J., and Wang, J. (2010). In situ etching WO_3 nanoplates: hydrothermal synthesis, photoluminescence and gas sensor properties. *Materials Research Bulletin, 45*(12): 1960-1963.

Suleman, M., Kumar, Y., and Hashmi, S. (2015). High-rate supercapacitive performance of GO/r-GO electrodes interfaced with plastic-crystal-based flexible gel polymer electrolyte. *Electrochimica Acta, 182*: 995-1007.

Sun, W., Yeung, M. T., Lech, A. T., Lin, C. W., Lee, C., Li, T., Duan, X., Zhou, J., and Kaner, R. B. (2015). High surface area tunnels in hexagonal WO_3. *Nano Letters, 15*(7): 4834-4838.

Taer, E., Deraman, M., Talib, I. A., Umar, A. A., Oyama, M., and Yunus, R. M. (2010). Physical, electrochemical and supercapacitive properties of activated carbon pellets from pre-carbonized rubber wood sawdust by CO_2 activation. *Current Applied Physics, 10*(4): 1071-1075.

Tang, L., Wang, Y., Li, Y., Feng, H., Lu, J., and Li, J. (2009). Preparation, structure, and electrochemical properties of reduced graphene sheet films. *Advanced Functional Materials, 19*(17): 2782-2789.

Tian, X., Zhao, N., Song, Y., Wang, K., Xu, D., Li, X., Guo, Q., and Liu, L. (2015). Synthesis of nitrogen-doped electrospun carbon nanofibers with superior performance as efficient supercapacitor electrodes in alkaline solution. *Electrochimica Acta, 185*: 40-51.

Tsai, W. Y., Lin, R., Murali, S., Zhang, L. L., McDonough, J. K., Ruoff, R. S., Taberna, P. L., Gogotsi, Y., and Simon, P. (2013). Outstanding performance of activated graphene based supercapacitors in ionic liquid electrolyte from − 50 to 80 ºC. *Nano Energy, 2*(3): 403-411.

Wang, G., Zhang, L., and Zhang, J. (2012). A review of electrode materials for electrochemical supercapacitors. *Chemical Society Reviews, 41*(2): 797-828.

Wang, H., Tian, H., Wang, X., Qiao, L., Wang, S., Wang, X., Zheng, W., and Liu, Y. (2011). Electrical conductivity of alkaline-reduced graphene oxide. *Chemical Research Chinese Universities, 27*(5): 857-861.

Wang, K., Huang, J., and Wei, Z. (2010). Conducting polyaniline nanowire arrays for high performance supercapacitors. *The Journal of Physical Chemistry C, 114*(17): 8062-8067.

Wang, P., Wang, J., Wang, X., Yu, H., Yu, J., Lei, M., and Wang, Y. (2013). One-step synthesis of easy-recycling TiO_2-rGO nanocomposite photocatalysts with enhanced photocatalytic activity. *Applied Catalysis B: Environmental, 132*: 452-459.

Wang, Q., Jiao, L., Du, H., Wang, Y., and Yuan, H. (2014a). Fe_3O_4 nanoparticles grown on graphene as advanced electrode materials for supercapacitors. *Journal of Power Sources, 245*: 101-106.

Wang, Q., Qiu, S., Wang, S., Shang, J., Zhao, R., Wu, X., Chen, W., Zhou, H., and Wang, X. (2015a). Graphene oxide/polyaniline nanotube composites synthesized in alkaline aqueous solution. *Synthetic Metals, 210*: 314-322.

Wang, Y. H., Wang, C. C., Cheng, W. Y., and Lu, S. Y. (2014b). Dispersing WO_3 in carbon aerogel makes an outstanding supercapacitor electrode material. *Carbon, 69*: 287-293.

Wang, Y., Shi, Z., Huang, Y., Ma, Y., Wang, C., Chen, M., and Chen, Y. (2009). Supercapacitor devices based on graphene materials. *The Journal of Physical Chemistry. C, Nanomaterials and Interfaces, 113*(30): 13103.

Wang, Y., Yang, R., Li, M., and Zhao, Z. (2015b). Hydrothermal preparation of highly porous carbon spheres from hemp (Cannabis sativa L.) stem hemicellulose for use in energy-related applications. *Industrial Crops and Products, 65*: 216-226.

Xia, H., Meng, Y. S., Yuan, G., Cui, C., and Lu, L. (2012). A symmetric RuO_2/RuO_2 supercapacitor operating at 1.6 V by using a neutral aqueous electrolyte. *Electrochemical and Solid-State Letters, 15*(4): A60-A63.

Xia, X. H., Tu, J. P., Mai, Y. J., Wang, X. L., Gu, C. D., and Zhao, X. B. (2011). Self-supported hydrothermal synthesized hollow Co_3O_4 nanowire arrays with high supercapacitor capacitance. *Journal of Materials Chemistry, 21*(25): 9319-9325.

Xiang, C., Li, M., Zhi, M., Manivannan, A., and Wu, N. (2013). A reduced graphene oxide/Co_3O_4 composite for supercapacitor electrode. *Journal of Power Sources, 226*: 65-70.

Xie, Q., Bao, R., Xie, C., Zheng, A., Wu, S., Zhang, Y., Zhang, R., and Zhao, P. (2016). Core-shell N-doped active carbon fiber@ graphene composites for aqueous symmetric supercapacitors with high-energy and high-power density. *Journal of Power Sources, 317*: 133-142.

Xing, L. L., Huang, K. J., and Fang, L. X. (2016). Preparation of layered graphene and tungsten oxide hybrids for enhanced performance supercapacitors. *Dalton Transactions, 45*(43): 17439-17446.

Xing, W., Huang, C., Zhuo, S., Yuan, X., Wang, G., Hulicova-Jurcakova, D., Yan, Z., and Lu, G. (2009). Hierarchical porous carbons with high performance for supercapacitor electrodes. *Carbon, 47*(7): 1715-1722.

Xu, J., Ding, T., Wang, J., Zhang, J., Wang, S., Chen, C., Fang, Y., Wu, Z., Huo, K., and Dai, J. (2015). Tungsten oxide nanofibers self-assembled mesoscopic microspheres as high-performance electrodes for supercapacitor. *Electrochimica Acta, 174*: 728-734.

Xu, J., Ju, Z., Cao, J., Wang, W., Wang, C., and Chen, Z. (2016). Microwave synthesis of nitrogen-doped mesoporous carbon/nickel-cobalt hydroxide microspheres for high-performance supercapacitors. *Journal of Alloys and Compounds, 689*: 489-499.

Yan, J., Fan, Z., Sun, W., Ning, G., Wei, T., Zhang, Q., Zhang, R., Zhi, L., and Wei, F. (2012). Advanced asymmetric supercapacitors based on $Ni(OH)_2$/graphene and porous graphene electrodes with high energy density. *Advanced Functional Materials, 22*(12): 2632-2641.

Yang, C.-S., Jang, Y. S., and Jeong, H. K. (2014). Bamboo-based activated carbon for supercapacitor applications. *Current Applied Physics, 14*(12): 1616-1620.

Yang, J., Jiao, L., Zhao, Q., Wang, Q., Gao, H., Huan, Q., Zheng, W., Wang, Y., and Yuan, H. (2012). Facile preparation and electrochemical properties of hierarchical chrysanthemum-like WO_3•$0.33H_2O$. *Journal of Materials Chemistry, 22*(9): 3699-3701.

Yang, J., Yuan, Y., Wang, W., Tang, H., Ye, Z., and Lu, J. (2017). Interconnected $Co_{0.85}Se$ nanosheets as cathode materials for asymmetric supercapacitors. *Journal of Power Sources, 340*: 6-13.

Yang, Q., Lu, Z., Liu, J., Lei, X., Chang, Z., Luo, L., and Sun, X. (2013). Metal oxide and hydroxide nanoarrays: Hydrothermal synthesis and applications as supercapacitors and nanocatalysts. *Progress in Natural Science: Materials International, 23*(4): 351-366.

Yao, S., Zheng, X., Zhang, X., Xiao, H., Qu, F., and Wu, X. (2017). Facile synthesis of flexible WO_3 nanofibers as supercapacitor electrodes. *Materials Letters, 186*: 94-97.

Yaqoob, U., Uddin, A. I., and Chung, G.-S. (2016). A high-performance flexible NO_2 sensor based on WO_3 NPs decorated on MWCNTs and RGO hybrids on PI/PET substrates. *Sensors and Actuators B: Chemical, 224*: 738-746.

Yoon, S., Kang, E., Kim, J. K., Lee, C. W., and Lee, J. (2011). Development of high-performance supercapacitor electrodes using novel ordered mesoporous tungsten oxide materials with high electrical conductivity. *Chemical Communications, 47*(3): 1021-1023.

Yu, A., Roes, I., Davies, A., and Chen, Z. (2010). Ultrathin, transparent, and flexible graphene films for supercapacitor application. *Applied Physics Letters, 96*(25): 253105.

Yu, G., Xie, X., Pan, L., Bao, Z., and Cui, Y. (2013). Hybrid nanostructured materials for high-performance electrochemical capacitors. *Nano Energy, 2*(2): 213-234.

Zainy, M., Huang, N., Kumar, S. V., Lim, H., Chia, C. H., and Harrison, I. (2012). Simple and scalable preparation of reduced graphene oxide–silver nanocomposites via rapid thermal treatment. *Materials Letters, 89*: 180-183.

Zhai, T., Wang, F., Yu, M., Xie, S., Liang, C., Li, C., Xiao, F., Tang, R., Wu, Q., and Lu, X. (2013). 3D MnO_2–graphene composites with large areal capacitance for high-performance asymmetric supercapacitors. *Nanoscale*, *5*(15): 6790-6796.

Zhang, H. B., Wang, J. W., Yan, Q., Zheng, W. G., Chen, C., and Yu, Z. Z. (2011). Vacuum-assisted synthesis of graphene from thermal exfoliation and reduction of graphite oxide. *Journal of Materials Chemistry, 21*(14): 5392-5397.

Zhang, H., Liu, Z., Yang, J., Guo, W., Zhu, L., and Zheng, W. (2014). Temperature and acidity effects on WO_3 nanostructures and gas-sensing properties of WO_3 nanoplates. *Materials Research Bulletin, 57*: 260-267.

Zhang, H., Zhang, L., Chen, J., Su, H., Liu, F., and Yang, W. (2016a). One-step synthesis of hierarchically porous carbons for high-performance electric double layer supercapacitors. *Journal of Power Sources, 315*: 120-126.

Zhang, L. L., and Zhao, X. (2009). Carbon-based materials as supercapacitor electrodes. *Chemical Society Reviews, 38*(9): 2520-2531.

Zhang, N., Qi, P., Ding, Y. H., Huang, C.-J., Zhang, J. Y., and Fang, Y. Z. (2016b). A novel reduction synthesis of the graphene/Mn_3O_4 nanocomposite for supercapacitors. *Journal of Solid State Chemistry, 237*: 378-384.

Zhang, X., Shi, W., Zhu, J., Zhao, W., Ma, J., Mhaisalkar, S., Maria, T. L., Yang, Y., Zhang, H., and Hng, H. H. (2010). Synthesis of porous NiO nanocrystals with controllable surface area and their application as supercapacitor electrodes. *Nano Research, 3*(9): 643-652.

Zhang, X., Wang, X., Jiang, L., Wu, H., Wu, C., and Su, J. (2012). Effect of aqueous electrolytes on the electrochemical behaviors of supercapacitors based on hierarchically porous carbons. *Journal of Power Sources, 216*: 290-296.

Zhang, Y., Hao, H., and Wang, L. (2016c). Effect of morphology and defect density on electron transfer of electrochemically reduced graphene oxide. *Applied Surface Science, 390*: 385-392.

Zhao, B., Liu, P., Jiang, Y., Pan, D., Tao, H., Song, J., Fang, T., and Xu, W. (2012). Supercapacitor performances of thermally reduced graphene oxide. *Journal of Power Sources, 198*: 423-427.

Zhao, L., Qiu, Y., Yu, J., Deng, X., Dai, C., and Bai, X. (2013). Carbon nanofibers with radially grown graphene sheets derived from electrospinning for aqueous supercapacitors with high working voltage and energy density. *Nanoscale, 5*(11): 4902-4909.

Zhong, C., Deng, Y., Hu, W., Qiao, J., Zhang, L., and Zhang, J. (2015). A review of electrolyte materials and compositions for electrochemical supercapacitors. *Chemical Society Reviews, 44*(21): 7484-7539.

Zhou, H., Peng, Y., Wu, H. B., Sun, F., Yu, H., Liu, F., Xu, Q., and Lu, Y. (2016). Fluorine-rich nanoporous carbon with enhanced surface affinity in organic electrolyte for high-performance supercapacitors. *Nano Energy, 21*: 80-89.

Zhu, M., Meng, W., Huang, Y., Huang, Y., and Zhi, C. (2014). Proton-insertion-enhanced pseudocapacitance based on the assembly structure of tungsten oxide. *ACS Applied Materials & Interfaces, 6*(21): 18901-18910.

Zhu, Y., Murali, S., Cai, W., Li, X., Suk, J. W., Potts, J. R., and Ruoff, R. S. (2010). Graphene and graphene oxide: synthesis, properties, and applications. *Advanced Materials, 22*(35): 3906-3924.

LIST OF PUBLICATIONS AND PAPERS PRESENTED

Research Article:

1. Wong, C.P.P., Lai, C.W., Lee, K.M., Juan, J.C., & Hamid, S.B.A. (2016). Synthesis of reduced graphene oxide/tungsten trioxide nanocomposite electrode for high electrochemical performance. *Ceramics International*, 42(11), 13128-13135. (Q1, Impact factor = 2.758)
2. Wong, C.P.P., Lee, K.M., & Lai, C.W. (2017). Hydrothermal preparation of reduced graphene oxide/tungsten trioxide nanocomposites with enhanced electrochemical performance. *Journal of Materials Science: Materials in Electronics*, 1-14. (Q2, Impact factor = 2.019)
3. Lai, C.W., Low, F.W., Chong, S.W., Wong, C.P.P., Siti Zubaidah, B.M.S., & Hamid, S.B.A. (2015). An overview: recent development of titanium dioxide loaded graphene nanocomposite film for solar application. *Current Organic Chemistry*, 19(19), 1882-1895. (Q3, Impact factor = 1.949)

Presentation in Conference:

1. Wong, C.P.P., Lai, C.W., Lee, K.M., Juan, J.C., & Hamid, S.B.A. International Conference on Waste Management and Environment (ICWME 2015*)*, 20-22 August 2015.